The Dissertation Committee for Shixuan Yang Certifies that this is the approved version of the following dissertation:

Mechanics and Applications of Stretchable Serpentine Structures

Committee:

Nanshu Lu, Supervisor

K. Ravi-Chandar

Kenneth M. Liechti

Rui Huang

Nan Sun

Mechanics and Applications of Stretchable Serpentine Structures

by

Shixuan Yang, B.E.

Dissertation

Presented to the Faculty of the Graduate School of

The University of Texas at Austin

in Partial Fulfillment

of the Requirements

for the Degree of

Doctor of Philosophy

The University of Texas at Austin

May, 2016

Dedication

Dedicated to my family

Acknowledgements

I would like to express the deepest appreciation to my advisor and mentor, Professor Nanshu Lu. I'm indebted to Dr. Lu for her invaluable guidance and support on both my research and personal life through the five years of graduate school. Dr. Lu's strong expertise in biointegrated electronics, perceptive insights into problems and creative thoughts always enlighten my research towards "the" direction. Her genuineness for people and endless enthusiasm for research have set a high standard which constantly drove me to be a better person. Without her selfless mentoring and unflinching trust, this thesis would not have been possible.

I'm grateful to the collaborations with the research groups of Dr. Deji Akinwande, Dr. Dae-Hyeong Kim, Dr. Nan Sun, Dr. Dean Neikirk and Dr. David Schnyer. The thoughtful inputs from our collaborators have greatly expedited this work to its accomplishment.

Deep appreciation goes to my committee members, Dr. K. Ravi-Chandar, Dr. Kenneth M. Liechti, Dr. Rui Huang and Dr. Nan Sun, for having taken the time to guide me through various stages of this research. Their interest and guidance in this project make me feel confident and have the courage to carry on the work till the end.

I appreciate the opportunities to take classes from Dr. Stelios Kyriakides, Dr. Leszek F. Demkowicz, Dr. Gregory J. Rodin, Dr. Mark E. Mear, Dr. Chad M. Landis and Dr. Loukas Kallivokas. Their vast knowledge in and devotion to their own fields set good examples for me on how to be an excellent researcher.

I would also like to convey thanks to the financial support from National Science Foundation under Grant Nos. CMMI-1301335 and ECCS-1509767, as well as Cooperative Agreement EEC-1160494, and the partially support from Air Force Office of Scientific

Research under Grant No. FA9550-15-1-0112.

Thanks to the group members who have shared meaningful discussions with me, and who are always there ready to offer their hands to me. I'm greatly honored to witness the growth of this group from seed to bloom and meet so many talented researchers who are determined to bring us a brighter future through their persistence and perseverance.

Special thanks to my friends who have shared their time with me so that I could enjoy joyful life after research. My life will be a lot more difficult without their company and encouragement.

I would like to express my deepest love to my parents and parents-in-law. Thanks for bringing me and my beloved into this wonderful world and giving us the confidence to choose who we want to be. I feel so blessed being immersed in this unconditional love which makes me strong and fearless.

Finally, I would like to thank Ruyi Yang, my friend, my valentine, my darling and my soul mate. Thanks for your incredible patience during our first 2-year long-distance relationship and the courage and determination you showed me moving to Austin and keeping me company. You must have lived through countless difficulties along the way, most of which I'm even not aware of and hard to imagine, but you always show me your support without any complaints. I'm so blessed to have you around me and share all the joys and tears in life with me. You are the endless source of love and courage that give me the reason and guts to face any struggles in my life. I would like to put my arms around you and share the rest of my life with you.

Mechanics and Applications of Stretchable Serpentine Structures

Shixuan Yang, Ph.D.

The University of Texas at Austin, 2016

Supervisor: Nanshu Lu

Stretchable structures have been developed for various applications, including expandable coronary stents, deployable sensor networks and stretchable bio-mimetic and bio-integrated electronics. High-performance, stretchable electronics have to utilize high-quality and long-lasting inorganic electronic materials such as silicon, oxide dielectrics and metals, which are intrinsically stiff and often brittle. It is therefore an interdisciplinary challenge to make inorganic electronics stretchable while retaining their electronic functionality. Patterning stiff materials into serpentine-shaped wavy ribbons has become a popular strategy for fabricating stretchable inorganic electronics. However, due to the lack of mechanics understanding, design of serpentine structures is still largely empirical, whether for freestanding or substrate supported serpentines. This dissertation systematically investigates the mechanics of serpentine structures with emphasis on the effects of serpentine geometry and substrate stiffness, which involves theoretical analysis, numerical simulation, and experimental validation. Our theory has successfully predicted the stretchability and stiffness of various serpentine shapes and has been applied to the optimization of serpentine designs under practical constraints. We also find that not all geometric effects are monotonic and serpentines are not always more stretchable than linear ribbons. To manufacture high quality stretchable devices with high throughput and low

cost, we have invented a “cut-and-paste” method to fabricate both metallic and ceramic serpentines. As a demonstration of our method, a noninvasive, tattoo-like multifunctional epidermal sensor system has been built for the measurement of electrophysiological signals, skin temperature, skin hydration, and respiratory rate. Engineering of epidermal stretchable antenna for wireless communication is also detailed and rationalized.

Table of Contents

List of Tables

List of Figures

Chapter 1 Introduction

This chapter will discuss the background and motivation for flexible and stretchable electronics and their applications in bio-integrated devices. As conventional wafer-based electronics are planar and rigid, many mechanics strategies are proposed to enhance the flexibility and stretchability of intrinsically stiff and brittle inorganic electronics. Out of many available strategies, patterning inorganic conducting and semiconducting membranes into meandering serpentine ribbons offers high stretchability, low stiffness, as well as convenient bio-integration. The goal of this dissertation is to understand the fundamental mechanics of serpentine-shaped stretchable structures and propose an affordable method for manufacturing disposable yet high performance epidermal sensors for reliable vital sign monitoring.

1.1 BACKGROUND

This section is going to introduce the history and status quo of flexible (bendable), stretchable, and bio-integrated electronics, each of which will be discussed in a following subsection.

1.1.1 Flexible Electronics

Flexible electronics refers to electronic devices that are able to bend to a finite radius of curvature. The idea of flexible electronics can be dated back to 1948 [1], when a brief discussion of creating circuits on flexible insulating materials such as paper was first introduced. Following development on this topic has brought revolutionary changes to the design of electronic devices in the consumer, medical and military sectors [2-6]. The unconventional benefits of flexible electronics such as light weight, low cost and mechanical robustness provide solutions to the problems which are inefficient or even impossible to solve with traditional rigid electronics and thus offer possibilities for various new applications. The last 30 years [7, 8] has evidenced the booming growth of flexible electronics with lots of promising achievements such as flexible displays [9], conformable electronics textiles [10], rollable solar cells [11-16], adaptive RFID tags [4], artificial E-skins [17, 18], flexible photonic devices [19], and so on.

Organic materials are appealing for the design of flexible electronics due to their intrinsically small mechanical stiffness, light weight, low cost and adaptability for roll-to-roll processes [20-22]. Organic electronics can be fabricated through mass-printing methods such as offset printing or screen printing [23], and digital printing technologies such as inkjet printing or laser patterning. However such printing methods cannot provide satisfactory resolution and are not suitable for high-throughput, large-area fabrication of devices with small features. Moreover, the moderate electronic performance and chemical instability prevent organic electronics from becoming high-end devices.

Therefore, high-performance flexible electronics still relies on high-quality single-crystal inorganic semiconductors, such as silicon, gallium arsenide, and gallium nitride, which are well established materials with high on-off ratio, high carrier mobility, and excellent chemical stability [24-29]. Since inorganic materials usually rupture at small strain, for example 1%, strain management strategies have been proposed to achieve high bendability. An early strategy is to thin down the inorganic functional materials and their substrates, if any [30-32]. Later on, mechanicians suggested sandwiching the inorganic films between identical polymer layers so that the brittle material is placed along the neutral axis of the multilayer to minimize the bending strain [26, 30, 33]. Recently, researchers proposed that there can be multiple neutral axes in an alternating stiff-soft-stiff multilayer stack such that a multilayer flexible electronics can be realized [19]. The fabrication of inorganic flexible electronics involves thin film deposition, photolithography, and micro-transfer printing [34-36], which are high-resolution patterning methods and will be detailed later.

1.1.2 Stretchable Electronics

Although flexible electronics represents an important step towards soft electronics, it is difficult to conform simply bendable electronics to complex 3D surfaces or mimic soft biological systems. As a result, rubber-like inorganic stretchable electronics have began to emerge [37-41]. Examples include stretchable transistors and CMOS circuits [31, 42], soft bio-mimic devices, tissue-like bio-integrated electronics [5, 43-46], and deployable sensor networks[47, 48].

Inorganic semiconductors and conductors are known to be very stiff and even brittle. For example, silicon and gallium arsenide tend to rupture at strains around 1%[49]. Copper and gold films tend to yield and develop irreversible deformation around 0.2%. In contrast, bio-tissues can deform by tens of percent and deployable sensors such as balloon catheters

[5, 50-52] and structural health monitoring systems [48] demand stretchability of hundreds of percent. To minimize strain in inorganic materials and achieve high system compliance, several mechanical design strategies have been proposed. One strategy is exploiting the wrinkling and buckling delamination of stiff nano-ribbons or nano-membranes on soft elastomeric substrates [31, 53-59], as shown in Figure 1.1 (a)&(b). The inorganic nano-ribbons or nano-membranes are transferred onto a pre-stretched, compliant elastomeric substrate, which is then released to form wrinkled or buckled shapes, depending on the level of the film-substrate adhesion. Under external stretching, the compliant substrate will be elongated and the wrinkled nano-membrane will flatten and accommodate the stretch through rigid body rotation. Although this strategy was widely adopted in early inorganic stretchable electronics [58, 60-62], its implementation has dimed nowadays due to the fact that their corrugated surfaces are not amenable to encapsulation and bio-integration. Another strategy is to adopt the so called island-plus-serpentine designs supported by stretchable substrates, as shown in Figure 1.1 (c)&(d). In this configuration, the functional electronics are fabricated on or as the rigid islands and the islands are connected to their adjacent islands through stretchable serpentine interconnects. When the substrate is stretched, the serpentine interconnects will rotate in plane or buckle out of plane to accommodate the applied stretch, leaving small strains in the stiff islands. One issue for the island-plus-serpentine design is that the islands are still rigid and non-stretchable, which compromise the overall device compliance and stretchability. Eliminating the islands while keeping serpentines interconnected yield the so called filamentary serpentine network, which enabled epidermal electronics [63]. A more stretchable variation is called fractal serpentine design [64-66], whose stretchability can reach hundreds of percent.

Similar to flexible electronics, success of stretchable electronics relies on suitable photolithography and transfer printing technologies [67, 68]. The process of transfer

printing starts with preparation of an assembly of microstructures on a rigid donor wafer, which mainly involves thin film deposition, photolithography and wet/dry etching. Then an elastomeric stamp will be pressed against the microstructures to peel them off the donor substrate and transfer them to the target stretchable substrate. This process has been widely adopted in the manufacture of inorganic flexible and stretchable electronics.

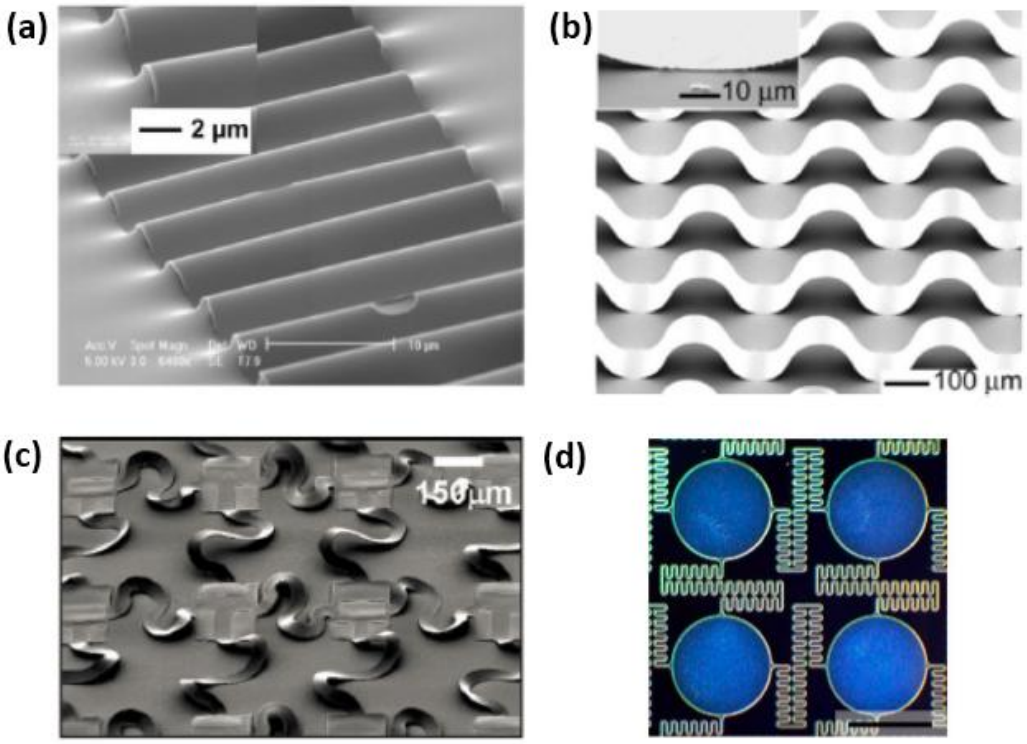

Figure 1.1 Different strategies for achieving high stretchability [69]. (a) SEM image of wrinkling ribbons [69]. (b) SEM image of buckling ribbons. (c) SEM image of non-coplanar-serpentine-island structure [70]. (d) Optical image of coplanar-serpentine-island structure [71]. The scale bar in this image is 2 mm.

1.1.3 Bio-Integrated Electronics

Bio-integrated electronics is an important branch of flexible and stretchable electronics. Conventional wafer-based inorganic electronics are intrinsically stiff and planar [72], while human bodies are compliant, curvilinear and highly deformable. Typically, the bulk electrodes are mounted on the skin via adhesive tapes, mechanical clamps or straps, or penetrating needles [73-75], which are irritating, obstructive and invasive methods that cause discomfort for the patient and induce error in the biosignal readings, due to the huge mismatch in the mechanical properties between conventional stiff electronic devices and compliant human bodies. In contrast, high-performance flexible and stretchable electronics can be engineered in form factors that are close to human tissues and organs, which enables intimate and non-irritating contact with human body for sensing, diagnosis and therapy.

As an example, Figure 1.2 (a) shows an instrumented balloon catheter for minimum invasive cardiac ablation therapy which is capable of measuring temperature, flow, tactile, optical and electrophysiological data. The balloon catheter serves as a platform for collections of sensors and actuators and the devices offers several modes of sensory feedback control. *In vivo* epicardial experiments of cardiac electrophysiological recording of rat and rabbit hearts have been successfully conducted by using this instrumented balloon catheter and tactile data has been extracted to monitor balloon-inflation level, electrical contact between the heart and device and onset of tachycardias. This multifunctional balloon catheter is also equipped with RF ablation electrodes which can be used to create lesions on the heart, and the extent of lesion can be monitored by the onsite temperature sensor, which makes controlled lesion formation possible [5]. Another example is the epidermal electronics system (EES), as shown in Figure 1.2 (b), whose thicknesses, effective elastic moduli, bending stiffnesses, and areal mass densities matched

to the epidermis, such that it can develop conformal contact and adequate adhesion to human skin with van der Waals interactions alone. Electrophysiological (EP) signals such as electroencephalograms (EEG), electrocardiograms (ECG) and electromyograms (EMG) can be monitored by this device system and other onboard sensors such as temperature sensor and RF diode make it multifunctional for human body health monitoring.

In addition to medical applications, bio-integrated electronics can also help to establish human-machine interfaces for prosthetic control, remote surgery, education and gaming. For example, Figure 1.3 illustrates a human-robot interaction loop in which bio-integrated electronics can serve as building blocks in all the five phases [20, 76, 77].

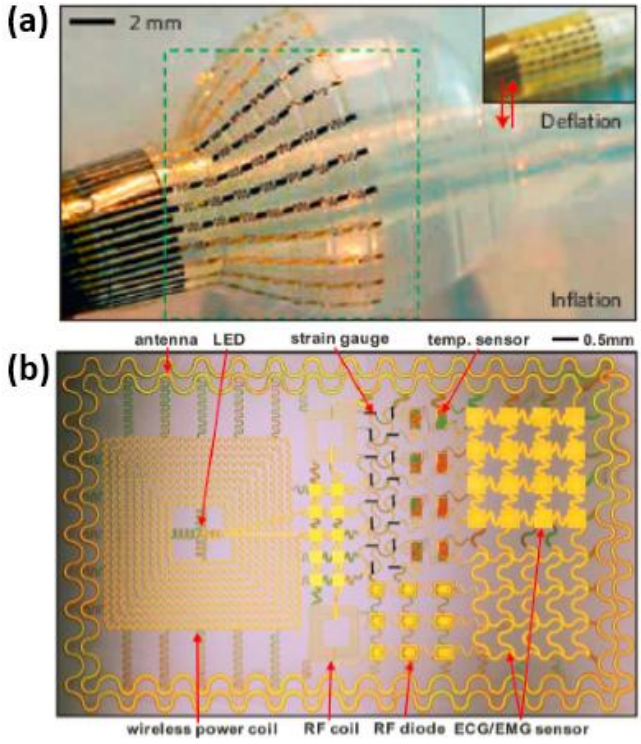

Figure 1.2 (a) Optical image of a stretchable, interconnected passive network mesh integrated on a balloon catheter which is inflated by 130% relative to its deflated state (inset) [5]. (b) Top view image of a Epidermal Electronics System (EES) with physical properties matched to the epidermis [63].

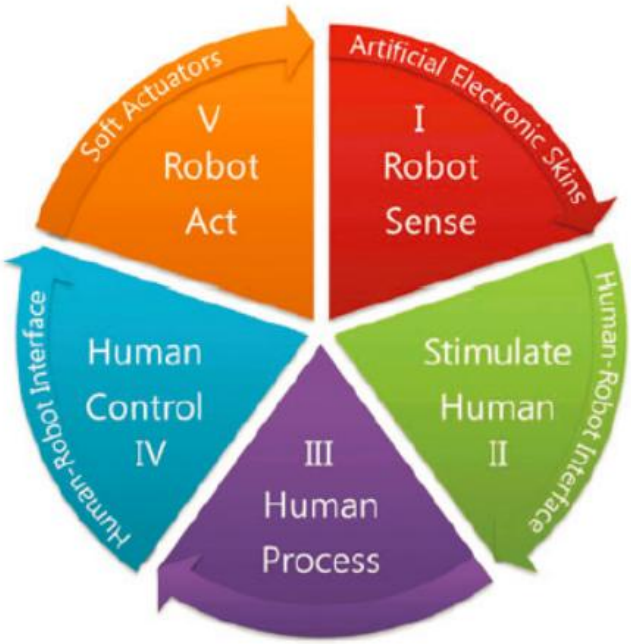

Figure 1.3 Schematic diagram of the five-step human-robot interaction loop [20]. Step I, the robot senses environmental stimuli (e.g., touch) through artificial electronic skins (E-skins). Step II, the robot passes the sensed environmental signal to the human through human-robot interface. Step III, the human processes the received stimulation. Step IV, the human sends out control signals through human-robot interface. Step V, robot (actuator) takes action according to the commands it received.

1.2 MOTIVATION

Development of high-performance flexible, stretchable and bio-integrated electronics is a highly interdisciplinary challenge which requires advances in electronics, materials and mechanics. The fundamental mechanics understanding of the novel structures of stiff materials and the interaction between hard and soft materials have all proved to be the critical driving forces for inorganic soft electronics. Despite existing achievements, many strain analyses just rely on finite element simulation and analytical solutions are lacking. As a result, many structural designs of deformable circuits are still empirical. Therefore theoretical derivation and corresponding experimental validation are highly desirable.

The wide-spread success of soft electronics also hinges on high-throughput and low-cost manufacturing methods. The current photolithography-based fabrication process for bio-integrated electronics involves clean room facilities and chemical processes, which are time, cost and labor intensive, and the overall yield is still unsatisfactory. Therefore, alternative time and cost effective manufacturing processes are in demand.

1.3 SCOPE OF RESEARCH

The goal of this dissertation is to understand the fundamental mechanics of serpentine-shaped stretchable structures and propose an affordable method for manufacturing disposable yet high performance epidermal sensors for reliable vital sign monitoring. Chapter 2 analytically investigates non-buckling freestanding serpentine ribbons via curved beam and elasticity theories. When serpentines are supported by polymer substrates, the substrate stiffness and serpentine-substrate adhesion also affect the serpentine behavior, which are studied in Chapter 3. In terms of manufacture and application of serpentines, Chapter 4 introduces a “cut-and-paste” fabrication method which can produce affordable and disposable stretchable serpentines, and Chapter 5

demonstrates its capability through an epidermal sensor system for multimodal vital sign monitoring. In addition to sensing, serpentines can also be used in wireless stretchable antenna, which is thoroughly investigated in Chapter 6. Conclusions and outlook of future research are given in Chapter 7.

Chapter 2 Freestanding Serpentines[1,2]

Freestanding serpentine structures can be found in many stretchable structures that are made out of intrinsically stiff materials, such as cardiovascular stents and deployable sensor networks. Because they are not confined by any supporting substrates, they can deform freely when subjected to external loading. When serpentine width is comparable or larger than the thickness, the serpentine ribbon can buckle and twist out-of-plane to lower the elastic energy. When serpentine width is smaller than its thickness, the serpentine will deform in-plane and hence can be modeled by 2D plane-strain curved beam or elasticity theory. Analytical solutions using both theories are derived based on three independent, dimensionless geometric variables. Finite element modeling (FEM) and experiments are used for validation. As a demonstration, the theoretical results are applied to optimize the geometry of a freestanding serpentine under practical constraints. Polymer embedded non-buckling serpentines are also investigated.

---

[1] T. Widlund, S. Yang, Y. Y. Hsu, N. Lu*, "*Stretchability and compliance of freestanding serpentine-shaped ribbons*" International Journal of Solids and Structures, vol. 51, no. 23-24, pp. 4026-4037, Nov, 2014.
Author contributions: T. W. conducted FEM and analytical analysis. S. Y. performed experiments and validation of T. W.'s FEM and analytical work. N. L. supervised and coordinated the project. N. L. and T. W. wrote the paper.

[2] S. Yang, S. Qiao, N. Lu*, "*Elasticity solutions to non-buckling serpentine ribbons*", to be submitted
Author contributions: S. Y. conducted FEM analysis. S. Y. performed analytical analysis with S. Q.'s assistance. N. L. supervised and coordinated the project. N. L. and S. Y. wrote the paper.

2.1 OBJECTIVE AND INTRODUCTION

To overcome the intrinsic stiffness of inorganic electronics materials, a popular strategy is to pattern them into serpentine shapes. The structural design of serpentine-based stretchable circuits dictates the stretchability and compliance of the system. Although the mechanical behavior of serpentines has been widely studied by numerical and experimental means, available analytical solutions are very limited, which hinders the development of a rational and transformative design paradigm for inorganic stretchable electronics. This is mainly attributed to the difficulty of analyzing large displacement and out-of-plane buckling of thin serpentine ribbons. But the deformation of non-buckling freestanding serpentines can be analytically solved through curved beam (CB) and elasticity theories. An introduction to buckling and non-buckling serpentines is offered as follows.

2.1.1 Out-of-Plane Buckling

When freestanding serpentine structures have small width-to-thickness ratios, they tend to buckle out-of-plane when subjected to tensile stretch. This is because for this structure, out-of-plane buckling favors the minimization of the global energy, which is the essential driving force for all physical phenomena. Although general three-dimensional (3D) theories for curved thin rods are available [78], theoretical analysis for out-of-plane buckling and post-buckling analysis for curved beams are still lacking and limited to 1D serpentine structures, few serpentine shapes and loading conditions [79-81]. Due to the complexity of analytically solving the post-buckling partial differential equations (PDE) [82], the analytical work for serpentine networks is still very limited. Nevertheless, numerical analyses of buckled freestanding serpentine interconnects have provided practical design guidelines [66, 83] and the buckled geometry for serpentine networks can also be visualized from the result of FEM and the deformed shape is well aligned with experiment result (Figure 2.1).

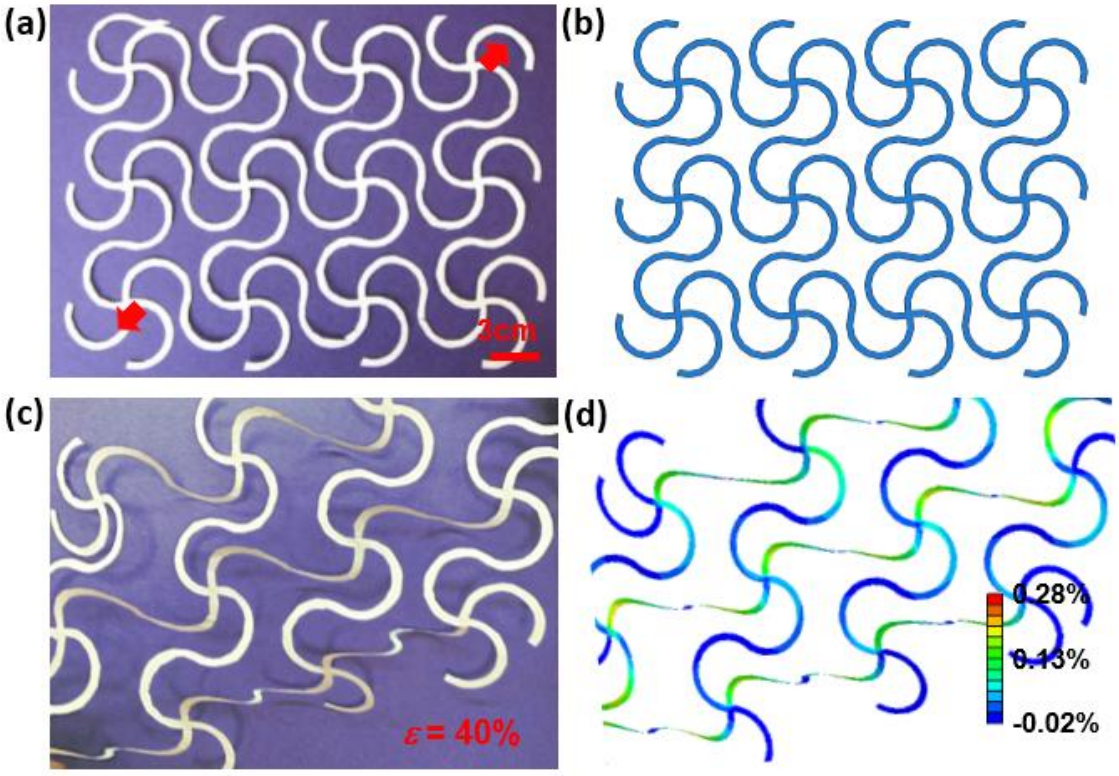

Figure 2.1 Comparison of experiment and simulation. Unstretched serpentine network paper cut in (a) experiment and (b) model. Serpentine network paper cut that is subject to 40% diagonal strain in (c) experiment and (d) model.

2.1.2 In-Plane Rigid Body Rotation

When freestanding serpentine structures have large width-to-thickness ratio, they tend to experience in-plane rigid body rotation when subject to tensile stretch. These structures can be found in a lot of expandable systems made out of intrinsically stiff materials. Examples include the cardiovascular stents for angioplasty [52] or percutaneous coronary intervention [51], and deployable sensor networks for structural health monitoring [48], Tubular metallic stents in the form of a serpentine-meshed scanfold can be inserted into blood vessels in a very small initial diameter, tunnel through the veins and arteries, and get expanded by more than 200% using a balloon catheter, to provide support inside the patient's arteries. As another example, ultra narrow, highly tortuous serpentines were incorporated in the design of a spider-web-like highly expandable sensor network [48]. The microfabrication of inorganic-material-based sensors which has to utilize regular-sized spinners, mask aligners, and vacuum chambers can all be performed on a wafer-sized rigid substrate. Once the circuit is released from the rigid substrate, the sensor network can be deployed by more than 100 times in area so that they can cover macroscopic civil or aerospace structures to perform structure health monitoring. In both examples, the large expandability comes from just the in-plane rigid body rotation of the freestanding serpentine ligaments.

Although serpentines have been widely used as the stretchable configuration of stiff materials, the designs of the serpentine shape are still largely empirical. According to existing studies, the applied strain-to-rupture of metallic serpentine ribbons varies from 54% to 1600%, depending on the geometric parameters such as ribbon width, arc radius, arm length, substrate support, and so on [48, 70, 84-86]. A few experimental and finite element modeling (FEM) studies have been conducted to provide insights into the shape-dependent mechanical behavior [83, 84, 86] of serpentine ribbons. Two recent theoretical articles

provided viable routes to predict the stretchability of buckled serpentines [87] and self-similar serpentines [88], but the shapes of the unit cells are very limited. Moreover, the effective compliance of the serpentine structure and the shape optimization under practical constraints have been rarely discussed.

This chapter intends to reveal the effects of the geometrical parameters on the stretchability and effective stiffness of freestanding non-buckling serpentine structures. Two analytical approaches, i.e. Curved Beam (CB) and elasticity theories will be used to study this problem and comparison of the two methods will be conducted. Serpentine stretchability and effective stiffness as functions of dimensionless geometric variables will be offered, and geometric optimization will be performed based on the analytical results. Polymer embedded non-buckling serpentines will also be numerically simulated and compared with freestanding solutions.

2.2 PROBLEM DESCRIPTION

The structure that we intend to study is a periodic serpentine ribbon whose unit cell is depicted in Figure 2.2(a). As labeled in Figure 2.2(a), the curved section is called the arc, and the straight section is called the arm. A uniaxial tensile displacement u_0 in the direction of periodicity is applied at each end. As we limit ourselves to thick ribbons that do not buckle out-of-plane under applied u_0, plane strain conditions can be assumed such that we only need to solve a 2D elasticity problem. Applying the symmetric and anti-symmetric features of the serpentine structure as well as the boundary conditions, the 2D problem can be further simplified and the boundary value problem to solve is illustrated in Figure 2.2(b). Specifically, the quarter serpentine is clamped at the right end, which is the axis of symmetry, and subjected to a displacement loading $u_0/2$ at the middle point of the the left end, whose reaction force is denoted by P. The geometry of the 2D serpentine structure can be fully defined by the four independent parameters labeled in Figure 2.2(a):

the arc radius *R*, the ribbon width *w*, the arm length *l*, and the arc opening angle α. The end-to to-end distance of a unit cell is denoted by *S*, which takes the form

$$S = 4\left(Rcos(\alpha) - \frac{l}{2}Rsin(\alpha)\right) \tag{2.1}$$

If the serpentine is stretched by u_0 at each end as shown in Figure 2.2(a), we define the applied strain as

$$\varepsilon_{app} = \frac{2u_0}{S} \tag{2.2}$$

After non-dimensionalization, three independent dimensionless parameters are used in this study: w/R, l/R, and α. The three dimensionless parameters are essentially the three degrees of freedom in the serpentine design space as illustrated in Figure 2.2(c) .Many different serpentine geometries can be analytically defined by different combinations of the three parameters, which can be represented as points in the first quadrant of the 3D design space. Representative serpentine shapes are summarized in Figure 2.3. Since dimensionless variables are used in this study, self-similar serpentines, no matter macro-, micro-, or nano-scale, as long as their w/R, l/R and α are all the same, their structural properties such as normalized effective stiffness and stretchability will not have any difference, assuming no size-dependent material properties.

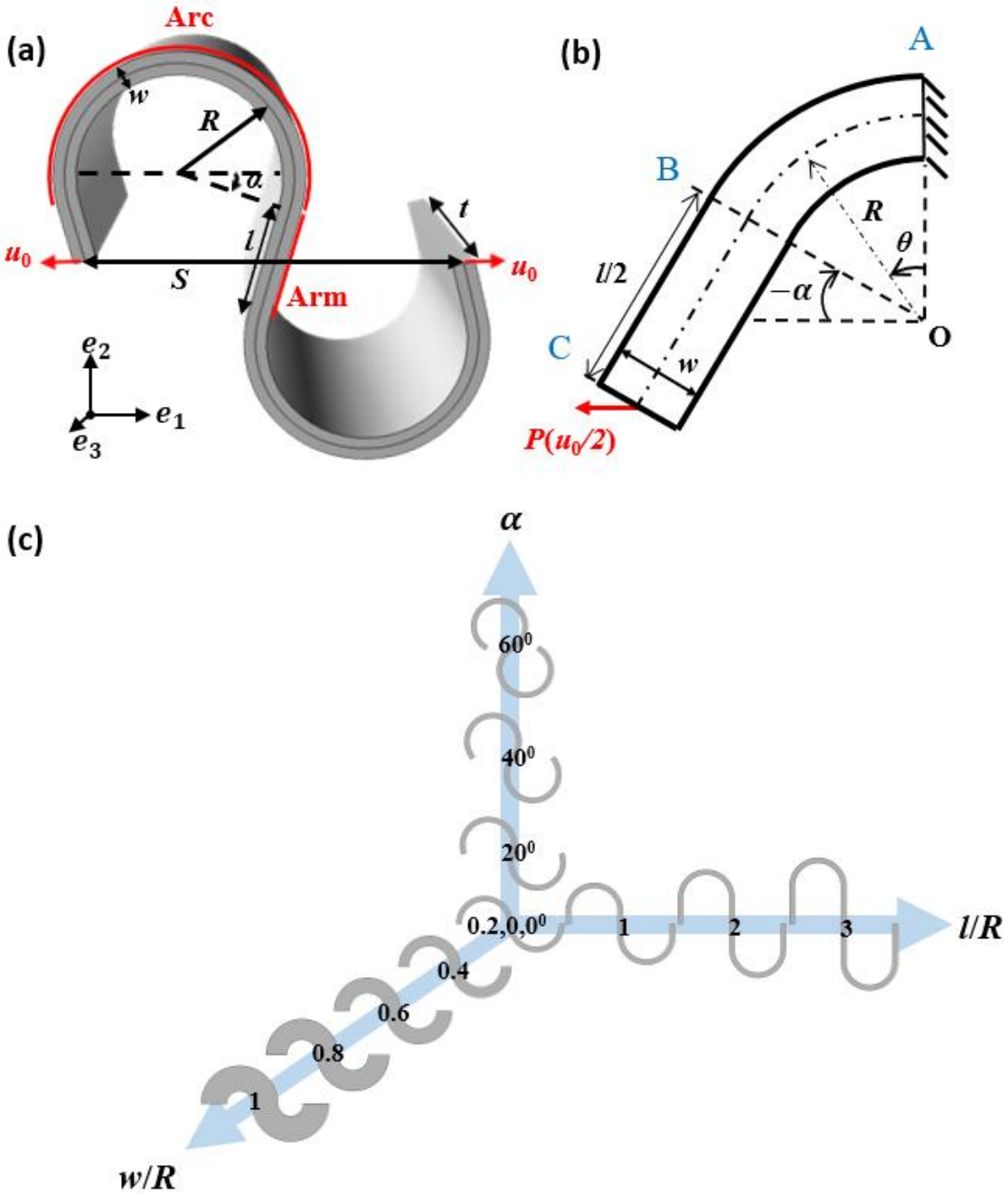

Figure 2.2 (a) Schematic for a unit cell of periodic freestanding serpentine structure. (b) Boundary condition for a plane strain representation for the original problem. (c) The 3 degree of freedom design space for serpentine shape.

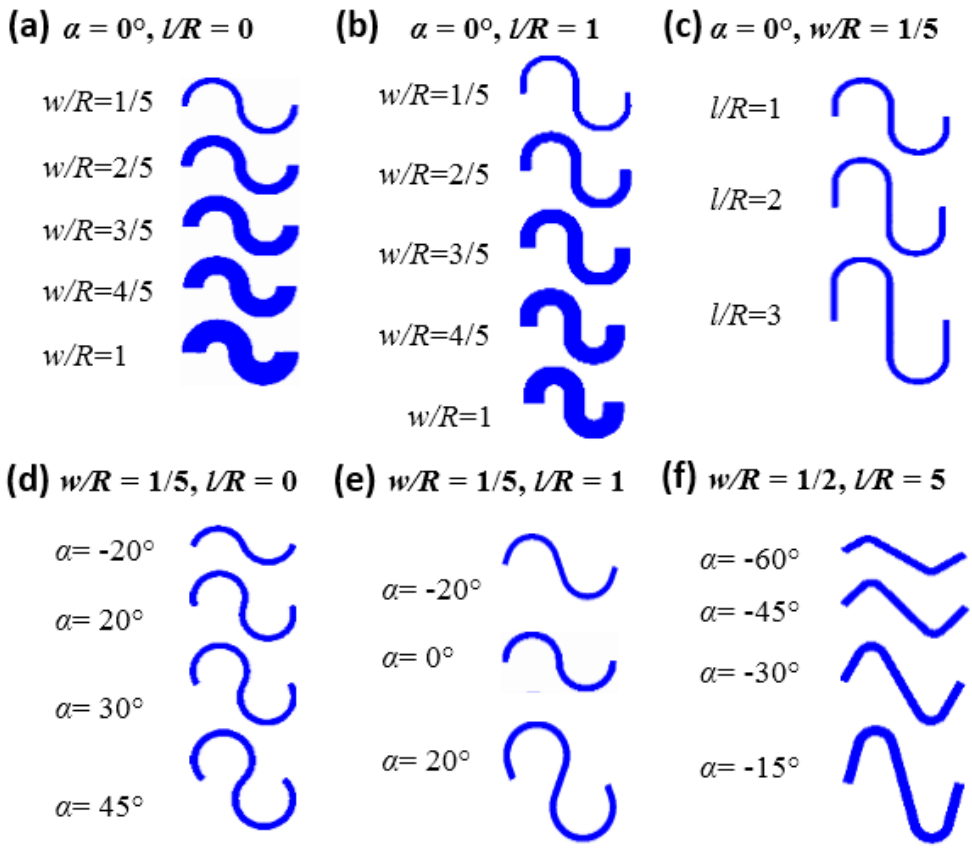

Figure 2.3 Schematics of the serpentine shapes where (a) $\alpha = 0°$, $l/R = 0$,with varying w/R (b) $\alpha = 0°$, $l/R = 1$, with varying w/R (c) $\alpha = 0°$, $w/R = 5$, with varying l/R (d) $w/R = 1/5$, $l/R = 0$, with varying α(e) $w/R = 1/5$, $l/R = 1$, with varying α, and (f) $w/R = 1/2$, $l/R = 5$, with varying α.

In this problem, we are particular interested in two mechanical behaviors of serpentines: the stretchability and the effective stiffness. *Stretchability* is defined as the critical applied strain beyond which the material of the serpentine ribbon will rupture and will be denoted by $\varepsilon_{\text{app}}^{\text{cr}}$. Therefore, if the failure criterion is $\varepsilon_{\max} = \varepsilon_{\text{cr}}$, where $\varepsilon_{\max}$ and ε_{cr} represent the maximum tensile strain and the intrinsic strain-to-rupture of the material, respectively, the normalized maximum tensile strain in the serpentine, $\varepsilon_{max}/\varepsilon_{app}$, will govern the stretchability by

$$\varepsilon_{app}^{cr} = \frac{\varepsilon_{cr}}{\varepsilon_{max}/\varepsilon_{app}}, \tag{2.3}$$

which means we only need to focus in the study of $\varepsilon_{max}/\varepsilon_{app}$ and the stretchability of serpentines will be directly reflected from it.

Effective stiffness is defined as the ratio of the reaction force P to the overall displacement. With Young's modulus E and Poisson's ratio v, the stiffness of a plane strain straight ribbon of length S and width w is given by $\bar{E}w/S$, where $\bar{E} = E/(1-v^2)$ is the plane strain modulus. Therefore the effective stiffness of a serpentine ribbon normalized by that of straight ribbon of the same end-to-end length is given by $PS/(2\bar{E}wu_0)$. When α approaches -90^o, i.e. when the serpentine degenerates to a linear ribbon, both $\varepsilon_{\max}/\varepsilon_{\text{app}}$ and $PS/(2\bar{E}wu_0)$ should approach one.

2.3 ANALYTICAL MODELING AND SIMULATION

In this study, we adopt both curved beam (CB) and elasticity theories to analytically solve this problem.

2.3.1 Curved Beam (CB) Theory Solution

The internal forces in the curved beam shown in Figure 2.2(b) can be expressed as

$$N_{arc} = P\cos(\theta), V_{arc} = -P\sin(\theta), M_{arc} = PR(\sin(\alpha)+\cos(\theta)) + P\frac{l}{2}\cos(\alpha) \tag{2.4}$$

$$N_{arm} = P\sin(\alpha), V_{arm} = -P\cos(\alpha), M_{arm} = Ps\cos(\alpha), \tag{2.5}$$

where N is the internal normal traction at the centroid of the cross section and M is the internal moment at the cross section. Castigliano's theorem can be used to correlate the applied displacement u_o and reaction force P

$$\frac{u_o}{2} = \frac{\partial U}{\partial P} = \frac{\partial (U_{arm}+U_{arc})}{\partial P}, \tag{2.6}$$

where U is the total elastic energy and comprises energy from the serpentine arm and arc, whose form are

$$U_{arm} = \int_0^{\frac{l}{2}} \left[\kappa \frac{V_{arm}{}^2}{2GA} + \frac{N_{arm}{}^2}{2\bar{E}A} + \frac{M_{arm}{}^2}{2\bar{E}I_2} \right] ds \tag{2.7}$$

and

$$U_{arc} = \int_0^{\alpha+\frac{\pi}{2}} \left[\frac{(N_{arc}R - M_{arc})^2}{2\bar{E}AR^2} + \frac{M_{arc}{}^2}{2\bar{E}I_2} \right] Rd\theta, \tag{2.8}$$

where κ=*1.5*, is the correction coefficient for strain energy in a rectangular section. Since the stiffness of a straight ribbon is given by $\bar{E}w/S$, and for plane strain problems, we assume a thickness t = 1 so that $A = w, I_2 = w^3/12$, and $\bar{E} = E/(1-\nu^2)$. Therefore we obtain the relationship between the applied displacement u_o and the reaction force P as

$$\frac{u_0}{2} = \frac{PR^3}{w^3\bar{E}} \begin{bmatrix} \cos^2(\alpha)\left(\frac{l^3}{2R^3} + 3\left(\frac{\pi}{2}+\alpha\right)\frac{l^2}{R^2} + 12\frac{l}{R} - 12\left(\frac{\pi}{2}+\alpha\right)\right) \\ +\sin(2\alpha)\left(6\left(\frac{\pi}{2}+\alpha\right)\frac{l}{R}+9\right) \\ +\frac{w^2}{R^2}\left[\left(\frac{\pi}{2}+\alpha\right)\left(\frac{l}{2R}\cos(\alpha)+\sin(\alpha)\right)^2 + \frac{l}{2R}\left(\sin^2(\alpha)+\frac{3\bar{E}}{2G}\cos^2(\alpha)\right)\right] + 18\left(\frac{\pi}{2}+\alpha\right) \end{bmatrix}. \tag{2.9}$$

The effective stiffness is then given by

$$\frac{PS}{2\bar{E}wu_0} = \frac{\frac{w^2}{R^2}\left(\cos(\alpha) - \frac{l}{2R}\sin(\alpha)\right)}{2\left[\begin{array}{c}\cos^2(\alpha)\left(\frac{l^3}{2R^3} + 3\left(\frac{\pi}{2}+\alpha\right)\frac{l^2}{R^2} + 12\frac{l}{R} - 12\left(\frac{\pi}{2}+\alpha\right)\right) \\ +\sin(2\alpha)\left(6\left(\frac{\pi}{2}+\alpha\right)\frac{l}{R}+9\right) \\ +\frac{w^2}{R^2}\left[\left(\frac{\pi}{2}+\alpha\right)\left(\frac{l}{2R}\cos(\alpha)+\sin(\alpha)\right)^2 + \frac{l}{2R}\left(\sin^2(\alpha)+\frac{3\bar{E}}{2G}\cos^2(\alpha)\right)\right] + 18\left(\frac{\pi}{2}+\alpha\right)\end{array}\right]} \quad (2.10)$$

For the curved beam, the hoop stress in the arc is given by

$$\sigma_{\theta\theta} = \frac{N-\frac{M}{R}}{A} - \frac{My}{(1+\frac{y}{R})I_2}, \quad (2.11)$$

where A is the cross-sectional area and y is the distance from the middle line. By applying Hook's law, the hoop strain is then obtained by

$$\varepsilon_{\theta\theta} = \frac{\sigma_{\theta\theta}}{\bar{E}} \quad (2.12)$$

As the maximum local strain always occurs at the center of the inner crest of the arc (as shown in Figure 2.4 (a)), i.e. $\theta = 0^o$ and $y = -w/2$, we finally obtain the normalized maximum strain as

$$\frac{\varepsilon_{max}}{\varepsilon_{app}} = \frac{\frac{w}{R}\left[\frac{12}{2-\frac{w}{R}} + \left(\frac{12}{2-\frac{w}{R}} - \frac{w}{R}\right)\left(sin(\alpha) + \frac{l}{2R}cos(\alpha)\right)\right]\left(\cos(\alpha) - \frac{l}{2R}\sin(\alpha)\right)}{\left[\begin{array}{c}\cos^2(\alpha)\left(\frac{l^3}{2R^3} + 3\left(\frac{\pi}{2}+\alpha\right)\frac{l^2}{R^2} + 12\frac{l}{R} - 12\left(\frac{\pi}{2}+\alpha\right)\right) \\ +\sin(2\alpha)\left(6\left(\frac{\pi}{2}+\alpha\right)\frac{l}{R}+9\right) \\ +\frac{w^2}{R^2}\left[\left(\frac{\pi}{2}+\alpha\right)\left(\frac{l}{2R}\cos(\alpha)+\sin(\alpha)\right)^2 + \frac{l}{2R}\left(\sin^2(\alpha)+\frac{3\bar{E}}{2G}\cos^2(\alpha)\right)\right] + 18\left(\frac{\pi}{2}+\alpha\right)\end{array}\right]} \quad (2.13)$$

Now, fully analytical results for the effective stiffness (Equation (2.10)) and stretchability (Equation (2.13)) from CB theory have been achieved, and will be compared with the elasticity solution derived in the following subsection.

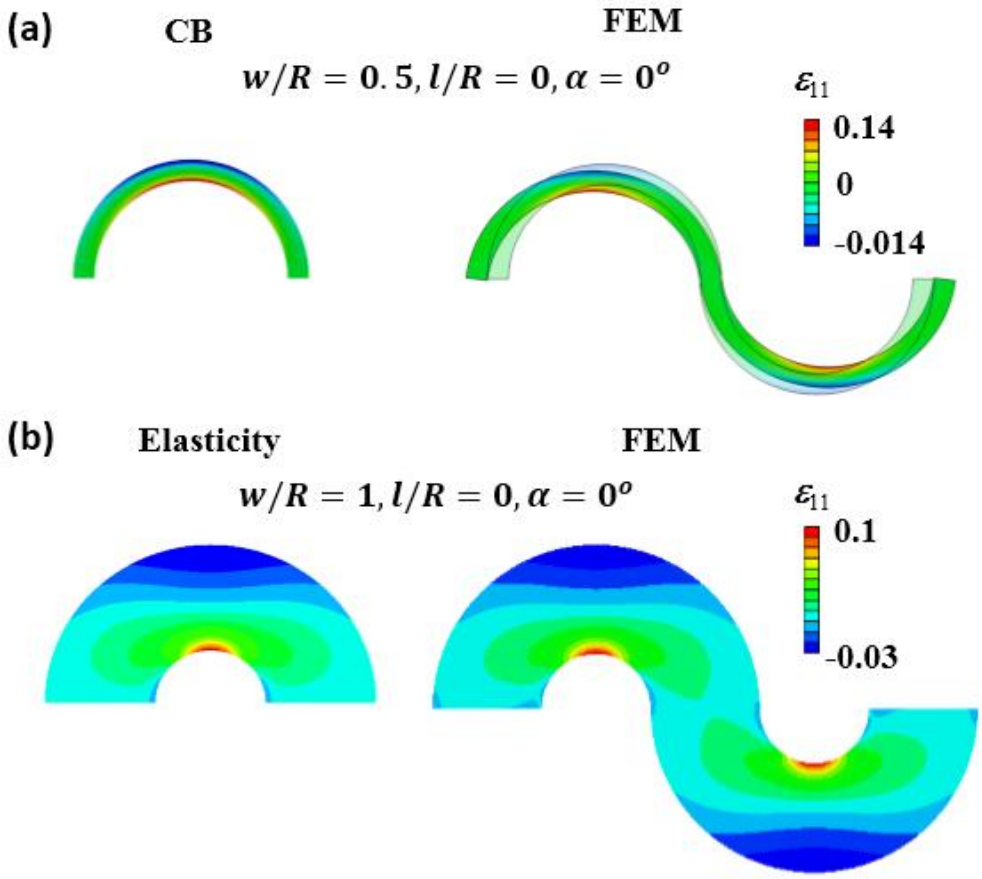

Figure 2.4 (a) Comparison between curve beam theory result and FEM result, for narrow serpentine with w/R = 1/5, l/R = 0, α=0°. (b) Comparison between elasticity solution and FEM result, for wide serpentine with w/R = 1, l/R = 0, α=0°.

2.3.2 Elasticity Solution

The elasticity solution starts with breaking down the original problem in Figure 2.2 (b) into three sub-problems, as illustrated in Figure 2.5 (a)-(c). Figure 2.5 (a) and Figure 2.5 (b) depict two sub-boundary value problems for the arc, where M_2 in Figure 2.5 (a) is the balancing moment for P in the arc section, M_1 in Figure 2.5 (c) is the balancing moment for P in the arc section, and M_1 in Figure 2.5 (b) is the reaction moment:

$$M_1 = P\frac{l}{2}cos\ (\alpha), M_2 = P\frac{a+b}{2}\big(1 + sin\ (\alpha)\big), \tag{2.14}$$

where a and b represent the inner and outer radii of the arc

$$a = R - \frac{w}{2}, b = R + \frac{w}{2}. \tag{2.15}$$

The resultant moment M at the fixed end of the arc is therefore given by

$$M = M_1 + M_2 \tag{2.16}$$

The original serpentine problem is now decomposed into three sub-cases with simple geometry and well-defined boundary conditions and it is hence possible to find analytical Airy stress functions for each of them. A Polar coordinate system will be used to solve the stress/strain field in the arc whereas a Cartesian coordinate system will be used for the arm. The coordinate origins and vectors are illustrated in Figure 2.5 (a)-(c). Based on the boundary value problems and the principle of Airy stress functions, stress functions can be assembled for sub-problems defined in Figure 2.5 (a), (b) and (c), respectively:

$$\varphi_1 = \left(\frac{A_1}{r} + A_2\, rln(r) + A_3\, r^3\right) cos(\theta) + A_4 ln(r) + A_5 r^2 + A_6 r^2 ln(r), \tag{2.17}$$

$$\varphi_2 = B_1\ ln(r) + B_2\, r^2 + B_3\, r^2\, ln(r) \tag{2.18}$$

and

$$\varphi_3 = C_1\, y^2 + C_2\, xy + C_3 y^3 + C_4 xy^3 \tag{2.19}$$

where A_i, B_i and C_i are constants to be determined by applying the boundary conditions.

The stress field for each of the sub-problem can then be derived by taking

derivatives of the corresponding stress function in polar or Cartesian coordinates and can be expressed in terms of geometrical parameters, applied force *P*, spatial variables such as r, θ, x, y, and the unknown constants. The unknown constants can be determined by implementing weak force boundary conditions.

For Figure 2.5 (a)

$$\begin{cases} 1. r = a, \sigma_{rr} = \sigma_{r\theta} = 0 \\ 2. r = b, \sigma_{rr} = \sigma_{r\theta} = 0 \\ 3. \theta = 0, \int_a^b \sigma_{\theta\theta} dr = P, \int_a^b \sigma_{r\theta} dr = 0, \int_a^b \sigma_{\theta\theta} r dr = \left(\frac{a+b}{2} + c\right) P \sin(-\alpha) \\ 4. \theta = \frac{\pi}{2} + \alpha, \int_a^b \sigma_{\theta\theta} dr = P \sin(-\alpha), \int_a^b \sigma_{r\theta} dr = P \cos(\alpha), \int_a^b \sigma_{\theta\theta} r dr = \left(\frac{a+b}{2} + c\right) P \sin(-\alpha) \end{cases} \quad (2.20)$$

For Figure 2.5 (b)

$$\begin{cases} 1. r = a, \sigma_{rr} = \sigma_{r\theta} = 0 \\ 2. r = b, \sigma_{rr} = \sigma_{r\theta} = 0 \\ 3. \int_a^b \sigma_{\theta\theta} dr = 0, \int_a^b \sigma_{r\theta} dr = 0, \int_a^b \sigma_{\theta\theta} r dr = -\frac{l}{2} P \cos(\alpha) \\ 4. \theta = \frac{\pi}{2} + \alpha, \int_a^b \sigma_{\theta\theta} dr = 0, \int_a^b \sigma_{r\theta} dr = 0, \int_a^b \sigma_{\theta\theta} r dr = -\frac{l}{2} P \cos(\alpha) \end{cases} \quad (2.21)$$

For Figure 2.5 (c)

$$\begin{cases} 1. y = -\frac{b-a}{2}, \sigma_{yy} = \sigma_{xy} = 0 \\ 2. y = \frac{b-a}{2}, \sigma_{yy} = \sigma_{xy} = 0 \\ 3. x = 0, \int_{-\frac{b-a}{2}}^{\frac{b-a}{2}} \sigma_{xx} dy = P \sin(-\alpha), \int_{-\frac{b-a}{2}}^{\frac{b-a}{2}} \sigma_{xy} dy = -P \cos(\alpha), \int_{-\frac{b-a}{2}}^{\frac{b-a}{2}} \sigma_{xx} y dy = \frac{l}{2} P \cos(\alpha) \\ 4. x = \frac{l}{2}, \int_{-\frac{b-a}{2}}^{\frac{b-a}{2}} \sigma_{xx} dy = P \sin(-\alpha), \int_{-\frac{b-a}{2}}^{\frac{b-a}{2}} \sigma_{xy} dy = -P \cos(\alpha), \int_{-\frac{b-a}{2}}^{\frac{b-a}{2}} \sigma_{xx} y dy = 0 \end{cases} \quad (2.22)$$

Those weak boundary conditions work well for long serpentines and would fail when α approaches -90^{o} and *l* approaches 0. This is because when α approaches -90^{o} and *l* approaches 0, the curve length of the serpentine is comparable with or even smaller than the ribbon width and Saint-Venant's principle no longer holds. Violation of

Saint-Venant's principle imply that the weak boundary condition is no longer applicable to short serpentines with α close to -90^{o} and *l* close to 0. One way to resolve this issue is to find the point-wise traction and apply the exact boundary condition to the stress functions and the stress functions, if they do exist, will be very complicated. Another approach to tackle this issue is to make the minimum number of modifications to the solution based on weak boundary conditions. We took the second approach and consider that the reaction force *P* on the arc is applied not at the median line of the ribbon, but with an offset of *c*, as highlighted in Figure 2.5 (d).

After deriving the stress fields from the stress function and the weak boundary conditions, the displacement fields for the arc and the arm can be obtained through constitutive and geometric equations. Weak displacement continuity conditions are adopted at the arm-arc interface:

$$\begin{cases} 1.\, u_{\mathrm{arm}|x=0,y=-\mathrm{d}} = 0 \\ 2.\, v_{\mathrm{arm}|x=0,y=-\mathrm{d}} = 0 \\ 3.\, \phi_{\mathrm{arm}|x=0,y=-\mathrm{d}} = \phi_{\mathrm{arc}|r=\frac{\mathrm{a+b}}{2}+\mathrm{d},\theta=\frac{\pi}{2}+\alpha} \end{cases}, \tag{2.23}$$

which essentially requires that the displacement and rotation of arc and arm are continuous through one point which is offset *d* to the middle line, as shown in Figure 2.5(e). As we pointed out before, the solutions to *c* and *d* are only valid when $\alpha \to -90^{o}$, as α grows from -90^{o}, the effect of weak boundary conditions on the stress field decays, thus *c* and *d* should vary with α. Simply assuming a quadratic variation, we propose the full solutions to be

$$c_{(\alpha)} = \begin{cases} c\dfrac{4\alpha^2}{\pi^2} & \alpha \le 0^{o} \\ 0 & \alpha > 0^{o} \end{cases}, \qquad d_{(\alpha)} = \begin{cases} d\dfrac{4\alpha^2}{\pi^2} & \alpha \le 0^{o} \\ 0 & \alpha > 0^{o} \end{cases} \tag{2.24}$$

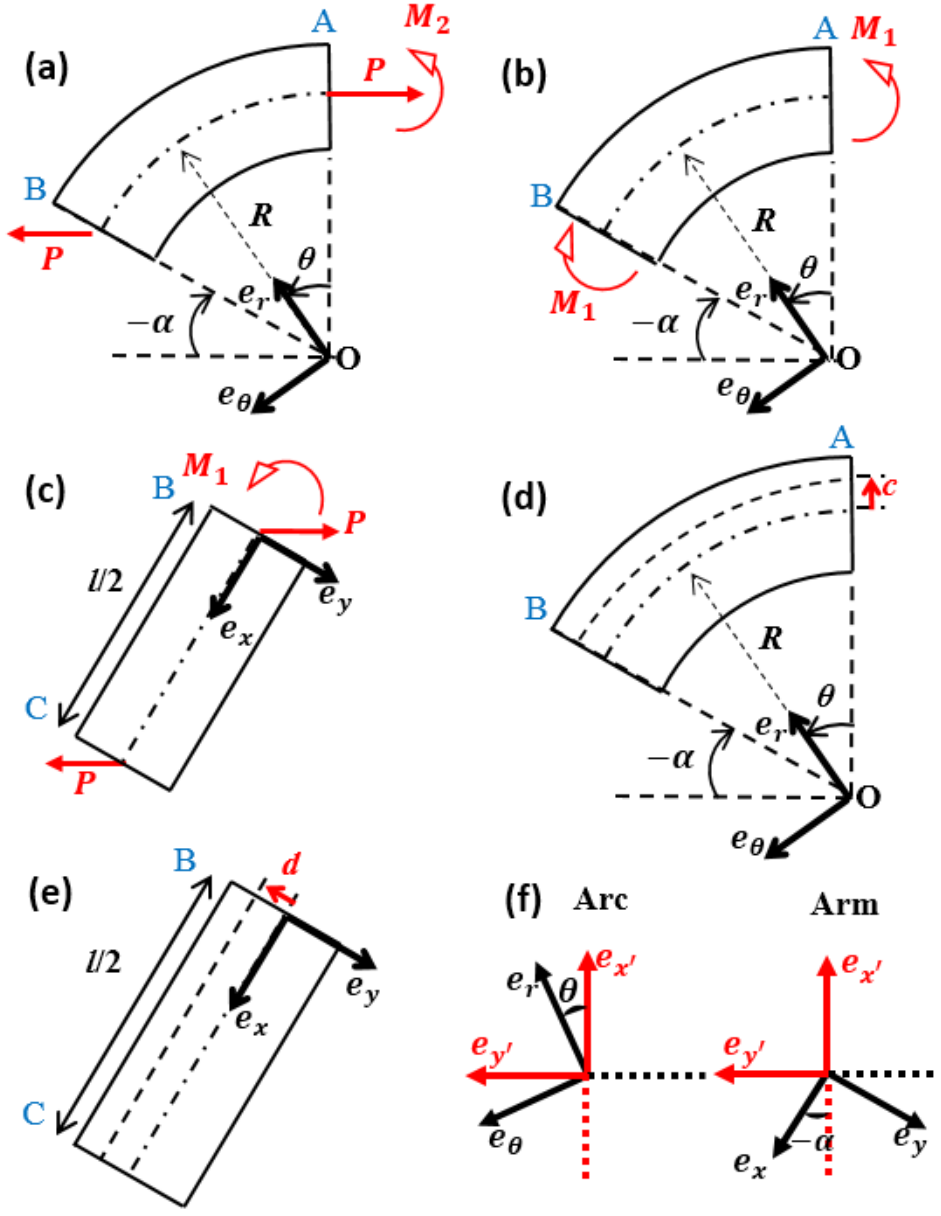

Figure 2.5 Boundary conditions for sub-problems for (a)&(b) arc and (c) arm (d). Offset of middle line for (d) weak boundary condition and (e) continuity condition. (f) Illustration of the local and global coordinate system.

So far, the stress, strain, and displacement were all derived in the local polar or local Cartesian coordinates. To establish results in the global Cartesian coordinate system, one more step of coordinate transformation has to be implemented. The global $\boldsymbol{e_{x'} - e_{y'}}$ coordinate along with each local coordinate are illustrated in Figure 2.5 (f) and the transformation angle for arc and arm are

$$\varphi_1 = -\theta, \varphi_2 = -(\pi + \alpha) \tag{2.25}$$

Through this coordinate transformation, the results are represented in the global Cartesian coordinate system. The total displacement is then formulated as

$$u_{app} = \frac{u_0}{2} = v'_{\text{arc}|r=\frac{a+b}{2}+d,\theta=\frac{\pi}{2}+\alpha} + v'_{\text{arm}|x=0,y=-d}, \tag{2.26}$$

and the maximum local strain always occurs at the center of the inner crest of the arc (as shown in Figure 2.4 (b)), i.e.

$$\varepsilon_{\max} = \varepsilon_\theta^{\text{arc}|r=a,\theta=0} \tag{2.27}$$

Finally, by combining Equations (2.2), (2.26) and (2.27) we can obtain elasticity solutions for $\varepsilon_{\max}/\varepsilon_{\text{app}} = f(w/R, l/R, \alpha)$ and $PS/(2\bar{E}wu_0) = g(w/R, l/R, \alpha)$

2.3.3 FEM Approach

The commercial FEM package ABAQUS 6.10 was used to perform a plane strain simulation of a unit cell as shown in Figure 2.2 (a). The serpentine material was assumed to be linearly elastic, with a Young's modulus E = 130 GPa, and a Poisson's ratio $\nu = 0.27$ (e.g. silicon). Symmetric displacement boundary conditions were applied at both ends to ensure $\varepsilon_{\text{app}} = 10\%$ for all the models. Small deformation (i.e. linear geometric relation) was assumed. After convergence tests, element size was smaller than w/40. Strain distributions and reaction forces were obtained directly from FEM solutions.

2.3.4 Comparison of CB and Elasticity Solutions

As an illustration, results for representative serpentine structures are shown in Figure 2.4. It is obvious that CB theory and elasticity results are in good agreement with FEM ones for narrow and wide serpentine structures, respectively, and the maximum strain always occurs at the inner crest of the arc.

Figure 2.6 (a)&(b) plot the normalized maximum strain $\varepsilon_{max}/\varepsilon_{app}$ as dots for FEM result, dash curves for CB theory result and solid curves for the elasticity result. The inset in each plot shows representative shapes for that plot and the parenthesized numbers below the serpentines show the x axis value for that serpentine shape. There are several useful insights in the plots. It is evident that for narrow serpentine structures the CB theory result aligns well with the FEM result, but for wide serpentine structures the good agreement no longer holds. By contrast, the elasticity solution reproduces the FEM result well for all serpentine structures. This is because CB theory makes certain assumptions, such as plane that is perpendicular to neutral axis remains normal during deformation, which only reflects the truth when the serpentine is narrow or the arm length is large. However, for serpentines with large ribbon width or short arm length these assumptions no longer hold, therefore CB beam theory fails to provide a faithful predication for wide serpentine structures. It has to be noted that even though elasticity has better performance, CB has its own advantage for prediction of narrow serpentine structures due to its simplicity for application.

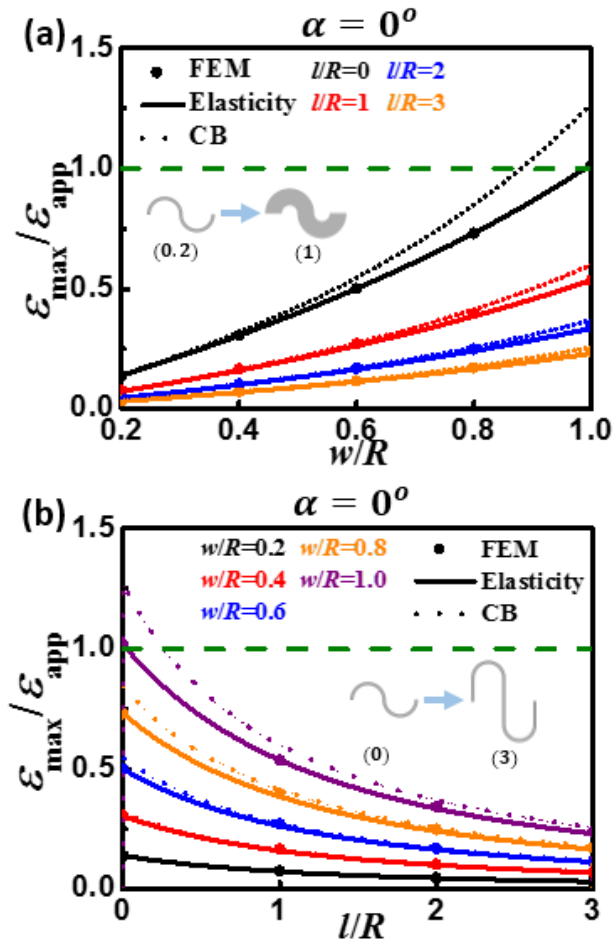

Figure 2.6 Normalized maximum strain result for serpentine with fixed α as a function of (a) ribbon width *w/R* and (b) arm length *l/R*.

2.4 EXPERIMENTS

Experimental validation of the analytical and FEM results was conducted with 3D-printed acrylonitrile butadiene styrene (ABS) straight and serpentine ribbons. Instron Dual Column Testing System (Model 3367) and Bluehill 2 were used as the uniaxial tension test and data acquisition system. Displacement-controlled tensile tests on the 3D-printed serpentine ribbons were performed with a strain rate of 0.1% s^{-1}. Engineering strains, i.e. total elongation divided by the initial gauge length, were measured in the experiments. The intrinsic material strain-to-rupture $\varepsilon_{\mathrm{cr}}$ was measured using a straight specimen whereas the applied strains-to-rupture (or stretchability) $\varepsilon_{\mathrm{app}}^{\mathrm{cr}}$ was measured for various serpentine ribbons. Although ABS is an elastic-plastic material and it ruptures within the plastic regime, the inner edge of the crest of the ABS serpentine is always subjected to pure tensile strain and small-scale yielding assumption has been validated for its failure [89], therefore the failure criterion $\varepsilon_{\max} = \varepsilon_{\mathrm{cr}}$ is still applicable. Comparison between modeling and experimental results is offered in Figure 2.7. Figure 2.7 (a) depicts the 3D printed serpentine specimens with systematically changing arm length. Every specimen shown in this figure has a thickness of 0.1 inch and a ribbon width of 0.039 inch. Because of their relatively large thickness, the serpentine specimens undergo in-plane elongation during the tensile tests, which is compatible with our plane strain assumption for the models. Measured $\varepsilon_{\mathrm{cr}}/\varepsilon_{\mathrm{app}}^{\mathrm{cr}}$ are compared with CB theory and FEM results as given by Figure 2.7 (b)&(c). Figure 2.7 (b) plots $\varepsilon_{max}/\varepsilon_{app}$ as a function of l/R with fixed $\alpha = 0^{o}$ and w/R=1/5 and Figure 2.7 (c) plots $\varepsilon_{max}/\varepsilon_{app}$ as a function of α with fixed w/R=1/5 and l/R=0. The experiment result shows good agreement with FEM and analytical results.

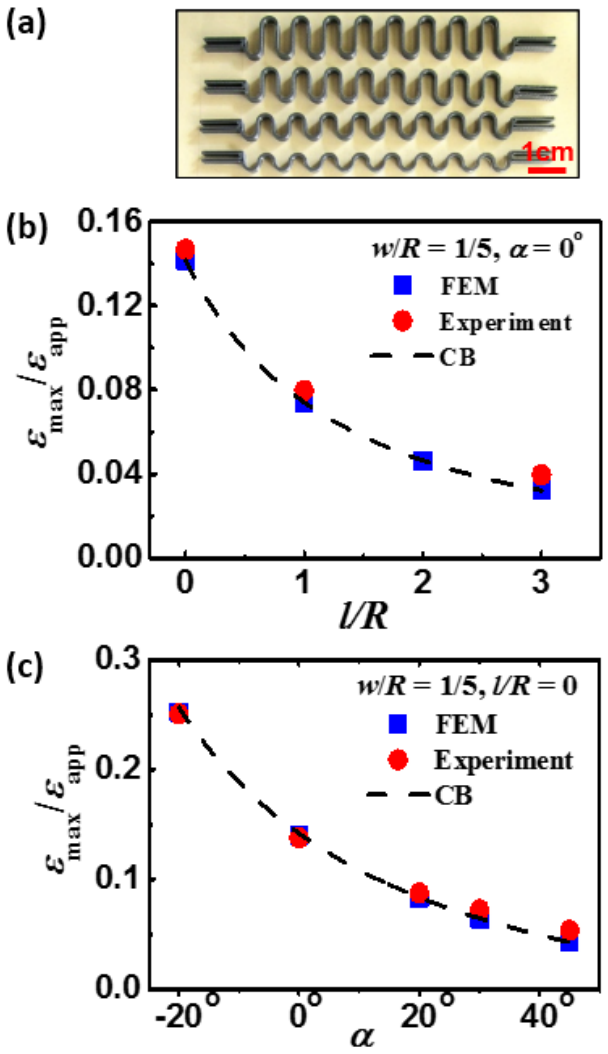

Figure 2.7 (a) 3D-printed thick serpentine ribbons to be tested by uniaxial tension. (b) Comparison of results from CB theory (dashed curve), FEM (blue markers), and experiments (red markers) for various l/R. (c) Comparison of results from CB theory (dashed curve), FEM (blue markers), and experiments (red markers) for various α at different w/R.

2.5 RESULTS

2.5.1 Shape Effect on Stretchability and Stiffness

Figure 2.6 suggests that when $\alpha = 0^o$, the normalized maximum strain $\varepsilon_{max}/\varepsilon_{app}$ depends monotonically on w/R and reversely monotonically on l/R, i.e. serpentine with smaller ribbon width and longer arm exhibits smaller $\varepsilon_{max}/\varepsilon_{app}$, therefore higher stretchability. This is because the applied strain is mainly accommodated by the rotation of the arm in such a way that only moderate strains will be induced in the arc. Figure 2.8 (a)&(b) plot the maximum strain result as function of arc angle α for narrow serpentine ($w/R = 0.2$) and wide serpentines ($w/R = 1$), respectively. It can clearly be seen that the effect of α is not a simply monotonic function on $\varepsilon_{max}/\varepsilon_{app}$. When α approaches -90^o, i.e. the serpentine becomes closer to a straight ribbon, $\varepsilon_{max}/\varepsilon_{app}$ first increases until it reaches a peak value and then decreases and ends up at 1 when $\alpha = -90^o$, for both narrow serpentine and wide serpentine structures. It is also obvious that in the full range of α examined in the two plots, a large portion of the curve is above 1 (green dashed curve in Figure 2.8 (a)&(b)) , which means that the stretchability of those serpentine shapes is actually smaller than their straight counterparts. For the serpentine shapes examined, the arc angle α corresponding to the curve that is above 1 is always negative and close to -90^o, which indicates the maximum strain augmentation always happens in a less tortuous (for wide serpentine) or almost straight serpentine structure (for narrow serpentines). The plots reveal that serpentine structures are not always more favorable in the sense of gaining higher stretchability, and actually a big portion of the serpentine structures are less stretchable than their straight ribbon counterparts, which might be contrary to intuition. Therefore in order to design a high stretchable serpentine structure, a specific serpentine structure should be carefully evaluated before to conclusions.

Other than stretchability, the effective stiffness is also of great importance for the

serpentine structure since it reflects how "compliant" the structure is. Figure 2.8 (c)&(d) plot the effective stiffness of serpentine ribbons normalized by that of a straight ribbon for both narrow ($w/R = 0.2$) and wide serpentines ($w/R = 1$), respectively, in semi-log scale. It is obvious that, again, the elasticity result finds good agreement with FEM result while CB theory result exhibits significant discrepancy, especially when $w/R = 1$. It shows that the all of the three parameters have a monotonic effect on the effective stiffness, i.e. the effective stiffness monotonically increases with increasing w/R and monotonically decreases with increasing l/R and α. Both of the plots show that the effective stiffness of serpentines are always smaller than 1, which indicates the serpentine structure is always "more compliant", even though it is not always more stretchable, than a straight ribbon. Actually the stiffness of a serpentine can be orders of magnitude smaller than a straight ribbon, which is the enabling mechanism for making tissue-like electronics out of stiff inorganic materials [48, 63, 90, 91].

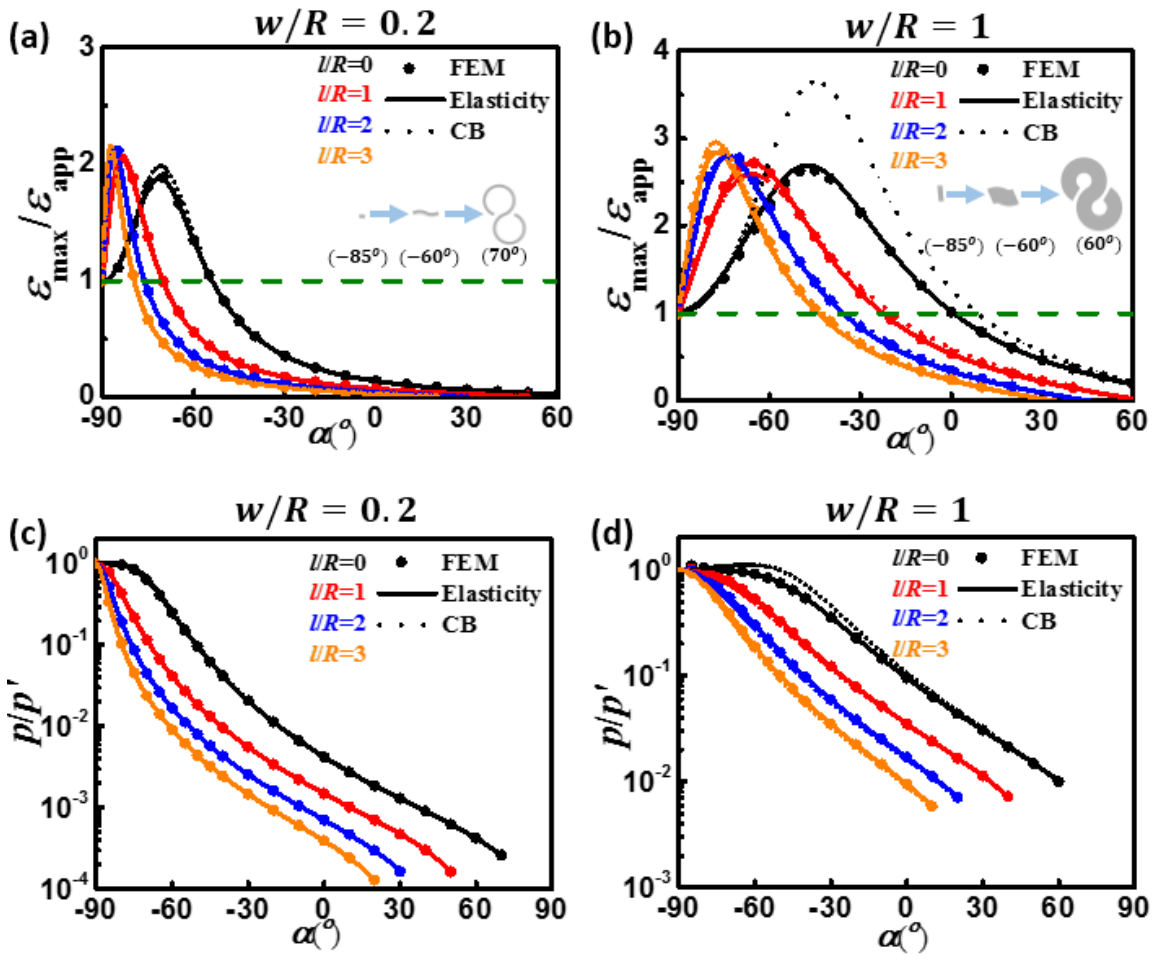

Figure 2.8 Maximum strain result for serpentine with (a) fixed $w/R = 0.2$ and (b) fixed $w/R = 1$. Effective stiffness of serpentine with (c) fixed $w/R = 0.2$ and (d) fixed $w/R = 1$.

2.5.2 Optimized Serpentine Shape

In practical circuit design, stretchable serpentine interconnects are usually subjected to design and fabrication constraints. For example, although narrower serpentines are always more compliant and more stretchable, the width of serpentines cannot approach zero due to limitations in fabrication resolution as well as electrical resistance considerations. Assuming that a practically realizable minimum width is pre-determined, this section will demonstrate how to construct the most stretchable serpentine shape with CB theory. For a given w, the mathematical procedure of finding out the optimal shape under certain geometric constraints is to identify three equations to solve for the three unknowns, w/R, l/R and α. The first equation comes from the non-overlapping requirement, i.e. the distance between the two nearest ribbons, X as defined in Figure 2.9 (a) should be larger or equal to 0, i.e.

$$X = \left(R - \frac{w}{2}\right)\cos(\alpha) - l\sin(\alpha) - \left(R + \frac{w}{2}\right)(1 - \cos(\alpha)) = 0. \tag{2.28}$$

Solving this equation, we can obtain the largest possible α for given (w/R, l/R) combinations. The second equation reflects the finite breadth constraint when considering limited real estate on the circuit board, e.g. $Y = 10w$, where the breadth Y is defined in Figure 2.9 (a)

$$Y = 2R + w + 2R\sin(\alpha) + l\cos(\alpha) = 10w. \tag{2.29}$$

The third equation is the minimization of $\varepsilon_{max}/\varepsilon_{app}$, i.e. minimizing the values given by Equation (2.13). Since the optimization problem now reduces to a problem of minimization under two constraints, we can certainly use Lagrangian multipliers. Therefore, with given constraints of w and Y, the most stretchable serpentine shape is depicted in Figure 2.9 (b). Shape optimization under other geometric constraints can be formulated following similar approaches.

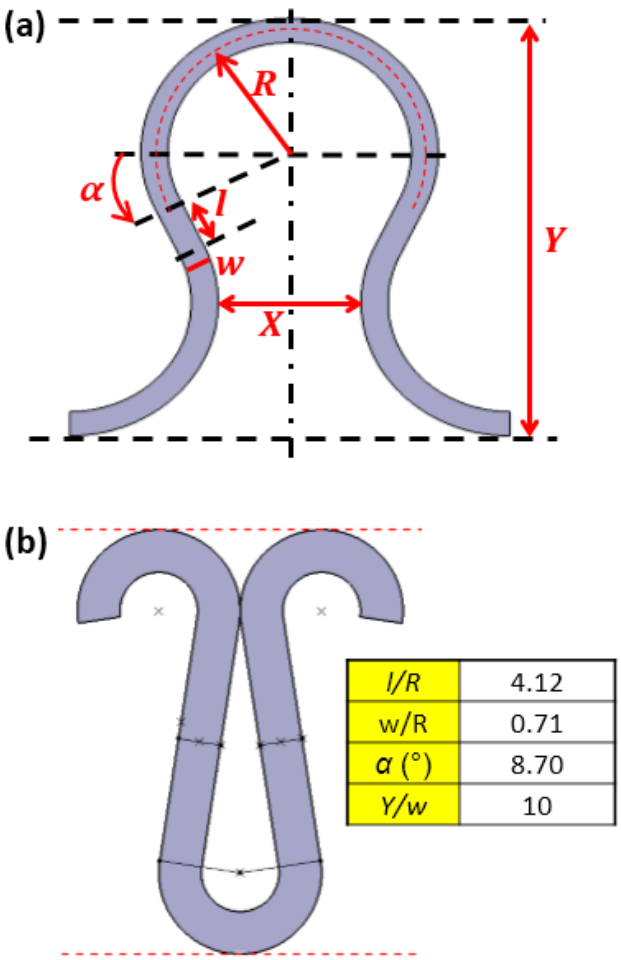

Figure 2.9 (a) Illustration of geometric constraints. (b) Optimal serpentine shape under the constraint of $X = 0$ and $Y = 10w$.

2.6 DISCUSSIONS

There is another large group of non-buckling serpentine structures that has been widely used for stretchable electronics [92-96]. For this group of structures, the thick, non-buckling serpentines of stiff metal are embedded in a polymer matrix, so that the polymer matrix can physically protect and support the conductive serpentine pathway. The existence of the polymer matrix may affect the stretchability of the embedded serpentine structure. We have performed finite element analysis to reveal $\varepsilon_{\max}$ in the serpentine structure when the polymer matrix is uniaxially stretched. Figure 2.10 (a) shows the FEM model for both freestanding and embedded serpentine structures and Figure 2.10 (b) plots $\varepsilon_{max}/\varepsilon_{app}$ as a function of the matrix modulus E_{matrix} against the CB (dashed line) and elasticity (solid line) solutions for freestanding serpentines, which are flat since they are independent of E_{matrix}. It shows that, when $E_{\text{matrix}} < 100$ MPa, the FEM results agree well with the analytical solutions for freestanding serpentines, which indicates that compliant polymer matrices have almost no effect on serpentine stretchability.

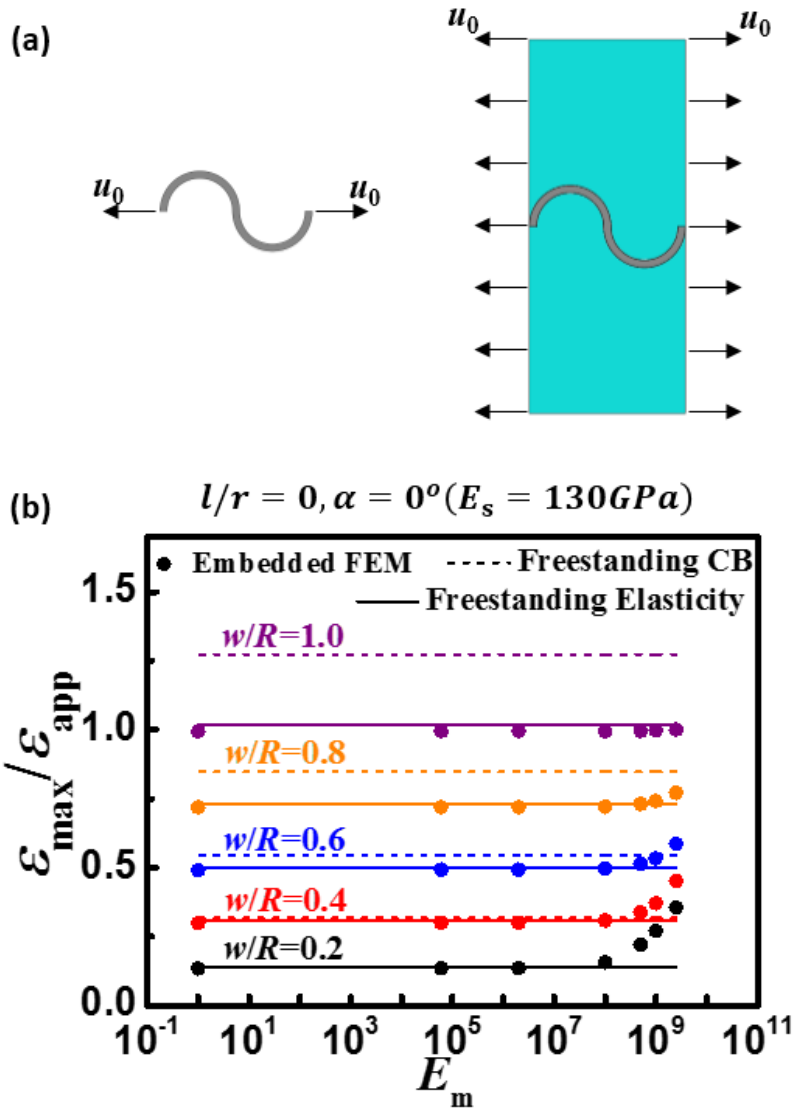

Figure 2.10 Matrix stiffness effect for embedded serpentine. (a) Boundary conditions for freestanding and embedded serpentine. (b) $\varepsilon_{\max}/\varepsilon_{\text{app}}$ as a function of the matrix modulus E_{matrix} against the CB (dashed line) and elasticity (solid line) solutions for freestanding serpentines.

2.7 CHAPTER SUMMARY

In this chapter, we have adopted both CB theory and linear elasticity to study the stretchability and effective stiffness of non-buckling freestanding serpentine structures. We have also carried out FEM and experimental studies to validate these theories. While CB theory only captures the strain and effective stiffness of narrow serpentines (ribbon width to arc radius ratio is small), elasticity solutions are valid for both narrow and wide serpentines. Surprisingly, we find that not all serpentines are more stretchable than their linear counterparts, but they are always more compliant. Therefore, the optimization of serpentine shapes relies on the theories we have developed and has been demonstrated under practical constraints. When non-buckling serpentines are embedded in a polymer matrix, we find that the matrix has no effect on serpentine deformations when it is more than three orders of magnitude more compliant than the serpentine material. However, when thin serpentine ribbons are bonded to polymer surfaces, both compliant and stiff polymer substrates may affect the mechanical behavior of the serpentines. Such situations will be discussed in the next chapter.

Chapter 3 Substrate-Supported Serpentines[1,2]

Other than freestanding serpentine structures, in many applications, stiff serpentine thin films are supported by stiff or compliant polymer substrates, which help maintain the integrity or bio-integration of the device. In such structures, the substrate stiffness and serpentine-substrate adhesion may affect the stretchability of the serpentine thin films. In this chapter, systematic experimental and numerical studies are conducted to investigate those effects using indium tin oxide (ITO) as a representative brittle material. As ITO is electrically conductive, serpentine ITO ribbons are stretched using *in situ* resistance measurement to indicate the mechanical failure, which is validated by *in situ* scanning electron microscope (SEM) and optical microscope observation.

---

[1] S. Yang, B. Su, G. Bitar, N. Lu*, "*Stretchability of indium tin oxide (ITO) serpentine thin films supported by Kapton substrates*," International Journal of Fracture, vol. 190, no. 1-2, pp. 99-110, Nov, 2014.
Author contributions: S. Y. conducted device design, FEM and analytical analysis. S. Y., B. S. and G. B. performed fabrication and testing. N. L. supervised and coordinated the project. N. L. and S. Y. wrote the paper.

[2] S. Yang, E. Ng, N. Lu*, "*Indium Tin Oxide (ITO) serpentine ribbons on soft substrates stretched beyond 100%*," Extreme Mechanics Letters, vol. 2, pp. 37-45, Jan, 2015, 2015.
Author contributions: S. Y. conducted device design and FEM analysis. S. Y. and E. N. performed fabrication and testing. N. L. supervised and coordinated the project. N. L. and S. Y. wrote the paper.

3.1 OBJECTIVE AND OVERVIEW

Although freestanding serpentine structures can provide extraordinary stretchability and compliance, they have a hard time to maintain their shapes without any underlying support. Therefore, bonding serpentine ribbons to polymer substrates is a popular strategy for building stretchable electronics [71, 76, 77, 91, 97-103]. Because of the constraint provided by the polymer substrate, the mechanical behavior of the serpentine ribbons can be very different from their freestanding counterparts. Such constraint is dictated by the substrate stiffness as well as the serpentine-substrate adhesion [86].

In the field of flexible electronics, polymers such as polyimide and polyethylene terephthalate (PET) are popular substrates on account of their mechanical stiffness which protects electronic components they host from accidental stretches. For example, Kapton, which is a polyimide film developed by DuPont, has been widely used in the fabrication of novel flexible devices such as flexible displays [9, 104], rollable solar cells [105], flexible 2D electronics [28, 29] and photonics [19], and energy generators [99, 101]. As a transparent, conductive material, indium tin oxide (ITO) is widely used in conventional rigid displays [106-108], touch panels [109-111] and solar cells [112-114]. However, it is too brittle to be used in highly flexible devices, even when patterned into serpentine shapes on Kapton or PET substrates. This suggests that serpentines do not always enhance deformability, and that substrate can play a significant role in serpentine behavior.

By contrast, serpentine structures have proved to be very successful in stretchable electronics when the substrates are stretchable polymers such as elastomers [115, 116], stretchable medical tapes, i.e. Tegaderm (3M) [91], and elastic fabrics [10]. Examples include epidermal electronics [63], inflatable balloon catheters [5], 3D “heart sock” [117, 118], stretchable lithium ion batteries [71] and stretchable antennae [119, 120]. This suggests substrate compliance is a critical condition for serpentines to be stretchable.

The mechanics of polymer supported serpentines have been studied by many researchers. The mechanics of metallic serpentines has been studied extensively through both experimental [70, 84, 86, 95] and theoretical/numerical means [83, 87, 88, 121]. Except for metal-based devices, stretchable continuous ceramic structures have also found wide application where high stretchability and large areal coverage is needed. For instance, filamentary serpentine single crystalline silicon has been transfer-printed onto elastomers for stretchable amplifiers and solar cells [63]. Stretchable ceramics such as lead zirconium titanate (PZT) ribbons [122] and zinc oxide (ZnO) ribbons [123] are used in biomechanical energy harvesting applications due to their superior piezoelectric properties [124]. However, up to now, ceramic serpentine ribbons are far less used than metal serpentines, due to their challenging fabrication processes and less understood mechanical behavior. While stretchable metallic serpentine ribbons can be fabricated on polymer substrates by thin film deposition and patterning through either lift-off [84, 85] or etch-back [70, 86] processes, so far no simple method is available for the fabrication of ceramic serpentine ribbons on stretchable substrates. The only successfully demonstrated method is to transfer-print ceramic nanomembranes (either silicon or ZnO) from silicon on insulator (SOI) wafer to polymer substrates and patterning through dry etching can be done before or after transfer [63, 123]. The stretchability of these brittle serpentine ribbons, however, has never been tested.

This chapter presents systematic experimental and numerical studies of the mechanical behavior of brittle serpentines supported by stiff and compliant substrates. ITO is chosen as a representative brittle material in this study in order to avoid plasticity so that electrical resistance can be used as a simple indictor of the mechanical integrity of the serpentine ribbons. Using *in situ* electro-mechanical stretch tests, the effects of serpentine geometry, substrate stiffness and serpentine-substrate adhesion are studied.

3.2 FABRICATION

3.2.1 Serpentine on Kapton

Serpentine on Kapton was fabricated through thin film deposition. Polyimide foils (Dupont Kapton 50NH, 12.7 μm) were cleaned in acetone and then isopropyl alcohol (IPA) in an ultrasonic cleaner followed by deionized Water rinse. After dehydration, the cleaned Kapton was covered by a molybdenum stainless steel stencil (Towne Technologies, Inc.) with straight and serpentine-shaped openings and then loaded in a sputter deposition chamber (AJA International, Inc.). The Kapton substrate was first cleaned with argon (Ar) plasma in RF power when the base pressure reaches 5×10^{-6} torr. Immediately after cleaning, 200 nm thick ITO was then sputtered from an ITO target (Kurt J. Lesker) onto the Kapton substrate through the openings on the stencil with a working gas pressure of 2×10^{-3} torr and a RF power of 65 W. After deposition, the stencil was removed and specimens were cut into rectangular pieces, each including a group of four to five ITO serpentine ribbons with systematically varied shapes, as shown in Figure 3.1 (a)

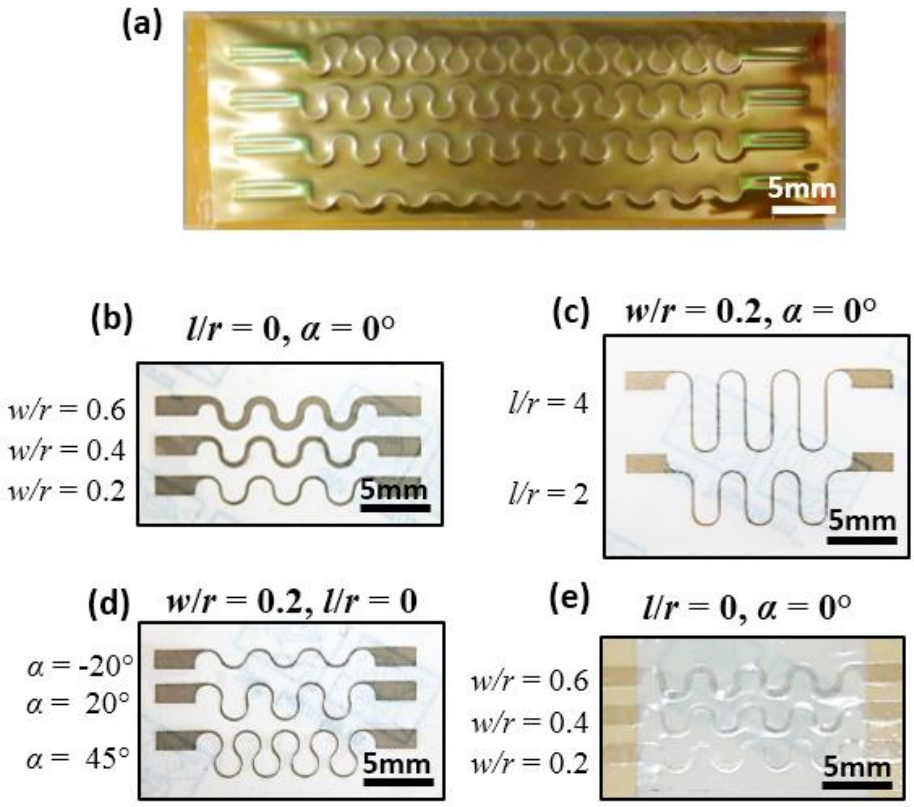

Figure 3.1 Pictures of the specimen. (a) Top view of a group of four ITO serpentine thin films sputtered on a 12.7 μm thick Kapton substrate. (b)-(d) Top view of three groups of well-bonded ITO serpentines with systematically varied geometries. (e) A picture of a weakly-bonded ITO displays good transparency.

3.2.2 Serpentine on Tegaderm

While ITO can be directly deposited onto stiff polymeric substrates like Kapton or PET, it's never an easy task to directly deposit brittle materials onto compliant substrates. This is because during deposition, the huge mismatch in the Young's moduli of the brittle material and compliant substrate will induce wrinkles in the as-fabricated sample, as shown in Figure 3.2 (a). And again, due to this huge mismatch in materials' stiffness, channel cracks in the stiff ceramic material will be easily triggered by even mild mechanical operations, such as sample removal from the sample holder of the deposition system, as shown in Figure 3.2 (b). Since ITO is too brittle to be directly deposited onto compliant substrates, an alternative fabrication method has to be used to make the compliant substrate-supported samples.

We successfully developed a completely dry patterning and transfer process to bond ITO serpentine ribbons either weakly or strongly to compliant substrates. The whole process is illustrated is Figure 3.3. Figure 3.3 (a) shows a piece of 13 μm thick transparent polyethylene terephthalate (PET) film (Goodfellow Corp.) pre-cleaned by acetone and isopropyl alcohol (IPA) and attached to a thermal release tape (TRT) (Semiconductor Equipment Corp.), which is supported by a cutting mat. The cutting mat is fed into an electronic cutting machine (Silhouette Cameo) which can cut the PET with serpentine-shaped seams as shown in Figure 3.3 (b). The cut PET on TRT is peeled off the cutting mat (Figure 3.3 (c)) and loaded into a magnetron sputter system (AJA International, USA) where 200 nm thick ITO is deposited from an ITO target (Kurt J. Lesker Company) on the PET with base pressure of 1.0×10^{-7} torr, working gas (argon) pressure of 2.0×10^{-3} torr, and RF power of 60 W (Figure 3.3 (d)). After deposition, the ITO covered PET is transferred to another TRT as shown in Figure 3.3 (e). To achieve well-bonded serpentines, 5 nm Ti and 50 nm SiO_2 are sputtered on the backside of PET, i.e., the surface

not covered by ITO, as shown in Figure 3.3 (f). When the TRT is heated to 115 °C on a hot plate, the excessive PET can be easily peeled off, leaving only serpentine ribbons on the TRT (Figure 3.3 (g)). The serpentine ribbons can be transferred onto Tegaderm (3M), a transparent wound dressing polymer tape with thickness of 47 μm and Young's modulus of 7.43 MPa, whose adhesive surface is treated by ultraviolet ozone (UVO) for 5 minutes (Figure 3.3 (h)), rendering the final sample as shown in Figure 3.3 (i). UVO treated polymer surfaces are hydrophilic and able to form strong chemical bonding through condensation reactions with the SiO_2 layer deposited on the backside of the PET. For weakly-bonded samples, SiO_2 deposition (Step (f)) and UVO treatment of Tegaderm are omitted, but the native adhesive on Tegaderm can still ensure successful transfer of the serpentine ribbons. The whole process takes less than 15 minutes excluding the deposition time and the yield is almost 100%. Other than brittle materials, it has also been proven that this "cut-and-paste" method is effective in patterning metal-on-polymer laminates, which will be discussed in the next chapter. With this new fabrication method, ITO serpentine ribbons weakly- and well-bonded on compliant Tegaderm substrate can be fabricated and the top views are shown in Figure 3.1 (b)-(e). Figure 3.1 (b)-(d) show groups of as-fabricated, well-bonded ITO/PET serpentines on Tegaderm. While thin ITO film should exhibit high transparency, the dark color of the serpentine ribbons in the well-bonded samples is due to the presence of the Ti and SiO2 adhesive layers. Figure 3.1 (e) shows the weakly-bonded serpentines without the Ti and SiO2 layers and the transparency of ITO thin film is evidenced.

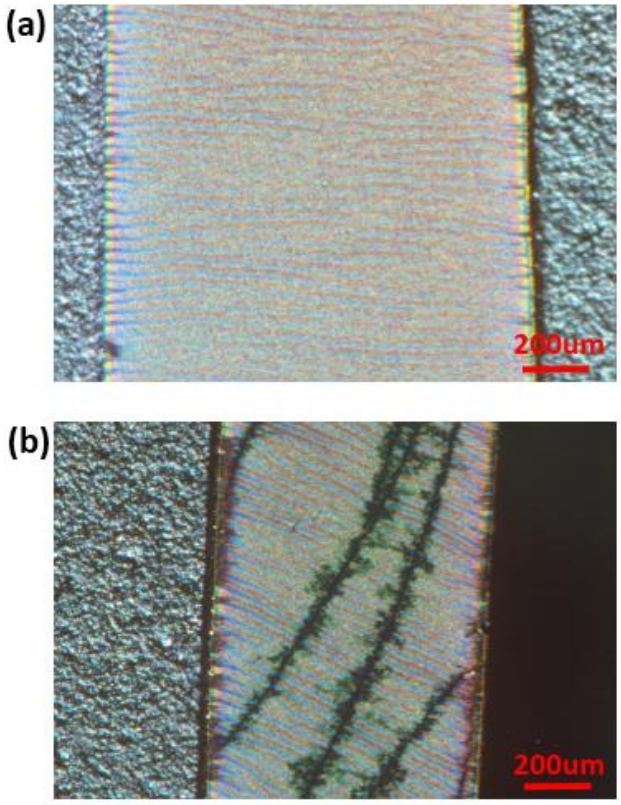

Figure 3.2 ITO thin film directly deposited onto 10:1 PDMS substrate with sputter deposition system. Scotch tape adhered to the PDMS on both sides for sealing purpose. (a) Top view for sample right after deposition. Due to the different thermal expansion coefficients of ITO and PDMS, wrinkles develop in the as-fabricated sample. (b) Top view for samples with Scotch tape peeled off to the right side of the ITO film. Due to the brittleness of ITO thin film, channel cracks develop as a consequence of a relatively mild mechanical operation.

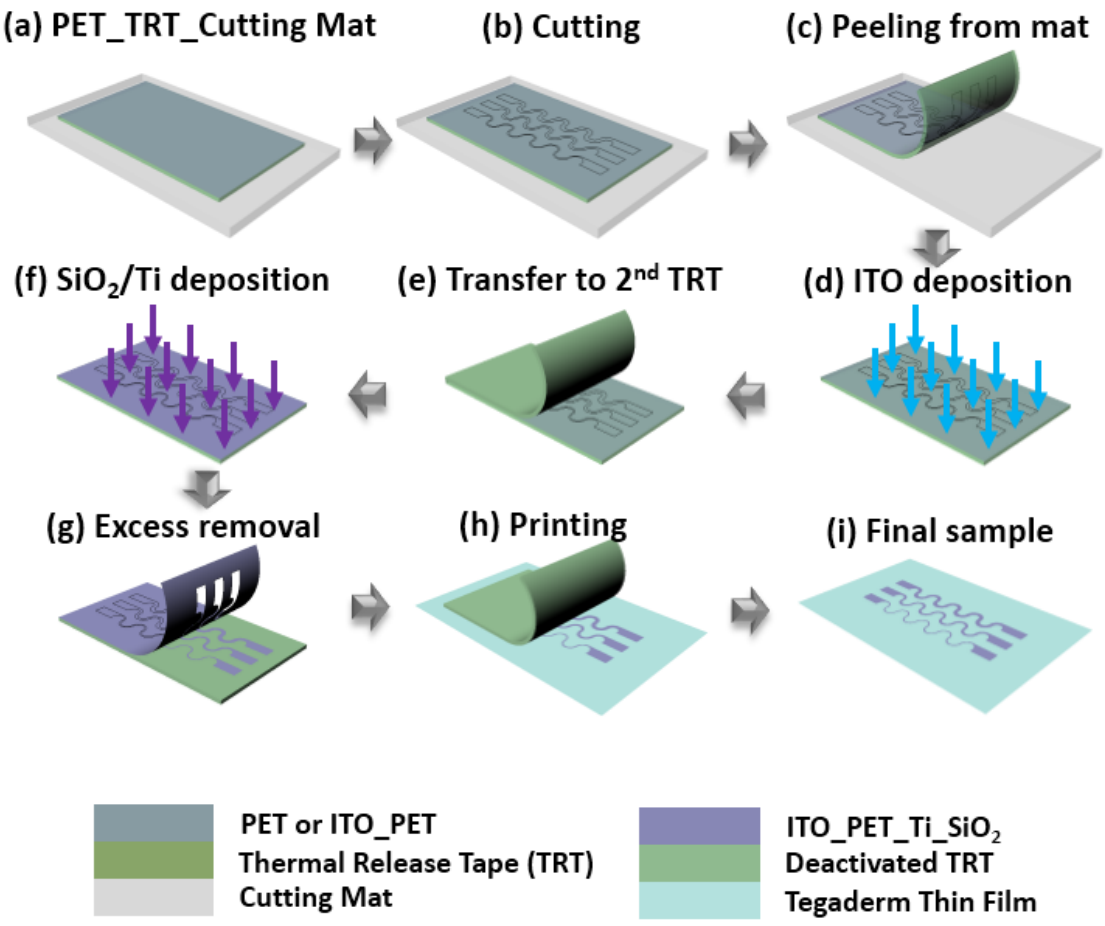

Figure 3.3 Schematics of the dry, bench top fabrication process of stretchable ITO serpentines on Tegaderm: (a) laminating 13 μm thick PET on TRT on cutting mat. (b) using an electronic cutter to carve serpentine-shaped seams on PET. (c) peeling TRT-supported PET from the cutting mat. (d) sputtering 200 nm thick ITO on PET. (e) transferring ITO covered PET from one TRT to another with the backside of PET exposed. (f) sputtering 5 nm Ti and 50 nm SiO2 on the backside of the PET (for weakly-bonded serpentines, this step is skipped). (g) removing unwanted PET, leaving only ITO_PET serpentines on the TRT. (h) printing the ITO_PET serpentine ribbons on Tegaderm. (i) the final sample.

3.3 METHODS

3.3.1 Electrical Resistance Measurement

Since ITO is mechanically brittle and electrically conductive, resistance vs. applied strain curves have been widely adopted to indicate the overall mechanical integrity of thin ITO films as a function of strain [125, 126]. Figure 3.4 (a) shows the schematic for the experimental setup for Kapton-supported ITO specimen. To perform uniaxial tension tests, Kapton sheets with a group of ITO serpentine ribbons are gripped on a home-made stretcher and applied displacements are obtained by measuring the change of the gauge length between the grips. The applied strain, ε_{app}, is then calculated as the ratio of the applied displacement to the initial gauge length. The ITO films are connected to external multi-channel data acquisition (DAQ) system (NI USB-6225) through an anisotropic conductive film (ACF). The data acquisition system is configured to conduct simultaneous resistance measurements up to five channels, which enables the resistance change of each serpentine ribbons in the same group to be monitored simultaneously. The normalized resistance vs. applied strain result for a straight ITO specimen is provided in Figure 3.4 (b). Due to the brittle nature of the ITO thin film, channel cracks will develop when the local strain reaches the material's intrinsic failure strain and it will not take too long for the film to completely lose its electrical conductivity, which is reflected by the sudden increase of the curve in this plot. If we adopt the failure criterion of 10% deviation from initial resistance, the strain-to-rupture of a straight, Kapton-supported ITO sample is found to be 1.08%, which agrees with 1% from previous studies [125, 126], indicating that our electrical resistance measurement is a good indicator of the damage state in straight ITO ribbons.

Figure 3.5 (a) depicts the experimental setup for a Tegaderm-supported ITO specimen. It is almost the same as that of the Kapton-supported ITO specimen except that,

in this case, a webcam is used to perform top-down *in situ* observation of the failure behavior of serpentine ribbons when they are under uniaxial tension. Figure 3.5 (b) shows normalized resistance vs. strain curves for a straight sample and a typical serpentine-shaped sample, with an expanded view included as the inset. The plot shows that the stretchability of a straight ITO ribbon is around 1.12%. For the serpentine specimen shown in Figure 3.5 (b), whose shape is given by $w/r = 0.2, l/r = 2, \alpha = 0°$and whose adhesion to Tegaderm is weak, the stretchability is found to be 113%, which represents a 100 fold enhancement of the straight ITO stretchability. It is the first time that a continuous ITO ribbon can be stretched beyond 100%.

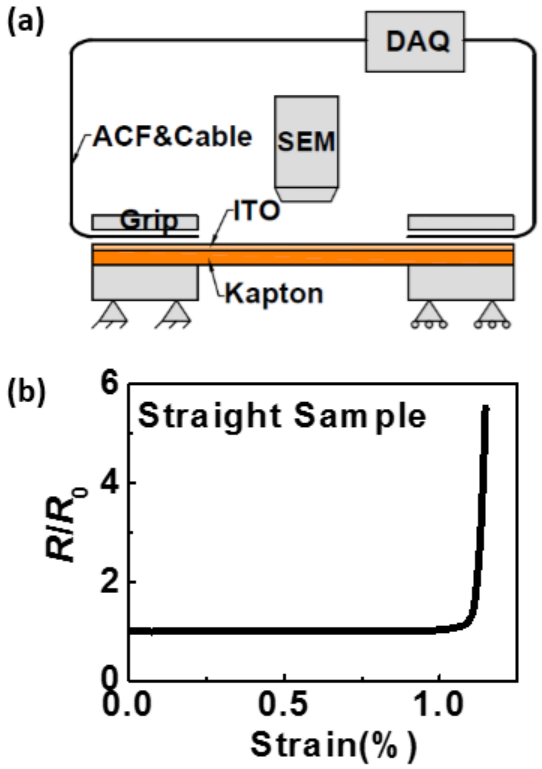

Figure 3.4 The electromechanical setup for Kapton-supported ITO specimen. (a) Schematics of the experimental setup for the *in situ* electrical resistance measurement of the ITO serpentines subjected to uniaxial tension. (b) A resistance vs. applied strain curve of a linear ITO ribbon on Kapton substrate.

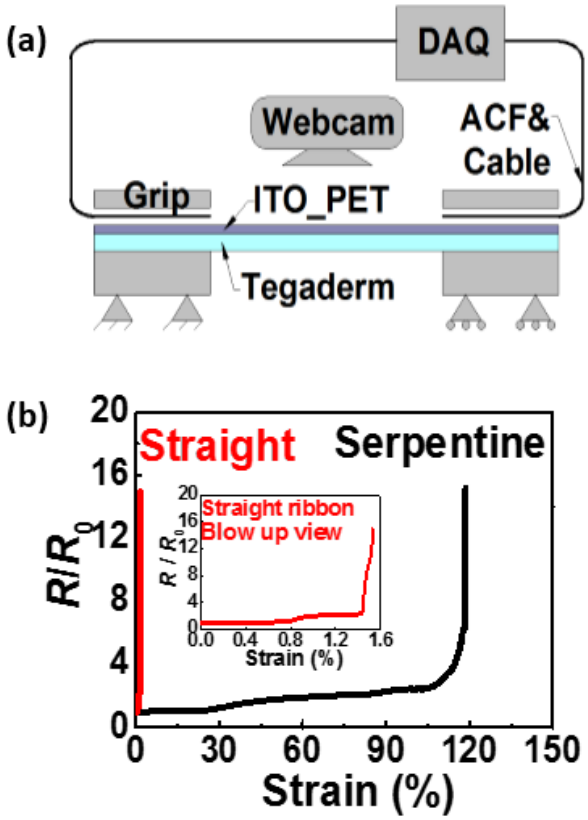

Figure 3.5 The electromechanical setup for Tegaderm-supported ITO specimen. (a) Schematics of the experimental setup for the *in situ* electrical resistance measurement of the ITO serpentines subjected to uniaxial tension. (b) Resistance vs. strain curves of a straight and a serpentine ribbon.

3.3.2 SEM Observation - Serpentine on Kapton

To validate that resistance measurement can also sufficiently reflect the damage state in serpentine thin films, we tried to compare the strain-to-rupture measured by crack density and electrical resistance. Semi-*in situ* scanning electron microscope (SEM) tension test was preformed to obtain the crack density vs. applied strain curve and the results are summarized in Figure 3.4. The SEM picture in Figure 3.4 (a) indicates that when the Kapton-bonded serpentine ribbons are subjected to uniaxial tension, the inner edge of the crest of the serpentine is where cracks like to initiate. This observation can later be explained by the strain concentration at the inner crest using FEM. We therefore focus on this area and obtain a series of snapshots at different levels of applied strain as shown in Figure 3.4 (b). The defect appearing in all snapshots serves as a reference point to align the frames. Starting with a crack free snapshot at $\varepsilon_{app} = 1.3\%$, a channel crack perpendicular to the tensile (horizontal) direction first emanates from the defect at $\varepsilon_{app} = 1.4\%$. Since then, the number of cracks within the rectangular box has gradually increased with increasing ε_{app}. A crack density vs. applied strain curve (black) can be offered in Figure 3.4 (c), along with the resistance vs. applied strain curve (blue) which is obtained from the semi-*in situ* electrical measurement. By adopting the "10% deviation" criterion, the strain-to-rupture deduced from the crack density measurements is 1.3% whereas it is determined to be 1.45% from the resistance measurement. Similar discrepancy between crack density and electrical resistance measurements has been observed in straight ITO-on-Kapton specimens [125, 126]. Figure 3.4 (d) offers a possible explanation to such discrepancy. Defects in ITO thin films induced either by imperfections in the Kapton substrates or during ITO deposition tend to give rise to half or misaligned channel cracks, as highlighted in Figure 3.4 (d). The presence of these types of cracks has less effect on the overall resistance of the ribbon compared to perfectly straight channel cracks shooting across the whole ribbon width.

Therefore there is a small strain lag when the sharp increase in the resistance curve is compared to the crack density curve. Despite the small lag, the resistance is able to capture the failure of the ITO serpentine in a much more experimentally economic way.

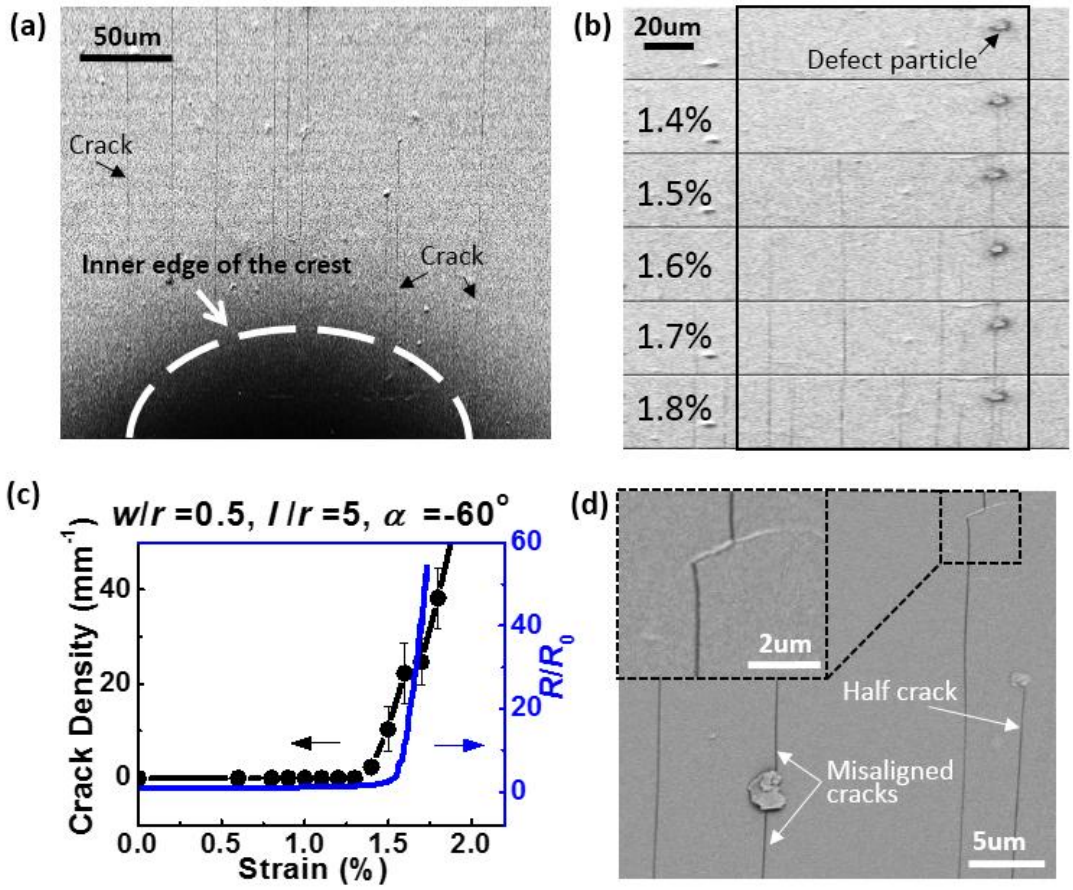

Figure 3.6 Channel cracks in ITO. (a) One of many SEM micrographs showing channel cracks emanating from the inner edge of the crest and propagating perpendicular to the tensile (horizontal) direction. (b) A sequence of SEM snapshots showing the evolution of crack density with increased applied strain. (c) The crack density and electrical resistance of an ITO serpentine as functions of the applied strain. Strains at which the curves blow up are defined as the strain-to-rupture. (d) Half or misaligned cracks are associated with defects in ITO films.

3.3.3 Optical Microscopic - Serpentine on Tegaderm

For Tegaderm-supported ITO serpentine structures, the failure behavior of the serpentine thin films depend on the serpentine geometry as well as the presence of the adhesive layer. The behavior of ITO serpentines during stretch was continuously observed by a top-down webcam. Two representative results are shown in Figure 3.7. Figure 3.7 (a) shows the deformation of a group of weakly-bonded serpentine samples with systemically varying ribbon width that are under 50% uniaxial stretch. It is evident that the narrowest serpentine, i.e. the one with $w/r = 0.2$, is almost fully debonded and straightened when it ruptures while the wider serpentines rupture before debonding, which has been validated by our electrical resistance measurement as will be discussed later. Figure 3.7 (b) shows the result for a well-bonded serpentine that has small ribbon width and long arm length. Due to the strong constraint from the substrate, compressive stress builds up in the serpentine arm, which is in the direction perpendicular to the stretch direction, which induces out-of-plane buckling of the arm, as shown in Figure 3.7 (b). The out-of-plane buckling will cause a large tensile strain in the top surface of the serpentine arm and therefore results in reduced stretchability, which has been confirmed by the electrical resistance measurement.

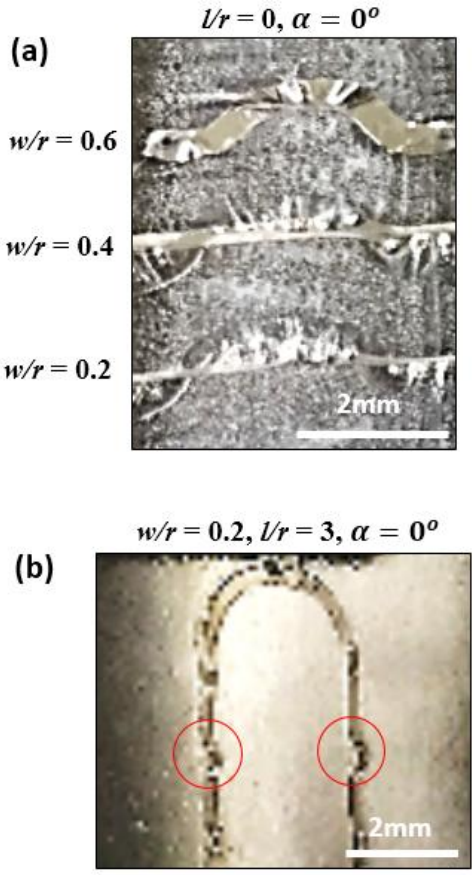

Figure 3.7 Optical top-down image for two representative Tegaderm-supported ITO serpentine samples. (a) A group of serpentines with varying ribbon width that are weakly bonded to Tegaderm substrate. (b) ITO serpentine with shape $w/r = 0.2, l/r = 3, \alpha = 0^o$ that is well bonded to Tegaderm substrate.

3.4 RESULTS

3.4.1 Serpentine on Stiff Substrate

For stiff substrate-supported structure, resistance results of different ITO serpentine shapes as a function of the applied strain are plotted in Figure 3.8. Figure 3.8 (a) studies the effect of w/r with l/r fixed to be 0 and α fixed to be 0º. It is evident that the width has a monotonic effect on the strain-to-rupture of the serpentine, i.e. the strain-to-rupture increases when w/r decreases. This indicates that provided the same arm length and arc opening angle, narrower serpentine ribbons are more stretchable. Among the four serpentine shapes we tested, the one with $w/r = 0.2$ exhibited a strain-to-rupture of 1.25%, which is 15.7% higher than the straight ribbons as shown in Figure 3.4 (b). Despite of the enhancement, the stretchability of ITO serpentine ribbons bonded to Kapton substrate is still far less than freestanding or elastomer-supported metallic serpentine ribbons [70, 83, 84, 86], due to first the constraint from the stiff Kapton substrate which suppresses both in-plane rigid body rotation and out-of-plane twist of the ribbons and second the intrinsic brittleness of the ITO. Figure 3.8 (b)&(c) suggest that the effect of arm length and arc opening angle on the serpentine stretchability are limited, which is due to the strong constraint from the stiff substrate on serpentine. Figure 3.8 (d) studies the effect of α for V-shaped serpentines, with w/r fixed to be 0.5, l/r fixed to be 0 and α varying from -60º to -15º. It shows that, although serpentines with α = -45º, -30º, and -15º share very similar stretchability, α = -60º serpentine clearly shows lower stretchability. All of these experimental observations can be explained by the FEM results.

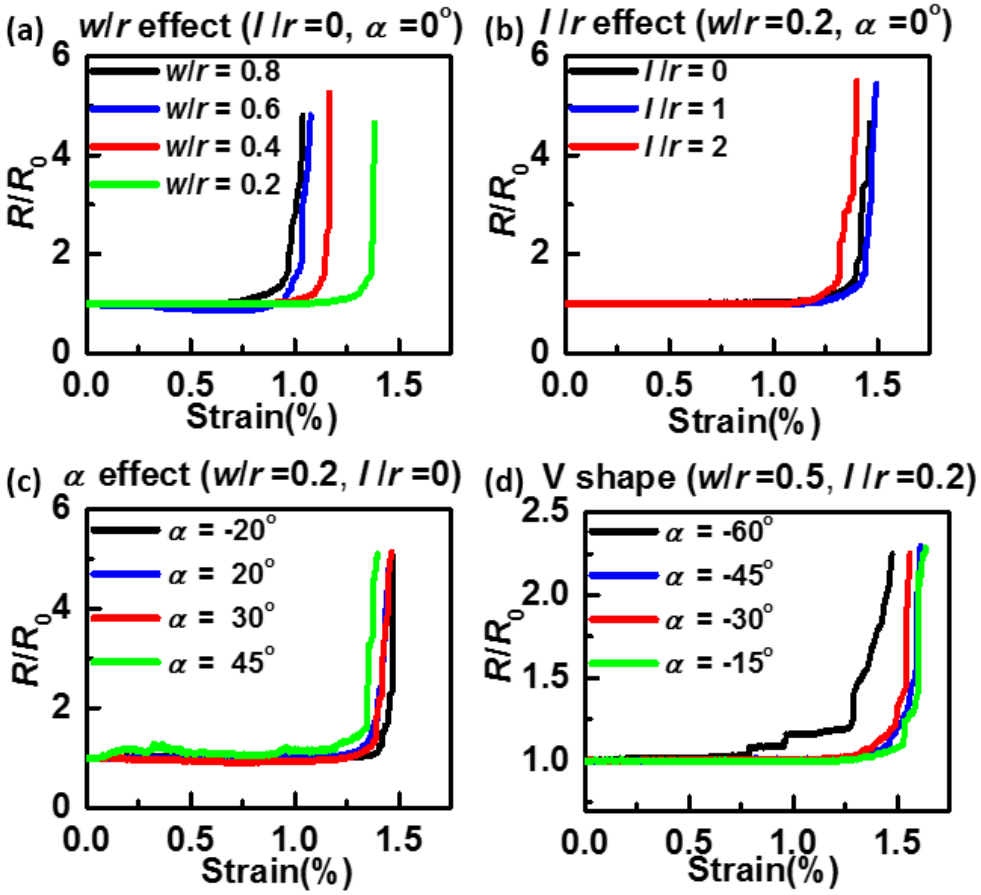

Figure 3.8 Results of the multi-channel electrical resistance measurement during uniaxial tensile tests. (a) Effect of *w*/*r*: smaller *w*/*r* leads to delayed resistance blow-up (b) Effect of *l*/*r* is negligible on the failure strain. (c) Effect of α on the stretchability of horseshoe-shaped serpentines is also negligible. (d) Effect of α on V-shaped serpentines is only significant when α falls in the far negative (less tortuous serpentines).

ABAQUS/CAE is used to build the finite element model of a unit cell of the Kapton-supported ITO serpentine as depicted in Figure 3.9 (a). Due to the large difference in the thickness of ITO and Kapton (200 nm vs. 12.7 μm), the ITO thin film is modeled by shell elements, whereas the Kapton substrate is modeled by 3D solid elements. ITO and Kapton are assumed to be linear isotropic materials with moduli of 118 GPa and 2.5 GPa, and Poisson's ratios 0.27 and 0.34, respectively. Tie constraints are applied between the substrate and the film and tensile strain ε_{app} = 1% is applied on the Kapton substrate along the *x* direction. Simulation results suggest the maximum strain always occurs at the inner edge of the arc, as shown in Figure 3.9 (b), which is consistent with our experimental observation. Based on Equation (2.3) the following equation should hold

$$\frac{\varepsilon_{max}}{\varepsilon_{app}} = \frac{\varepsilon_{cr}}{\varepsilon_{app}^{cr}} \tag{3.1}$$

which provides a way to quantitatively compare the FEM and experimental results. One representative comparison is plotted in Figure 3.9 (c), in which the black curve is the FEM result and the blue curve is the result from experiments. Therefore in the most ideal cases, the black and blue curves should fully overlap. Figure 3.9 (c) shows both methods justify the monotonic effect of ribbon width on the stretchability of Kapton-supported serpentine structure. It is worthwhile to note that in Figure 3.9 (c), for serpentine ribbons with $w/r > 0.4$, their stretchability is lower than that of straight ribbons, since the curves are about 1.

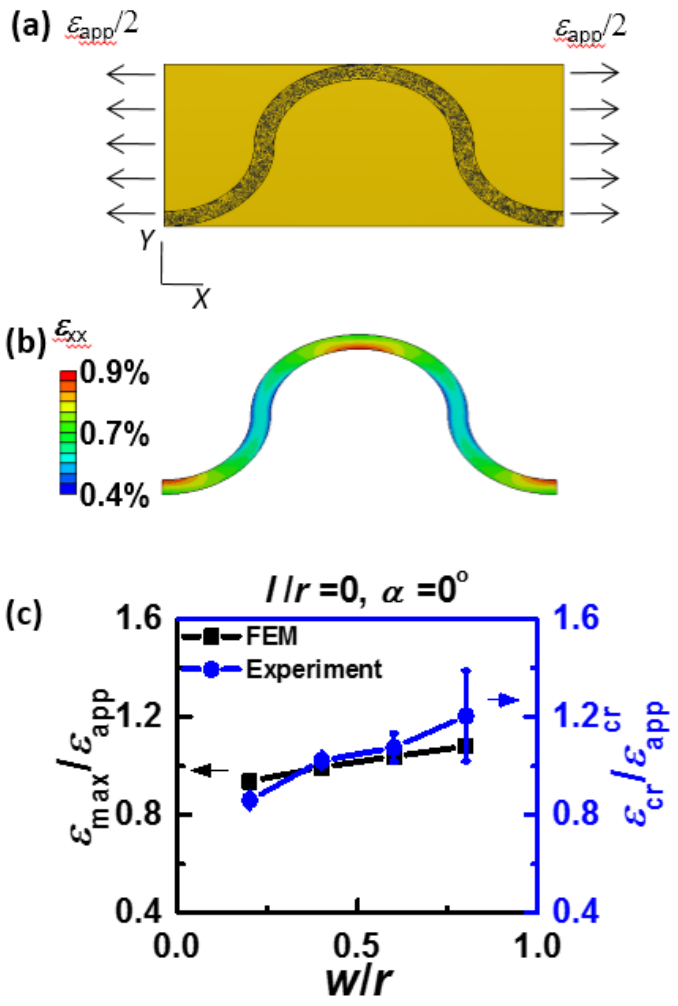

Figure 3.9 Comparison between FEM and experimental results. (a) Boundary condition and (b) contour plot of ε_{xx} of a unit cell serpentine under applied strain ε_{app} = 1% on the Kapton substrate. (c) Effect of w/r: narrower ribbons render lower strains.

Empirical geometry-stretchability relations have also been proposed to predict the stretchability of Kapton-supported serpentine thin films. In this analysis we use three new dimensionless geometric variables $b/s, b/r$ and w/h, where b is the breadth of a unit cell, and s and h are the total length and height of one unit cell, as labeled in Figure 3.10 (a). The three new variables are chosen in order to account for the "island" effect of serpentine breadth and the stress/strain concentration at the inner edge of the crest [127]. Therefore for every serpentine shape, the three independent geometrical variables $w/r, l/r$ and α can be converted to $b/s, b/r$ and w/h. A characteristic dimensionless length scale λ can be defined and is assumed to be linearly proportional to $\varepsilon_{max}/\varepsilon_{app}$ through

$$\frac{\varepsilon_{\max}}{\varepsilon_{\text{app}}} = m_1\lambda + m_2. \tag{3.2}$$

Equation (3.2) suggests that the stretchability of the serpentine is completely determined by λ. To obtain m_1 and m_2 we build finite element models for different serpentine shapes, i.e. different combinations of $b/s, b/r$ and w/h, and find the best empirical equation for λ as

$$\lambda = \left(\frac{b}{s}\right)^{0.15} \times \left(\frac{b}{r}\right)^{0.38} \left[\left(\frac{w}{h}\right)^2 - 0.32\frac{w}{h} + 0.42\right], \tag{3.3}$$

and the corresponding linear regression coefficients are obtained as $m_1 = 0.0082$ and $m_2 = 0.0064$. Comparison of experiments, FEM and Equation (3.3) shows good agreement (Figure 3.10 (b)). By using different coefficients m_1 and m_2, our empirical equation is also capable of predicting the stretchability of serpentines made out of other materials such as gold and silicon, as shown in Figure 3.10 (c). The good agreement of the prediction and FEM result proves that the characteristic dimensionless length scale λ given by Equation (3.3) is applicable for different film-substrate material combinations as long as the substrate is stiff enough to suppress any in-plane rotation or out-of-plane twist of the

serpentine.

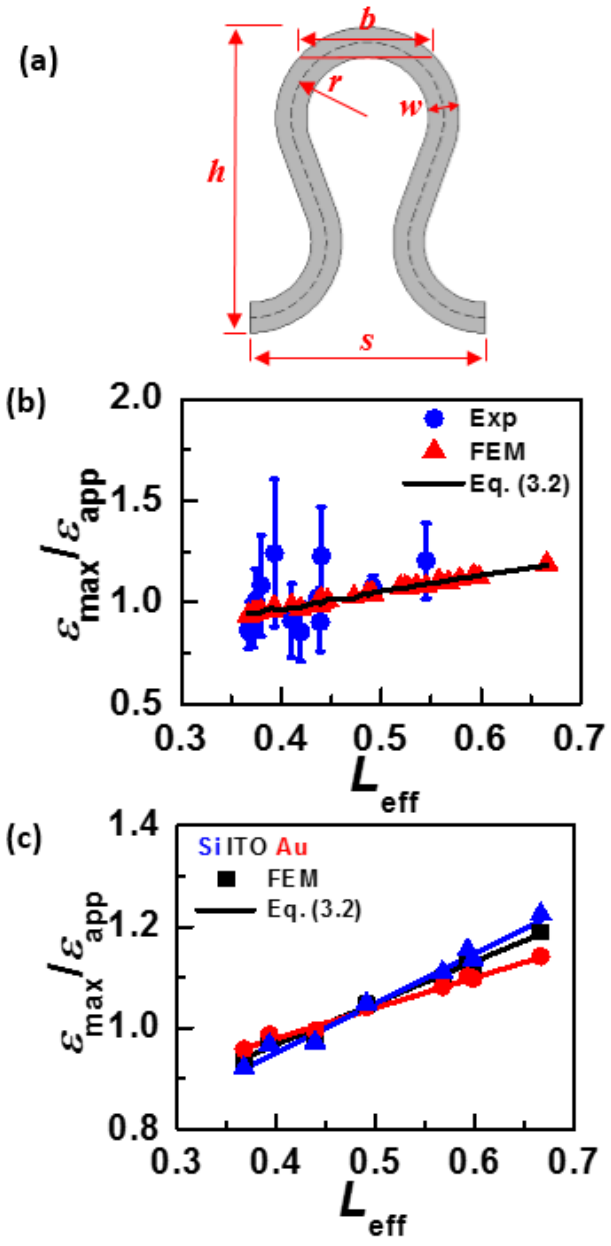

Figure 3.10 (a) New geometric variables that are used to determine the characteristic length λ. (b) A linear empirical relation between strain and λ is validated by FEM and experiments. (c) Linear relation between strain and λ for other serpentine materials such as gold and silicon bonded to Kapton.

3.4.2 Serpentine on Compliant Substrate

The effects of serpentine geometry and serpentine-substrate adhesion have been carefully investigated for Tegaderm-supported ITO serpentine thin film. We conducted *in situ* observation of the failure behavior of weakly-bonded serpentines along with the electromechanical test and the result is shown in Figure 3.11. Due to low interfacial adhesion, narrow serpentines tend to debond before rupture which exhibit high stretchability, as shown as the black curve in Figure 3.11 (a) and all the curves in Figure 3.11 (c) and (e). Wide serpentines tend to rupture before debonding due to the high strain concentration near the crest of the arc according to numerous finite element modeling results (FEM). If we assume delaminated serpentines becomes freestanding and eventually rupture when they are fully straightened, then their ultimate stretchability is limited by the total curve length of the serpentine, i.e.

$$\varepsilon_{\text{app}}^{\text{cr}} = \frac{\pi + 2\alpha + \frac{l}{r} - \left(2\cos(\alpha) - \frac{l}{r}sin(\alpha)\right)}{2\cos(\alpha) - \frac{l}{r}sin(\alpha)} \tag{3.4}$$

which is plotted as the red dashed lines in Figure 3.11 (b), (d) &(f). It is evident that the narrow serpentines better approach the predicted stretchability due to their debonding from the substrate. For wide serpentines such as the ones with $w/r = 0.4$ or $w/r = 0.6$, however, the local strain exceeds material's critical strain before the interfacial adhesion loss its strength, which results in rupture before debonding and thus low stretchability. The failure behavior of the weakly-bonded serpentines can be well evidenced from the optical snap shot. If we differentiate the strain-to-rupture before delamination and after delamination to be bonded and debonded strain-to-rupture, it can be concluded that for narrow serpentines, strain-to-debond is smaller than bonded strain-to-rupture but wide ribbons exhibit smaller bonded strain-to-rupture than strain-to-debond .

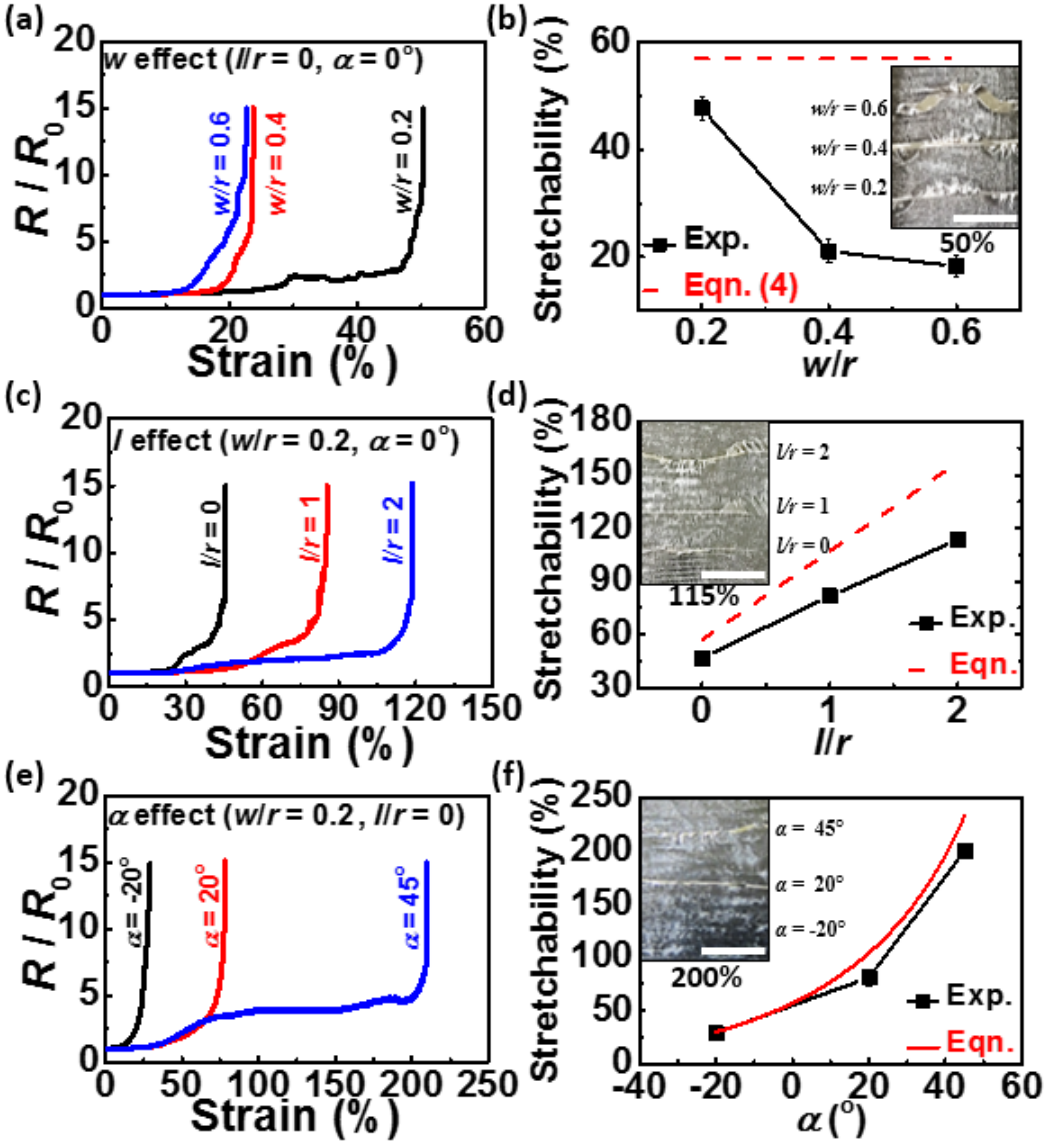

Figure 3.11 Resistance vs. strain plots and stretchability plots for weakly-bonded serpentines. (a)&(b) Serpentines with different ribbon widths (w effect). (c)&(d) Serpentines with different arm lengths (l effect). (e)&(f) Serpentines with different arc angles (α effect). The scale bar is 2 mm in all insets.

Figure 3.12 demonstrates the stretchability of well-bonded ITO serpentine on Tegaderm. Figure 3.12 (a), (c) &(e) suggest that the overall the stretchabilities for these samples are lower compared with weakly-bonded ones because of retarded detachment from substrate, however it does not mean that delamination is fully prohibited. Figure 3.12 (b), (d), (f) provide a direct comparison of the stretchability of weakly-bonded (red dash line) and well-bonded (solid black line) samples. While Figure 3.12 (b) suggests there is no significant change of failure mechanism for a serpentine with $l/r = 0, \alpha = 0°$ due to the close alignment of the two data sets, Figure 3.12 (d) &(f) indicate clear deviations for serpentines with large l/r and α. This is because compliant substrates develop contraction in the transvers direction due to Poisson's effect [54, 128-131], which induces buckling of a thin film that is well-bonded on the top of it (inset in Figure 3.12 (d) &(f)). While carefully controlled buckling has been harnessed to achieve stretchable electronics [54], buckled brittle thin films are susceptible to fracture due to the local tensile strain at the buckled peaks or ridges [131, 132]. For serpentines with long arms or large arc angles the transverse buckling will be more easily triggered, which leads to low stretchability for such structures. Figure 3.12 (c)-(f) suggest the stretchability of well-bonded serpentines is not always monotonic. While simply increasing the arm length or arc angle can enhance the stretchability of weakly-bonded serpentines, it is no longer true for well-bonded serpentines for two reasons. First, when the arm is too long, transverse buckle-delamination within the arms can induce rupture of ITO and the longer the arm, the earlier the rupture. The optimum arm length was found to be $l/r = 1$. Second, when α is too large, strain-to-rupture is reached before strain-to-debond is reached. The optimum arc angle is found to be $\alpha=20°$.

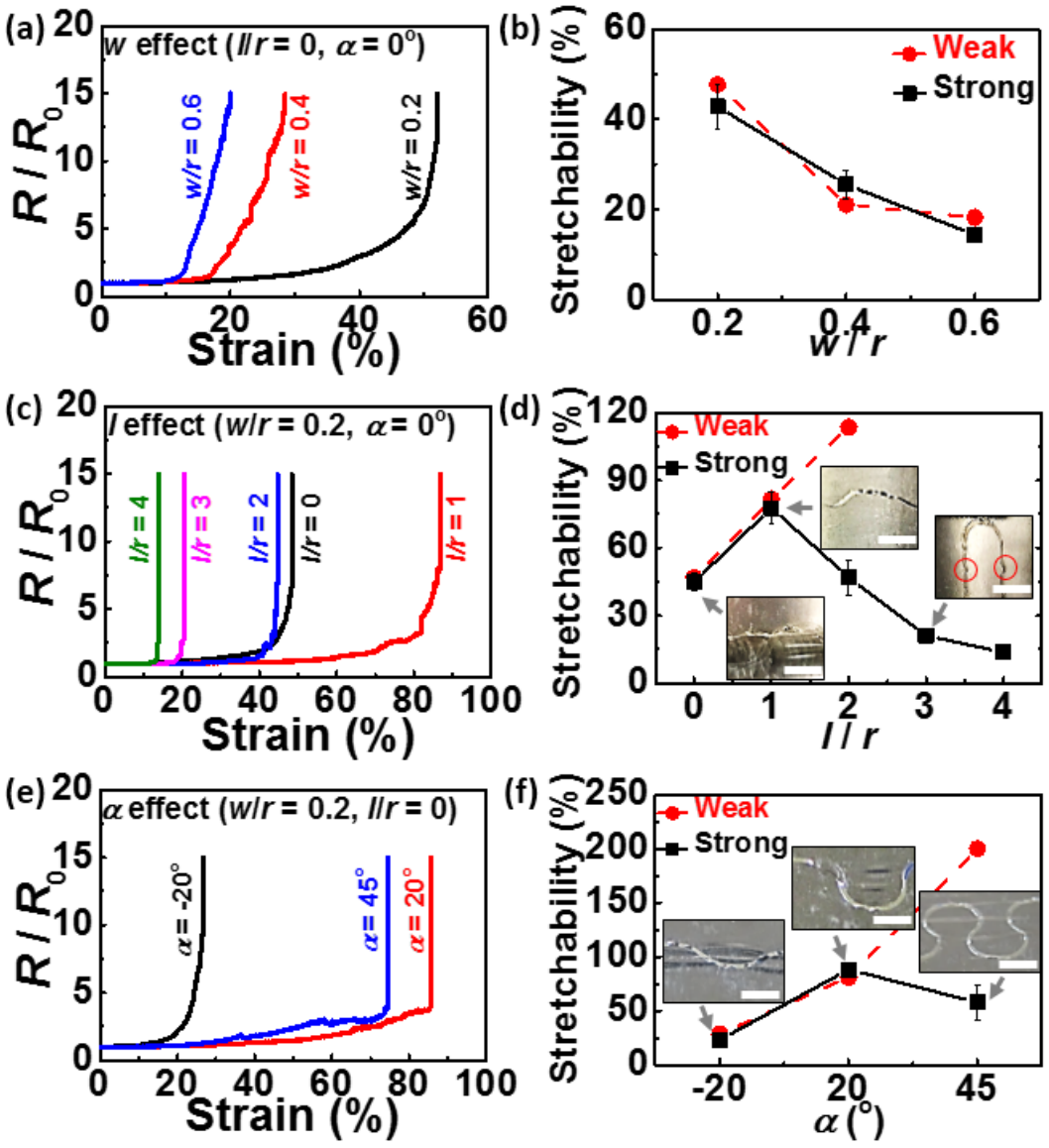

Figure 3.12 Resistance vs. strain plots and stretchability plots for well-bonded serpentines. (a)&(b) Serpentines with different ribbon widths (*w* effect). (c)&(d) Serpentines with different arm lengths (*l* effect). (e)&(f) Serpentines with different arc angles (α effect). The scale bar is 2 mm in all insets.

3.5 CHAPTER SUMMARY

In this chapter, we have studied the stretchability of stiff and compliant polymer-supported ITO serpentine thin films. It is found that when the substrate is stiff, the in-plane rotation and out-of-plane buckling of the serpentine is completely suppressed, which leads to low stretchability and very limited effects of the serpentine geometry. When the substrate is compliant, the serpentine has some degree of freedom to rotate and buckle, which is also affected by the serpentine-substrate interfacial adhesion. To demonstrate the stretchability experimentally, an innovative bench-top manufacturing method has been developed to fabricate ITO serpentine thin films on compliant polymers, and we were able to stretch ITO serpentines by more than 100%. In the next chapter we will extend this new fabrication method to manufacture stretchable devices.

Chapter 4 Cut-and-Paste Fabrication[1,2]

The conventional cleanroom-based micro-fabrication method is not suitable for rapid prototyping or mass production of disposable medical patches such as epidermal electronics. We therefore invent a dry, benchtop, freeform and portable manufacturing method called the "cut-and-paste" method to manufacture disposable epidermal sensor systems in a time and cost effective manner. Manufacturing quality has been carefully investigated and pros and cons are explicitly discussed.

---

[1] S. Yang, Y.-C. Chen, L. Nicolini, P. Pasupathy, J. Sacks, B. Su, R. Yang, D. Sanchez, Y.-F. Chang, P. Wang, D. Schnyer, D. Neikirk, N. Lu*, "*"Cut-and-Paste" Manufacture of Multiparametric Epidermal Sensor Systems*," Advanced Materials, vol. 27, no. 41, pp. 6423-6430, Nov 4, 2015.
Author contributions: S. Y., Y.-C. C., L. N., P. P., B. S., R. Y., N. L., D. N., and D. S. conducted device design, fabrication, calibration, and testing. S. Y. led the FEM analysis with J. S. and D. S.'s assistance. Y. C., P. W., S. Y., Y.-C. C., L. N. and R. Y. served as human subjects. L. N. and D. N. performed EP analysis. N. L., D. N., and D. S. supervised and coordinated the project. N. L., S. Y., Y.-C. C., L. N., P. P., D. N., and D. S. wrote the paper.

[2] S. Yang, E. Ng, N. Lu*, "*Indium Tin Oxide (ITO) serpentine ribbons on soft substrates stretched beyond 100%*," Extreme Mechanics Letters, vol. 2, pp. 37-45, Jan, 2015, 2015.
Author contributions: S. Y. conducted device design and FEM analysis. S. Y. and E. N. performed fabrication and testing. N. L. supervised and coordinated the project. N. L. and S. Y. wrote the paper.

4.1 OBJECTIVE AND OVERVIEW

Conventional manufacturing process of epidermal electronics relies on standard microelectronics fabrication processes. It involves vacuum deposition of thin films, spin coating, photolithography, wet or dry etching and transfer printing [63, 133-139]. Although it has proven to be effective, there are several limitations associated with such processes. For example, this method depends on cleanroom-based facilities which are not portable, vacuum deposition and photolithography are time consuming, chemicals used in wet etching are hazardous to human body, wafers and masks used are expensive, and the rigid wafer is not compatible with roll-to-roll process. In this chapter, we report an innovative time- and cost-effective, benchtop, freeform, and portable fabrication method, which is applied to manufacture high-quality epidermal sensors. Detailed fabrication process of this new method is discussed and manufacture quality is investigated.

4.2 FABRICATION PROCESS

A schematic of the "cut-and-paste" fabrication process is shown in Figure 4.1, snapshots of detailed experimental steps can be found in our recently published paper [91]. The process starts with laminating a commercially available metal-coated PET foil (Goodfellow, USA) on a flexible, single-sided thermal release tape (TRT, Semiconductor Equipment Corp., USA) with the metal side touching the adhesive of the TRT. The other side of the TRT is then adhered to a tacky flexible cutting mat, as shown in Figure 4.1 (a). The cutting mat is fed into an electronic cutting machine (Silhouette Cameo, USA) with the PET side facing the cutting blade. By importing the AutoCAD design into the Silhouette Studio software, the cutting machine can automatically carve the Au-on-PET sheet with designed seams within minutes (Figure 4.1 (b)). Once seams are formed, the TRT is gently peeled off from the cutting mat (Figure 4.1 (c)). Slightly baking the TRT on a 115 °C hotplate for 1~2 minutes deactivates the adhesives on the TRT so that the excesses

can be easily peeled off by tweezers (Figure 4.1 (d)). The patterned devices are finally printed onto a target substrate with native adhesives, which could be a temporary tattoo paper (Silhouette) or a medical tape, such as 3M Tegaderm^{TM} transparent dressing or 3M kind removal silicone tape (KRST) (Figure 4.1 (e)), yielding an epidermal sensor system. Steps illustrated by Figure 4.1 (a) to Figure 4.1 (e) can be repeated for other thin sheets of metals and polymers, which can be printed on the same target substrate with alignment markers, rendering a multimaterial multifunctional system. For well-trained users, the entire process only takes about 15 minutes from beginning to end, which indicates that this new method has a significant advantage over conventional cleanroom-based fabrication approaches.

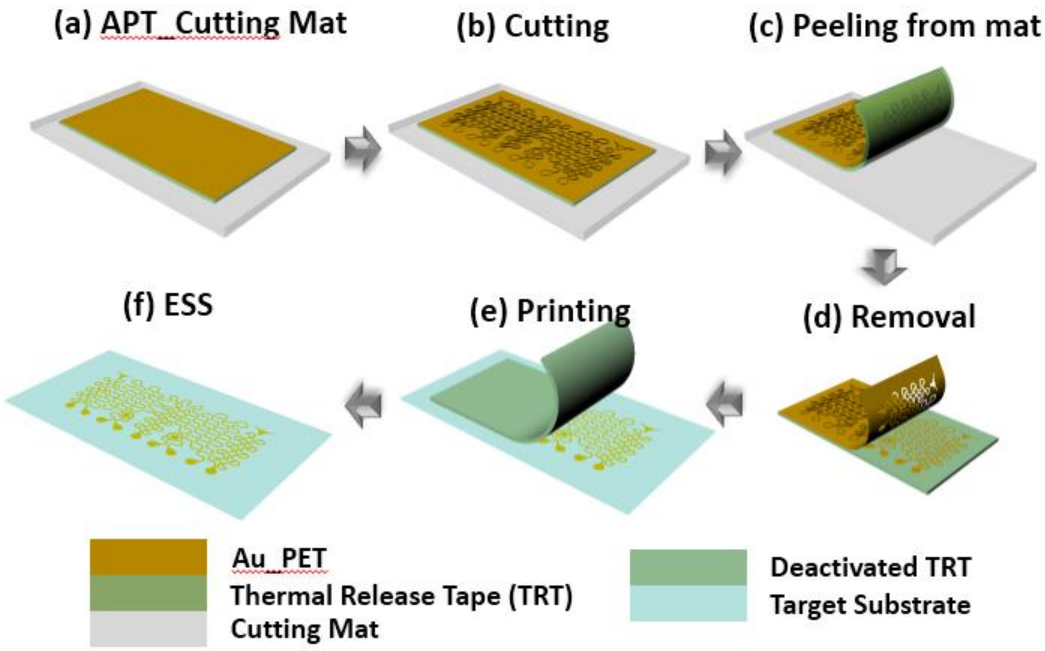

Figure 4.1 Schematics for the "cut-and-paste" process. (a) Au-PET-TRT (APT) laminated on the cutting mat with PET being the topmost layer. (b) Carving designed seams in the Au-PET layer by an automated mechanical cutting machine. (c) Peeling APT off the cutting mat. (d) Removing excessive Au-PET layer after deactivating the TRT on hot plate. (e) Printing patterned Au-PET layer onto target substrate. (f) Resulted epidermal sensor systems (ESS) with Au being the topmost layer.

4.3 MANUFACTURING QUALITY

To develop a better understanding of the performance of this new fabrication method and provide guidelines for future developments, we have carefully performed studies on the resolution, surface profile, width uniformity and blade wear effect of this new fabrication method by examining the rendered ribbon geometry.

4.3.1 Resolution Test

Epidermal sensors are designed to be at least as stretchable and conformable as the human skin in order to survive different kinds of skin deformation while remaining in close contact with human skin for high-fidelity bio-signal monitoring. According to previous studies on the stretchability and conformability [140-143] of stretchable serpentine structures, it is believed that the serpentine has to be minimized in width in order to be highly stretchable and conformable. For our "cut-and-paste" method, the smallest feature width, i.e. the resolution, mainly depends on the cutter's intrinsic mechanical performance. Figure 4.2 shows a representative resolution test. In the test, the same pattern is cut with different ribbon widths, from 600 μm down to 50 μm. The raw material being cut in this test is 9-μm-thick Al on 12-μm-thick PET foil (NEPTAPE® by NEPTCO, Inc.). It is evident that the pattern can be successfully cut when ribbon width is set to 200 μm, even though the uniformity is compromised. When the ribbon width is set to be 100 μm or less, the pattern can no longer be preserved. For our devices we set the ribbon width to be 400 μm in order to achieve high structural integrity and device functionality.

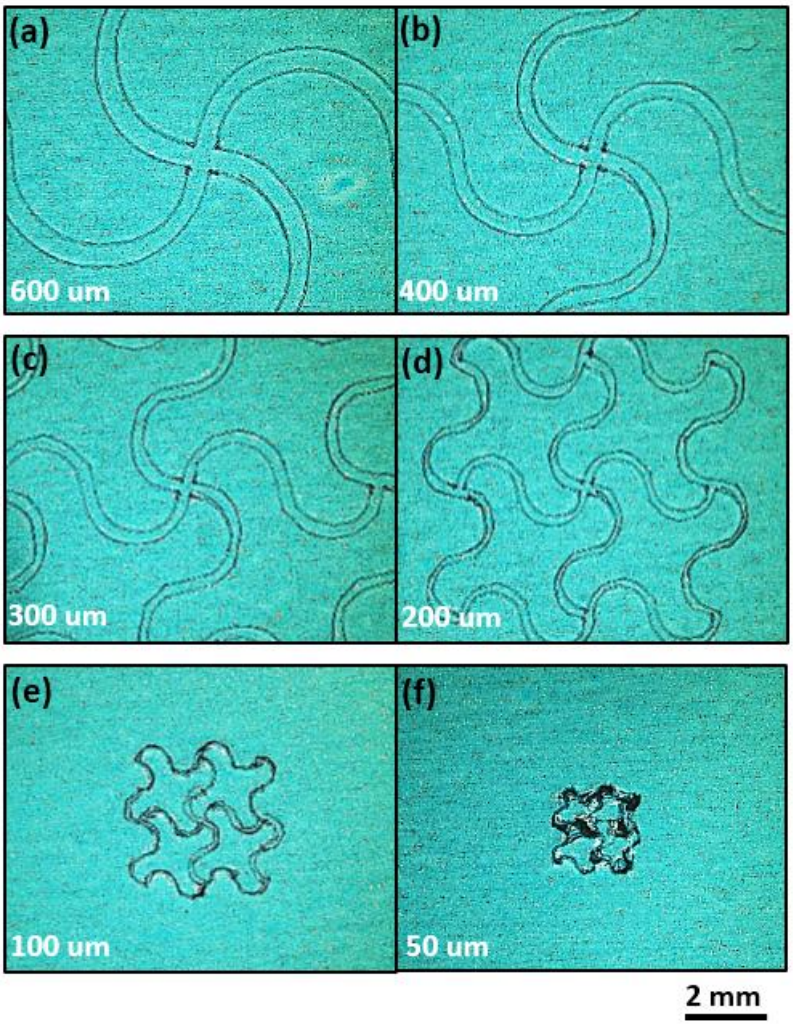

Figure 4.2 Resolution tests of the cutting machine. Pictures of the same seam pattern carved on blue PET-Al foil (Neptco Inc.) with different ribbon width: (a) 600 μm, (b) 400 μm, (c) 300 μm, (d) 200 μm, (e) 100 μm, and (f) 50 μm, by the cutting machine. The resolution of the cutting machine is determined to be 200 μm.

4.3.2 Width Uniformity

Ideally the resulting ribbon width should be the same as the setting in computer, however, due to the mechanical tolerance of the cutter, the width of the carved pattern exhibits variation. Ribbon width uniformity is examined by measuring and summarizing the widths of many cross-width lines which are evenly spaced along the median line of the serpentine, as shown in Figure 4.3 (a). We used 25-μm-thick Kapton sheet (Dupont) for this study. The cutter was set to cut 400-μm-wide ribbons but Figure 4.3 (b) indicates that ribbon width distribution was centered on 340 μm, with a standard deviation of 87 μm.

4.3.3 Thickness Profile

Thickness profile of the cut ribbon has been examined by profilometer (Dektak 6M stylus profilometer, vender, USA) at three different locations on one ribbon, (Figure 4.3 (c)). Cross-sectional profile in Figure 4.3 (d) indicates that the thicknesses of the cut ribbon exhibit good consistency in different locations and are close to the thickness of the raw material, which is 25 μm.

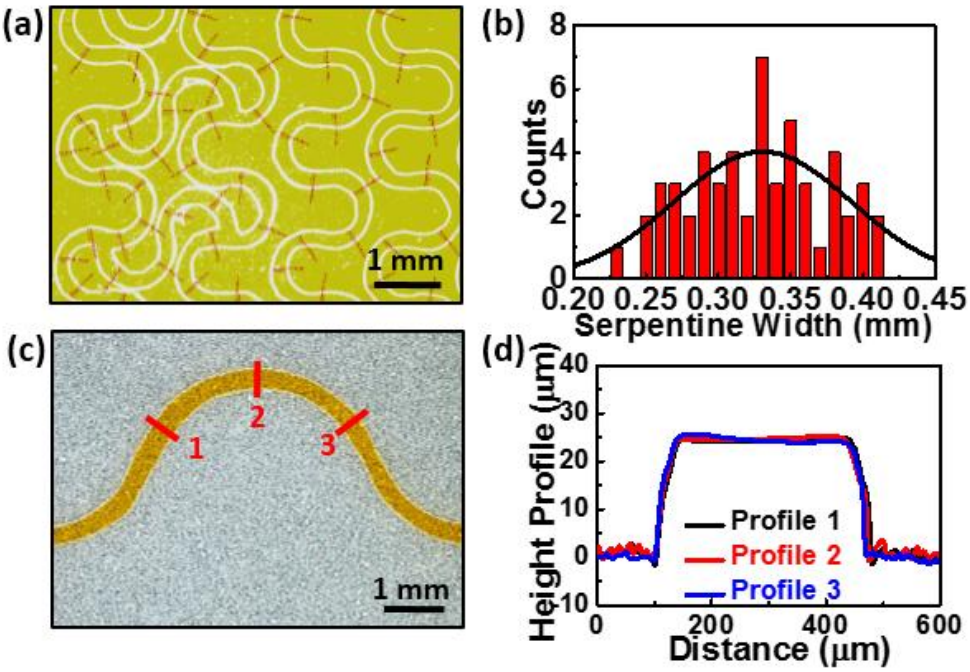

Figure 4.3 Width uniformity and surface profile of the cut ribbons. (a) Image of sampling spots for width uniformity investigation after cutting a 25 μm thick Kapton sheet on TRT. Ribbon width is 400 mm by drawing. (b) Width distribution fitted by Gaussian distribution (black curve) with a mean of 340 μm and a standard deviation of 87 μm. (c) Image of sampling spots for height profile investigation of the cut Kapton ribbon after excessive parts removed. (d) Height profile of the Katpon ribbon, showing flat plateau and steep transition zone.

4.3.4 Effect of Blade Tip Sharpness and Settings

Cutting quality is found to be highly dependent on the sharpness of the cutting blade. The mechanical blade tip can be worn or destroyed and lose its sharpness, depending on the cutting time, raw material, parameter setting and even mishandling of the cutter. Therefore it is important to optically check the blade condition before running any cutting job. Cutting jobs with different cutting parameters (see figure caption of Figure 4.4) have been performed with the results displayed in Figure 4.4 (d)-(i). It is concluded that the cutting thickness setting, thickness of the foil to be cut, and the blade condition are the most important factors for cutting quality control. After the parametric study we came up with a set cutting parameters, sharpness=5, cutting rate=2, thickness=1, that gives the best quality for our device. The close-up of representative spots of our samples is shown in Figure 4.4 (j)-(l).

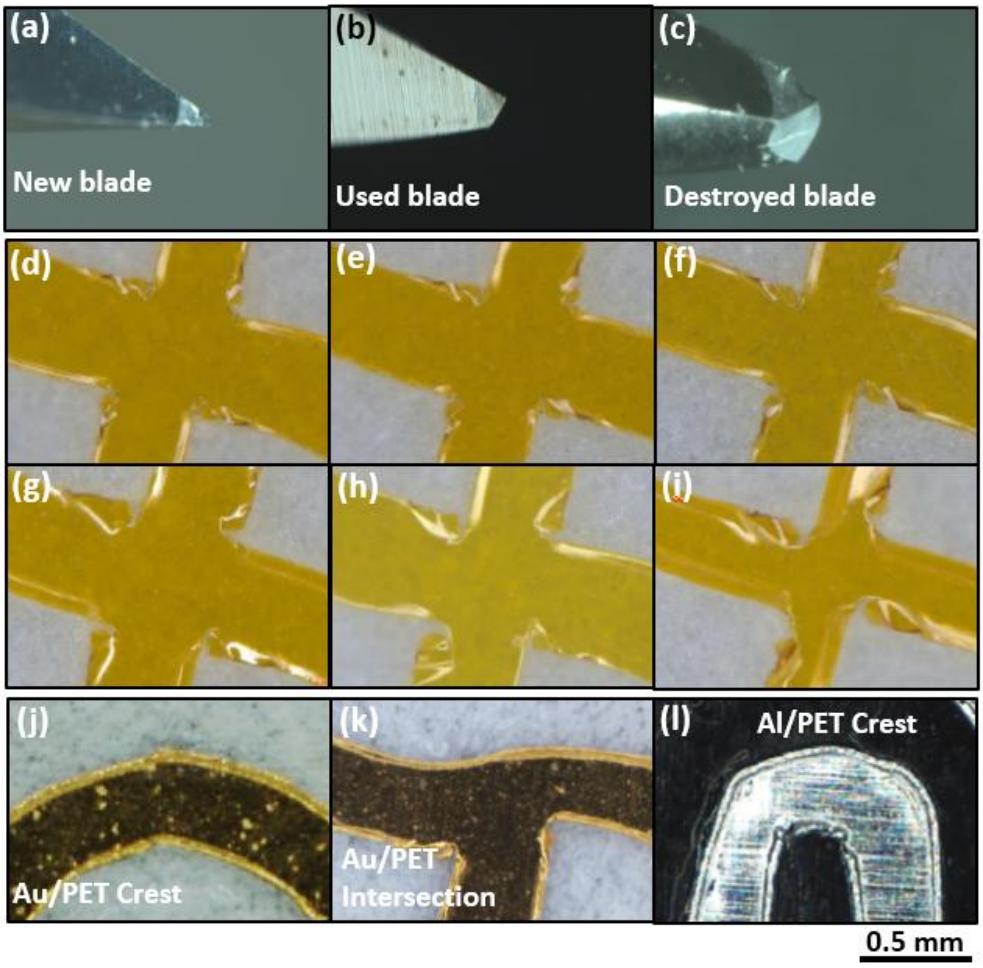

Figure 4.4 Effects of blade tip sharpness and cutting parameters. Images of a (a) new blade (b) a used blade and (c) a destroyed blade. Cutting results for different parameter combinations where KT stands for Kapton thickness, Sh for sharpness, Ra for cutting rate, Th for thickness, NB for new blade, UB for used blade: (d) KT=25.4mm, Sh=5, Ra=1, Th=7, NB (e) KT=25.4mm, Sh=10, Ra=1, Th=7, NB (f) KT=25.4mm, Sh=5, Ra=10, Th=7, NB (g) KT=25.4mm, Sh=5, Ra=1, Th=20 NB (h) KT=12.7mm, Sh=5, Ra=1, Th=7, NB (i) KT=25.4mm, Sh=10, Ra=1, Th=7, UB. Zoomed in images of final ESS cut by optimized parameters: (j) crest of the Au RTD, (k) intersection of the Au EP sensor, (l) crest of the stretchable Al coil.

4.4 CHAPTER SUMMARY

In this chapter, we have introduced a freeform "cut-and-paste" method to produce stretchable devices in a time and cost effective fashion. The fabrication process was described in detail and manufacturing quality has also been studied. Although the resolution of the "cut-and-paste" method is not as good as photolithography-based methods, the fabrication area can be significantly lager and the fabrication time is greatly reduced. To demonstrate the "cut-and-paste" method, a multifunctional epidermal sensor system (ESS) will be introduced in the next chapter.

Chapter 5 Multifunctional Epidermal Sensor System (ESS)[1]

Our body is radiating data about ourselves continuously. It is important to collect and analyze biological data for fitness tracking, health monitoring and disease prevention. Using our "cut-and-paste" fabrication method, we have successfully manufactured a multimaterial, multiparametric epidermal sensor system (ESS) which can be noninvasively laminated on human skin to continuously monitor electrocardiogram (ECG), electromyogram (EMG), electroencephalogram (EEG), skin temperature, skin hydration and the respiratory rate of the human body.

[1] S. Yang, Y.-C. Chen, L. Nicolini, P. Pasupathy, J. Sacks, B. Su, R. Yang, D. Sanchez, Y.-F. Chang, P. Wang, D. Schnyer, D. Neikirk, N. Lu*, "*"Cut-and-Paste" Manufacture of Multiparametric Epidermal Sensor Systems*," Advanced Materials, vol. 27, no. 41, pp. 6423-6430, Nov 4, 2015.
Author contributions: S. Y., Y.-C. C., L. N., P. P., B. S., R. Y., N. L., D. N., and D. S. conducted device design, fabrication, calibration, and testing. S. Y. led the FEM analysis with J. S. and D. S.'s assistance. Y. C., P. W., S. Y., Y.-C. C., L. N. and R. Y. served as human subjects. L. N. and D. N. performed EP analysis. N. L., D. N., and D. S. supervised and coordinated the project. N. L., S. Y., Y.-C. C., L. N., P. P., D. N., and D. S. wrote the paper.

5.1 OBJECTIVE AND OVERVIEW

Many health conditions of the human body can be reflected by non-invasive measurements of surface biosignals, such as surface ECG, surface EMG, surface EEG, skin temperature, skin hydration and respiratory rate [141]. One of the main focuses in measuring surface biosignals is to capture high fidelity and low noise data in real time. Conventional measurement exploits rigid electrodes that are attached to human skin through wet gels, which may cause skin irritation or may dry out after long-term wearing. Emerging epidermal electronics exhibit low stiffness and high stretchability that are well matched with human skin. They are demonstrated to be compelling alternatives to conventional surface sensors. In Chapter 4, we developed a low-cost, bench-top "cut-and-paste" method for manufacturing stretchable devices. As a demonstration, this chapter will introduce a multimaterial, multifunctional epidermal sensor systems (ESS), manufactured by this method. We will use this ESS to measure surface ECG, surface EMG, surface EEG, skin temperature, skin hydration and respiratory rate.

5.2 LAYOUT OF THE EPIDERMAL SENSOR SYSTEM

The top view of a multimaterial, multiparametric ESS supported by transparent temporary tattoo paper and its white liner is shown in Figure 5.1, which includes three Au-based filamentary serpentine (FS) EP electrodes which can be used for measurement of ECG, EMG and EEG, one Au-based FS resistance temperature detector (RTD), two Au-based dot-ring impedance sensors (for hydration measurement), and an Al/PET-based planar stretchable coil. In this picture, all Au-based sensors have the Au side facing up The stretchable coil, however, has the blue colored PET facing up because PET has demonstrated good biocompatibility [144-147] but some people's skin can be allergic to Al. For the three EP electrodes, the inter-electrode distance is set to be 2 cm for effective EP signal recording [141]. The FS is designed with a 1/5 ribbon width to arc radius ratio

in order to balance the trade-off between stretchability and occupied area, according to our recent mechanics of serpentine research [37]. The same FS design is not applicable to the stretchable Al coil because it will consume too much space when more turns are needed for higher inductance. Therefore a double-stranded serpentine design is proposed for the Al-PET coil, as shown in Figure 5.1, which saves space without compromising the number of turns or the stretchability. The two longhorns at the upper left and right corners of the Au pattern serve as alignment markers for printing Au and Al devices on the same tape. The overall size of this device is 7.5 cm × 5 cm, which ensures that this multifunctional epidermal sensor system can fit well in the majority of parts of the human body, including the chest, forehead, forearms and waist. The sensors are designed in such a way that they exhibit high electrical sensitivity to biosignals as well as mechanical robustness to skin deformations.

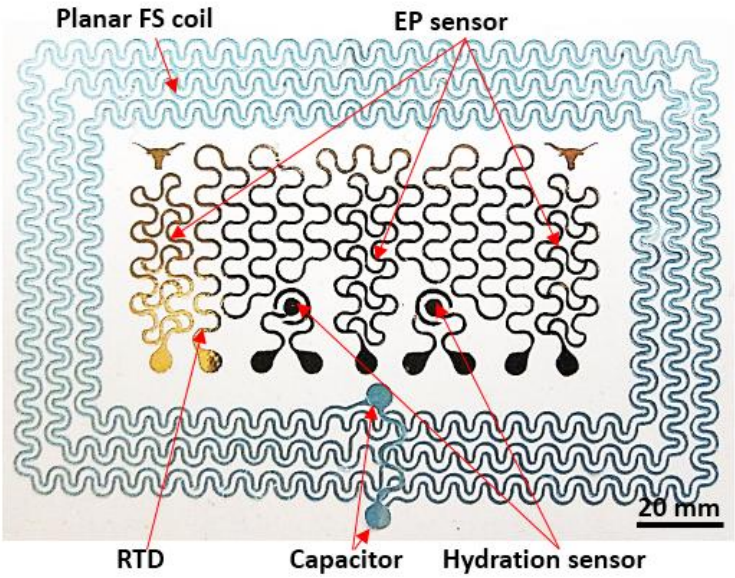

Figure 5.1 Top view of an ESS which incorporates three electrophysiological (EP) electrodes (Au-PET), a resistance temperature detector (RTD) (Au-PET), two coaxial dot-ring impedance sensors (Au-PET), and a wireless planar stretchable strain sensing coil (Al-PET), all in filamentary serpentine (FS) layout.

5.3 ELECTROPHYSIOLOGICAL SENSOR

Electrophysiological (EP) signals on the surface of human skin measure the flow of ions in the underlying tissues and organs, which reflects their health and function. For example, noninvasive ambulatory monitoring of ECG on human chest can help detect multiple important features of heart malfunction like irregular heartbeat (arrhythmia) [148]. EMG reflects human muscle activity and can identify neuromuscular diseases and serve as a control signal for prosthetic devices or other machines [141]. EEG measured from the surface of the human scalp can be used to not only capture cognitive and memory performance [149], but also chart brain disorders like epilepsy [150] and stroke [151].

Figure 5.2 (a)&(b) show ECG measured from human chest using silver/silver chloride (Ag/AgCl) gel electrodes and the ESS without applying any conductive gels. Both ESS and Ag/AgCl electrodes are connected to a small portable amplifier (AvatarEEG^{TM}) with a shared ground port. Out of the three EP electrodes integrated on the ESS, as shown in Figure 5.1, the center one is utilized as a ground and the other two electrodes measure EP signals in a bipolar montage to reflect the difference in electrical potential. Signals recorded by this amplifier are processed using a Principle Component Analysis based algorithm [152] with the final results shown in Figure 5.2 (b). It is evident that the important features of ECG are captured by both electrodes, but the ECG measured by our ESS demonstrates higher amplitude and more details compared with the Ag/AgCl electrodes. Specifically, the average amplitude of the P waves in the ECG measured by our ESS is around 1.9 times of that measured by the Ag/AgCl electrodes.

Except for EEG, the same type of ESS has also been placed on the forearm, specifically over the flexor muscles, to measure the EMG during two hand clenches (Figure 5.2 (c)&(d)). The intensity of the gripping force can be measured by a commercial dynamometer (Exacta™) and it is clear that the higher gripping force corresponds to higher

signal amplitude in the measured EMG. Specifically, the average amplitude of the signal envelope corresponding to 44 N gripping force is about 3 times of that for a gripping force of 14 N.

Finally the EEG has been measured by placing Ag/AgCl electrodes and the ESS on human forehead. Both electrodes are referenced against one FS electrode placed behind the human ear on the mastoid location, as shown in Figure 5.2 (e). Signals are high and low passed filtered at 0.1Hz and 40 Hz respectively and frequency spectrums are calculated using standard fast Fourier transformations (FFT). The EEG measurements between conventional and ESS agree remarkably well and their FFT spectrums almost fully overlap in the upper right panel of Figure 5.2 (f), which confirms that conventional and ESS electrodes are almost indistinguishable in measured EEG signals, but the ESS offers additional merits including conformability, compliance and customizable electrode patterns. The lower right panel of Figure 5.2 (f) compares the FFT of the ESS measured EEG signal while the participant maintained eyes open and eyes closed. One can note the expected increase in relative alpha power associated with the eyes closed period relative to eyes open (centered around 10 Hz). Figure 5.2 (f) shows the maximum amplitude of the relative alpha power increased by 1.75 times from eyes open period to eyes close period.

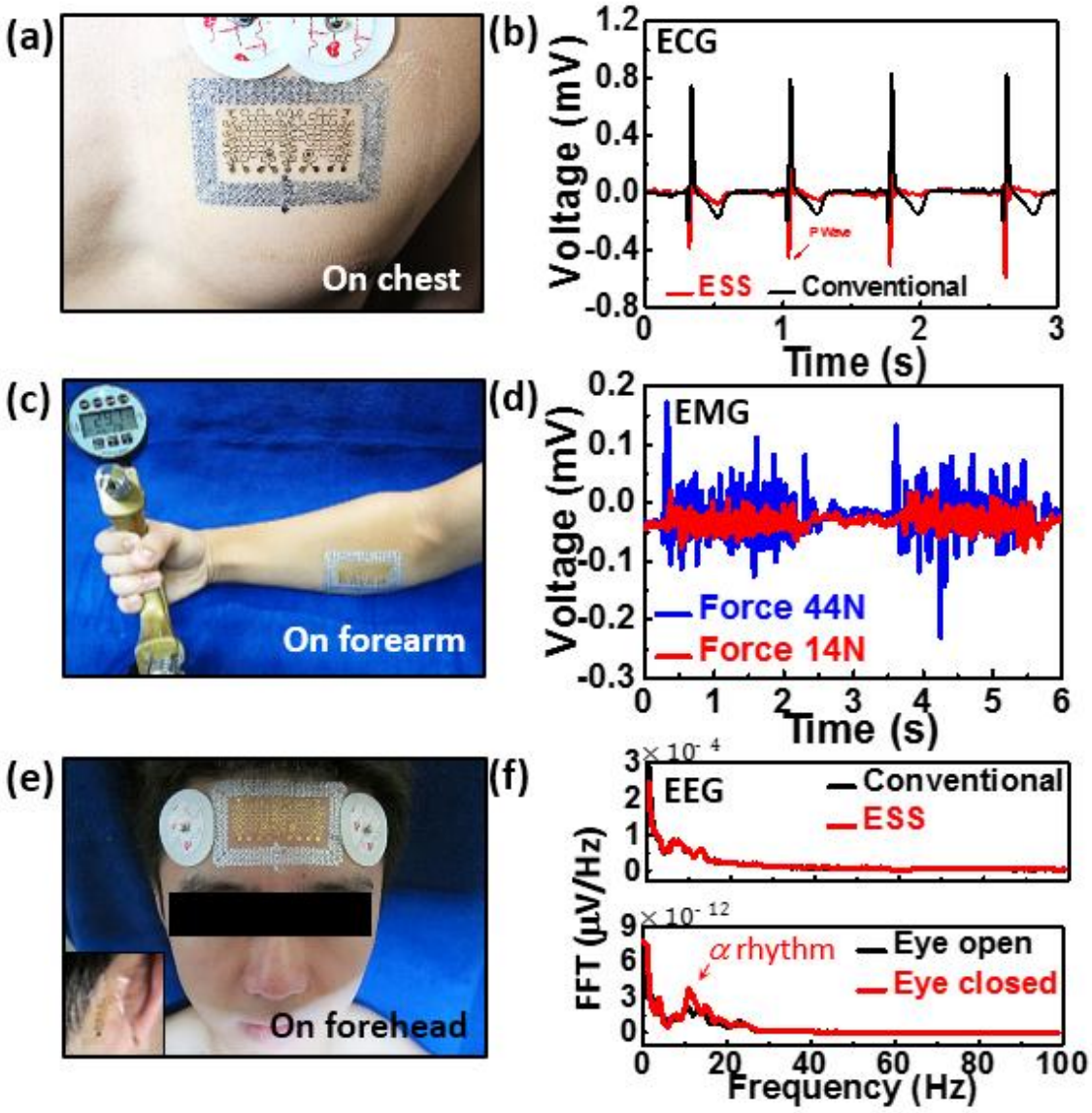

Figure 5.2 ECG, EMG and EEG measurements by ESS. (a) ESS placed on human chest along with conventional Ag/AgCl electrodes to measure ECG. (b) ECG simultaneously measured by ESS (red) and Ag/AgCl electrodes (black). Stronger ECG signals are obtained by the ESS. (c) ESS attached on human forearm for EMG measurement when the subject is gripping a commercial dynamometer with different forces. (d) EMG result from ESS in which Higher amplitude corresponds to higher gripping force. (e) EEG measured on human

forehead by both ESS and Ag/AgCl electrodes. (f) Two frequency spectrum of the EEG are well overlapped. 10 Hz alpha rhythm measured by ESS is clearly visible when eyes are closed.

5.4 RESISTANCE TEMPERATURE DETECTOR

In addition to EP signals, skin temperature is also an important indicator of human health. In our EES, the ultrathin, stretchable RTD can be built as a narrow but long ribbon of Au FS as labeled in Figure 5.1, which has a high initial resistance R_0 and a predictable change in resistance as the temperature changes. In order to eliminate the deformation effect on the final resistance reading, strain induced resistance is evaluated and the result is plotted in Figure 5.3 (a). It shows the resistance reading for RTD is stable for 25% applied strain, which is around the maximum strain that human skin can suffer without permanent damage. This means the temperature change due to strain is negligible. RTD resistance and temperature changes are related through the following equation

$$\frac{\Delta R}{R_0} = \alpha(T - T_0) \tag{5.1}$$

Based on our experimental result (Figure 5.3 (b)) the temperature coefficient of resistance is found to be α = 0.0017 $^{\circ}C^{-1}$. To perform skin temperature measurement, the epidermal RTD was attached on a human forearm, along with a commercial thermocouple (TMD-56, Amprobe) as pictured in Figure 5.3 (c). Skin temperature measured by the epidermal RTD and the thermocouple are plotted in Figure 5.3 (d). The experiment shows that skin temperature is initially stabilized at around 30 °C. At t = 2'13", an ice bag is brought in contact with the RTD and skin for 1 minute and then removed. The corresponding temperature drop and recovery are clearly visible in Figure 5.3 (d). The strong correlation between RTD and thermocouple outputs has validated the use of RTD as a compliant and stretchable skin temperature detector.

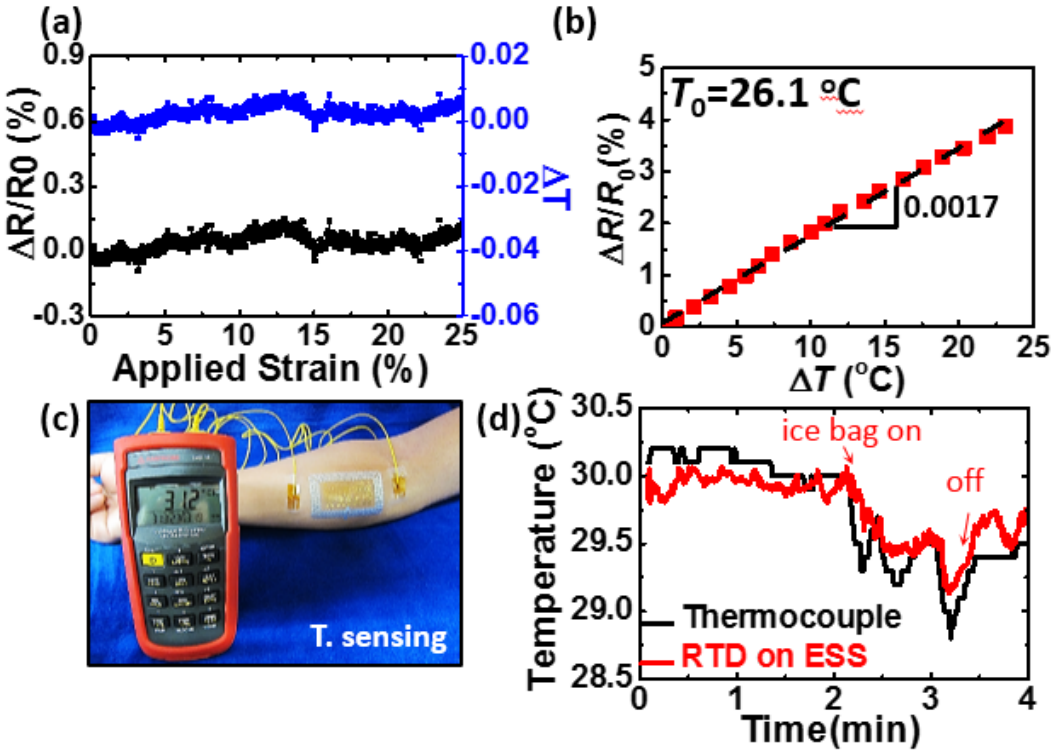

Figure 5.3 (a) The resistance reading for RTD is stable for 25% applied strain, which results in negligible temperature change. (b) Calibration curve of RTD. The measured temperature coefficient of resistance is 0.0017. (c) Picture of RTD placed on the forearm along with traditional thermalcouple for temperature monitoring. (d) Skin temperature changes measured by both epidermal RTD and thermocouple found good correlation.

5.5 EPIDERMAL HYDRATION SENSOR

Skin hydration is widely used in dermatology and cosmetology for the detection of diseases (e.g., atopic dermatitis, etc.) [153-157], the assessment of mental stress or hormone levels [158, 159], and the evaluation of medical therapies or cosmetic treatments [160, 161]. Skin hydration level is reflected by the impedance of skin, which can be conveniently measured by impedance sensors in the coaxial dot-ring design as labeled Figure 5.1. Laminating the epidermal hydration sensor (H. sensor) on human skin, an inductance, capacitance, and resistance (LCR) meter (Digital Multimeter, Rigol) was used to measure the impedance at different frequencies as well as different skin hydration levels. A commercial corneometer (MoistureMeterSC Compact, Delfin Inc.) was used to quantify the skin hydration level. Calibration for the skin hydration sensor was conducted and plotted in Figure 5.4 (a)&(b), in which the same data set for impedance magnitude is plotted as function of sweeping frequency and hydration level in Figure 5.4 (a)&(b), respectively. Figure 5.4 (c)&(d) illustrate a continuous hydration measurement with both epidermal H. sensor and the corneometer before and after the subject drank a can of cold Espresso. The caffeine in Espresso is expected to lead to perspiration as it stimulates human central nervous system, which activates the sweat glands. The results are shown in Figure 5.4 (d), which clearly indicates gradual increase of hydration after drinking Espresso based on the measurements of both the epidermal H. sensor and the corneometer. It is interesting to note that skin hydration peaks seven minutes after drinking the Espresso and starts to decay after that, likely due to the thermoregulation of the body. The tests also suggest that laminating ESS on dry skin may induce slight sweating, which induces lower impedance readings. It is also important to notice that the contact pressure significantly affects the measurement of skin impedance, as shown in Figure 5.4 (e)&(f), and mishandling of the measuring process such as loose contact of the ESS to the skin can largely fail a measurement.

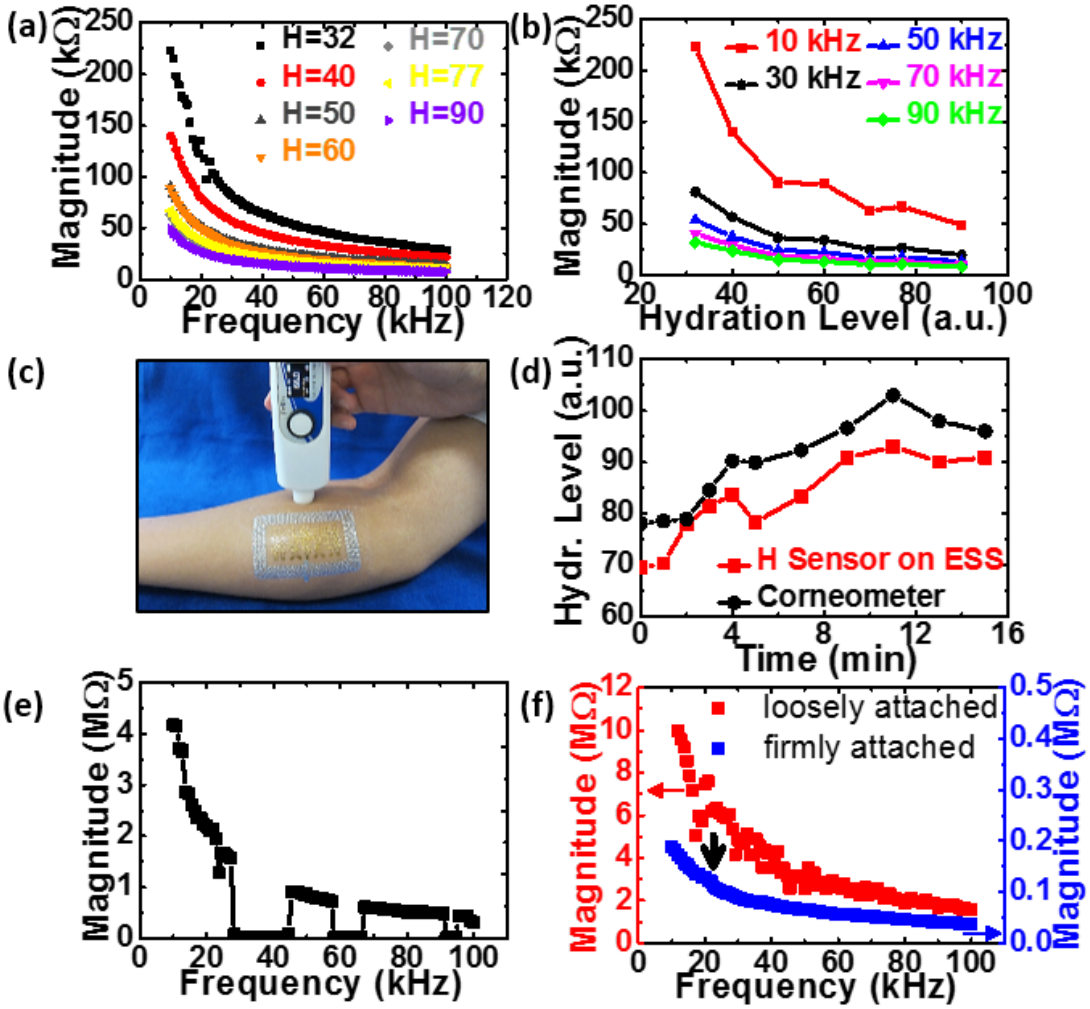

Figure 5.4 Calibration curves for hydration sensor measured on human skin. The magnitude of impedance is plotted as a function of (a) sweeping frequency and (b) hydration level. (c) Picture of ESS placed on the forearm along with commercial coaxial corneometer for hydration monitoring. (d) Real time skin hydration before and after Espresso intake measured by both commercial coaxial corneometer and ESS. (e) Magnitude change of impedance responding to repeated firm pressure applied on ESS which is gently attached on skin. (f) Magnitude of impedance without (red) and with (blue) one time hard press immediately after ESS is applied on skin. After one time hard press, magnitude drops orders of magnitude and pressure effect is eliminated.

5.6 RESPIRATORY SENSOR

The respiration rate is the number of breaths a person takes per minute and normal respiration rates for an adult person at rest range from 12 to 16 breaths per minute. Irregular respiration rates are closely related to fever, illness, and with other medical conditions, such that it is an important vital signs to be carefully monitored. In our ESS, an epidermal respiratory rate sensor was built using electrically conductive rubber (ECR), which is similar to our previous compliant strain gauge work [162], but was made by the more cost and time effective "cut-and-paste" method. Three types of ECR strain gauges were fabricated as shown in Figure 5.5 (a). The vertical and horizontal ECR strips are used to measure the vertical and horizontal tensile strains by measuring their change in resistance. The gauge factor (GF) is calculated from the calibration curve shown in Figure 5.5 (b) by using equation

$$GF = \frac{\Delta R/R_0}{\varepsilon} \tag{5.2}$$

The temperature induced resistance change can be compensated for in a square-shaped Wheatstone bridge as shown in Figure 5.5 (a) and the sensitivity of output voltage to applied uniaxial strain is given in Figure 5.5 (c). FEM results of strain distributions in the ECR resistors are offered in Figure 5.5 (d) when a horizontal tensile strain of 5% is applied on the Tegaderm substrate.

The test on skin was performed by applying Tegaderm-supported ECR-based strain gauges on the chest of a human subject and various respirational patterns have been studied. Figure 5.5 (e) illustrates the deformation of human chest during normal breath and deep breath using the Wheatstone bridge. Larger amplitude and lower frequency are observed for deep breath. Figure 5.5 (f) shows chest skin deformation due to a cough as measured by the Wheatstone bridge and cough induced voltage output pattern is characterized by undulated plateau.

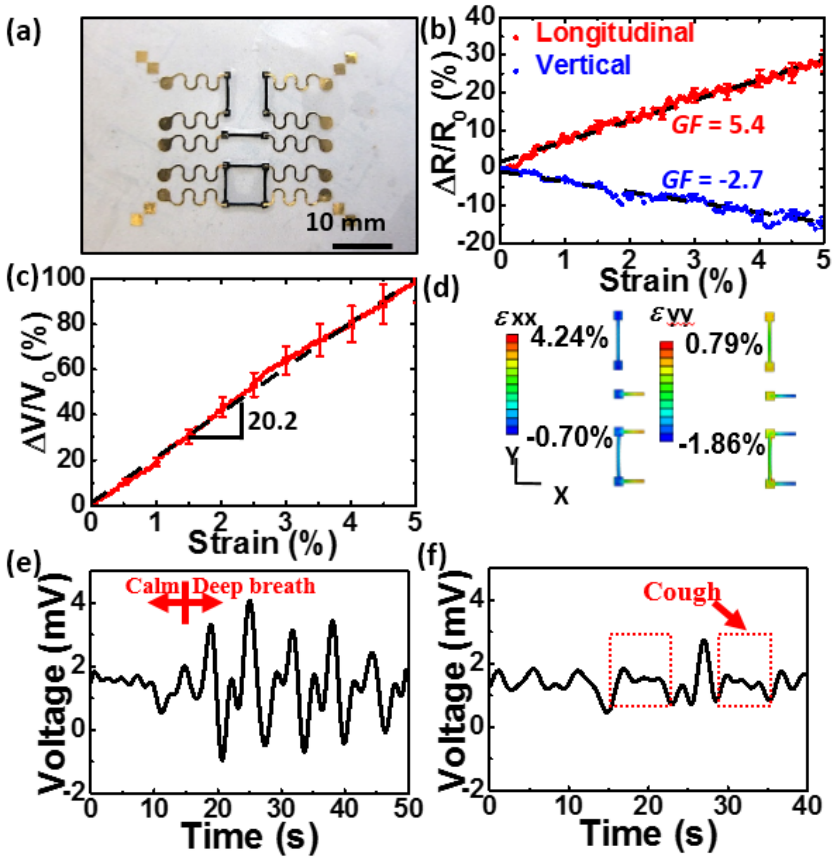

Figure 5.5 Stretchable strain gauges made by electrically conductive rubber (ECR) on ESS for respiratory rate and pattern monitoring. (a) Picture of the ESS strain gauge where ECR (black) is the strain sensing component and Au serpentine ribbons (yellow) serve as interconnects. Calibration curves for (b) horizontal and vertical ECR resistors and (c) Wheatstone bridge obtained by horizontal uniaxial tension tests. (d) FEM strain distribution in ECR when the supporting Tegaderm substrate is stretched horizontally by 5%. (e) Voltage outputs from the ECR Wheatstone bridge during normal and deep breath. (f) Voltage outputs from the ECR Wheatstone bridge during cough.

5.7 DOUBLE-STRANDED STRETCHABLE ANTENNA

In the ESS we exploited a double-stranded design for the wireless epidermal strain sensor. The resonant frequency of this sensor coil can be altered by changing its inductance through mechanical loadings such as stretching or bending, providing a direct correlation between local skin deformation with the electrical resonant frequency. This planar stretchable coil has the potential to work as a near field communication (NFC) antenna for wireless data transmission. Details about the design and analysis of this stretchable coil sensor will be discussed in Chapter 6.

5.8 MECHANICAL STUDY

5.8.1 Stretchability Study

Since human skin can be stretched up to 30% without causing serious damage [163], it's important for the epidermal sensor system to exhibit higher stretchability in order to survive different kinds of skin deformations. The stretchabilities of different serpentine ribbons on Tegaderm substrates were tested using a customized tensile tester with *in situ* resistance measurement and top down webcam observation, which is similar to the experimental setup for Tegaderm-supported ITO serpentine, as shown in Figure 3.2 (a). The resistance results are plotted in Figure 5.6 and close-up top view optical images are shown in Figure 5.7. According to Figure 5.6, while straight Al-on-PET and Au-on-PET ribbons exhibit limited stretchability (2.89% and 13.72%, respectively), their serpentine-shaped ribbons as shown in Figure 5.7 (a) (Al coil), Figure 5.7 (b) (Au EP electrode) and Figure 5.7 (c) (Au RTD), are much more stretchable, well beyond the elastic limit of human skin (30%). For serpentine ribbons such as the Al coil and Au RTD, rupture sites are always found at the crest of the arc (Figure 5.7 (a)&(c)) whereas for serpentine network such as the Au EP electrode, fracture first occurs at ribbon intersections (Figure 5.7 (b)) due to strain concentrations and overcutting at turning points (Figure 4.4 (d)-(i)).

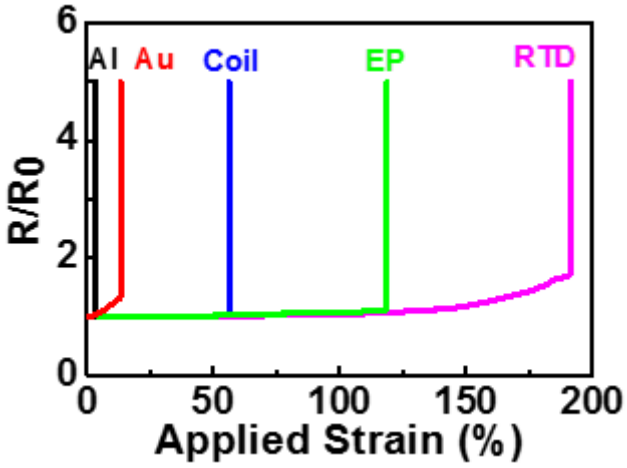

Figure 5.6 Resistance change measured as function of applied strain. “Al” denotes straight Al-PET ribbon, “Au” denotes straight Au-PET ribbon, “Coil” denotes Al-PET serpentine ribbon used in wireless strain sensor coil, “EP” denotes Au-PET serpentine ribbon used in EP electrode, and “RTD” denotes Au-PET serpentine ribbon used in RTD.

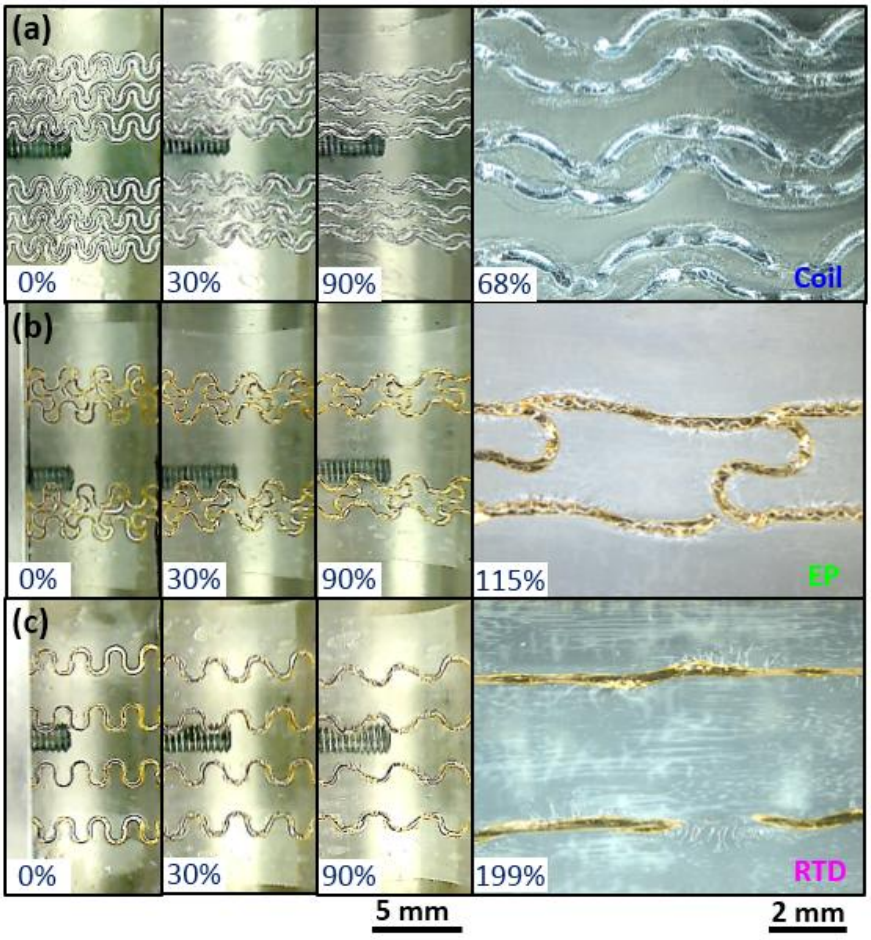

Figure 5.7 In situ images of different serpentine ribbons on Tegaderm stretched to certain strains. (a) Al coil serpentine at different applied strain up to its strain-to-rupture. (b) Au EP serpentine at different applied strain up to its strain-to-rupture. (c) Au RTD serpentine at different applied strain up to its strain-to-rupture.

5.8.2 Cyclic Stretch Test Study

Except for stretchability, the electrical performance of the sensors under cyclic loading is also of great importance. This is because skins near joints such as ankle and waist often undergo repeated stretching, which results in cyclic loading for any epidermal sensor that is attached to those locations. To ascertain that epidermal sensors preserve full functionality under repeated loading, cyclic uniaxial stretch tests with 20% and 30% peak strains have been performed. Figure 5.8 shows the cyclic test result for RTD and it is evident that the resistance remains unchanged up to several hundred numbers of cycles for 20% peak strain and stays stable for 100 cycles for 30% peak strain, which suggests the device exhibit good performance under repeated loading.

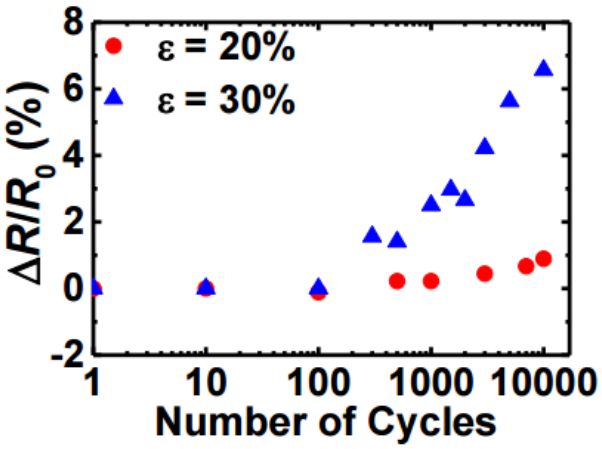

Figure 5.8 Cyclic test for RTD. Peak strain of 20% and 30% are applied on RTD and the resistance result shows the device is robust up to several hundreds number of cycles.

5.8.3 Deformability Study

A deformability study was also conducted to evaluate the system-level mechanical response of the epidermal sensor system, as shown in Figure 5.9. The patch has been subjected to different loading conditions such as stretching, compression, shear as well as surface rub and surface poking. Due to the small thickness and stretchable serpentine structure, the entire patch retains intimate contact with the skin under various loadings therefore exhibits high deformability. The electrical resistance of the Al and Au serpentines before and after various kinds of skin deformation is provided in Figure 5.10. It is evident that the ESS can survive all possible skin deformations without any mechanical degradation.

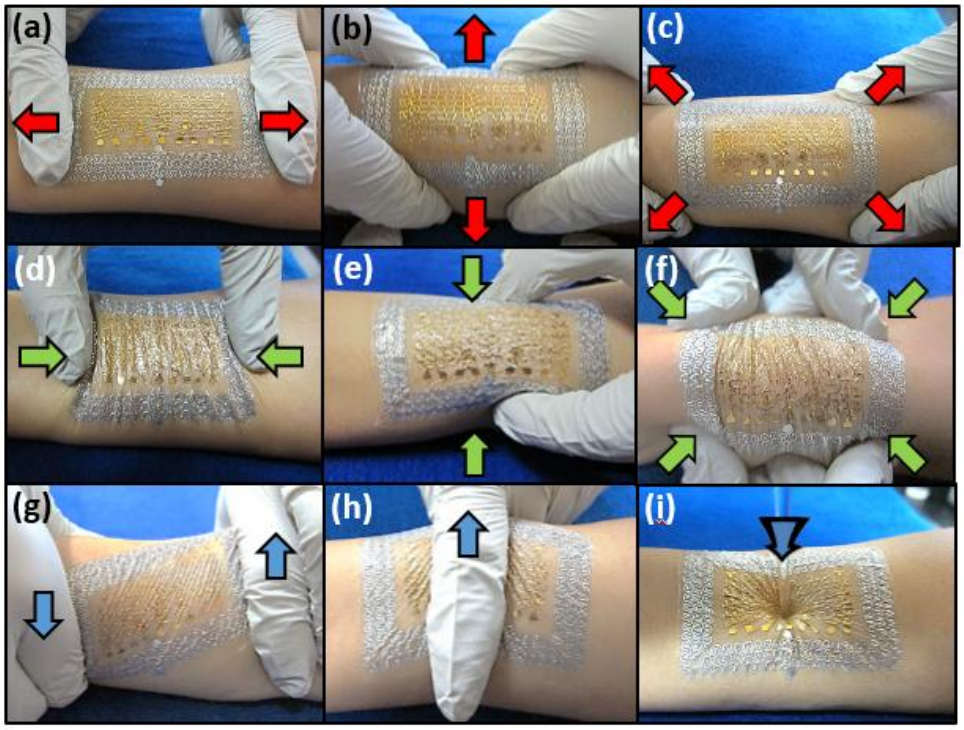

Figure 5.9 Deformability of ESS on human skin. Tattoo-paper supported ESS under (a) longitudinal stretch (b) transverse stretch (c) biaxial stretch (d) longitudinal compress (e) transverse compress (f) biaxial compress (g) shear (h) rub (i) poking by a glass rod.

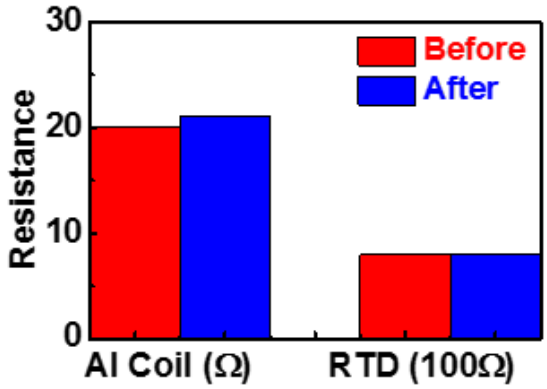

Figure 5.10 Resistance of Al coil and Au RTD before and after all possible deformations of skin-mounted ESS.

5.8.4 Substrate Study

Since the "cut-and-paste" fabrication method is not sensitive to the substrate material, as long as the compliant target substrate adheres sufficiently well to the thin film ESS, it can be transfer-printed onto different substrate materials. Figure 5.11 shows ESS on three different types of substrates. While Tegaderm and tattoo papers are thin, transparent and truly skin-like (Figure 5.11 (a)-(h)), the KRST is much thicker and behaves like a cloth tape (Figure 5.11 (i)-(l)). Because of its relatively large thickness, KRST does not crumple after being peeled off from the skin and the silicone adhesive allows multiple attachment and detachment before losing adhesion.

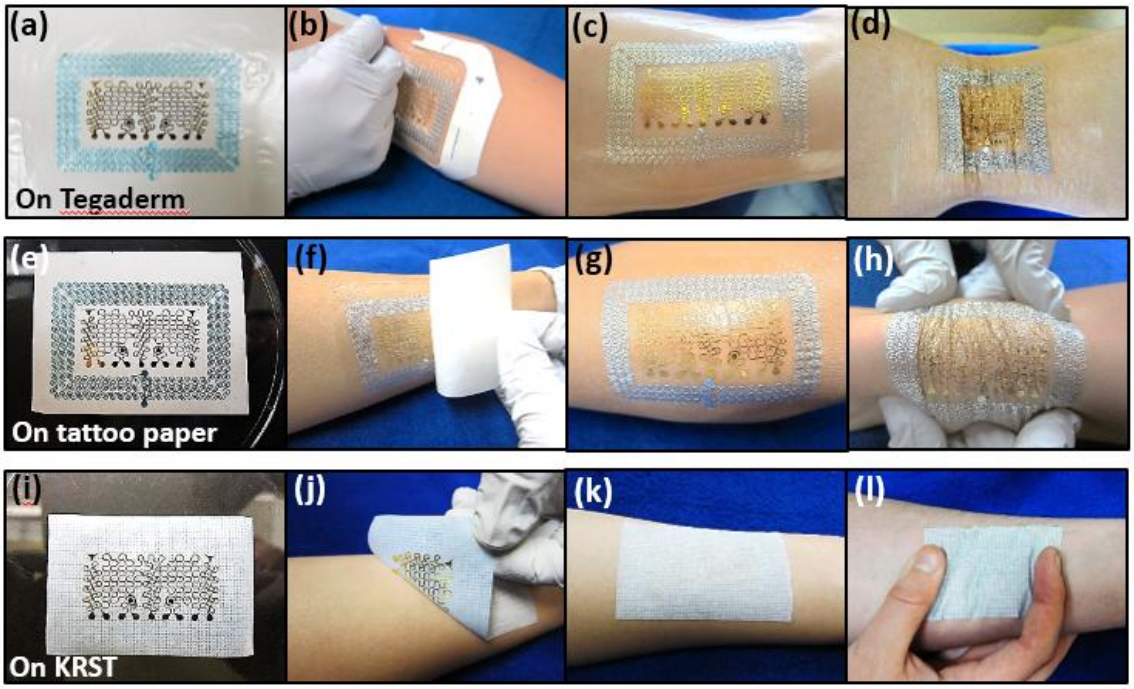

Figure 5.11 ESS on different substrates. (a) ESS on Tegaderm. (b) Applying ESS on the crook of the elbow. (c) As applied ESS. (d) ESS when elbow bends. (e) ESS on tattoo paper. (f) Applying ESS on forearm. (g) As applied ESS. (h) ESS under compression. (i) ESS on KRST. (j) Applying ESS on skin. (k) As applied ESS. (l) ESS under compression.

5.8.5 Material Behavior

This study involves a variety of different materials in order to yield high performance ESS. In order to fully understand the mechanical properties of different materials and their effect on the ultimate mechanical performance of ESS, we have conducted mechanical property tests, using a dynamic mechanical analyzer (RSA-G2, TA Instruments), for all the materials involved. Specimens were cut into rectangular strips with an aspect ratio of 10:1 and were pulled in the longitudinal direction. Repeated tests have been conducted and the representative stress-strain curves are offered in Figure 5.12 (a)&(b) and Table 5.1. Since Tegaderm has been mainly adopted in this work, its mechanical behavior is studied in detail. Tegaderm comprises a backing layer and an adhesive layer, whose mechanical responses are quite different. The top view of Tegaderm tape and the stress-strain curves for both layers are plotted in Figure 5.12 (c)&(d).

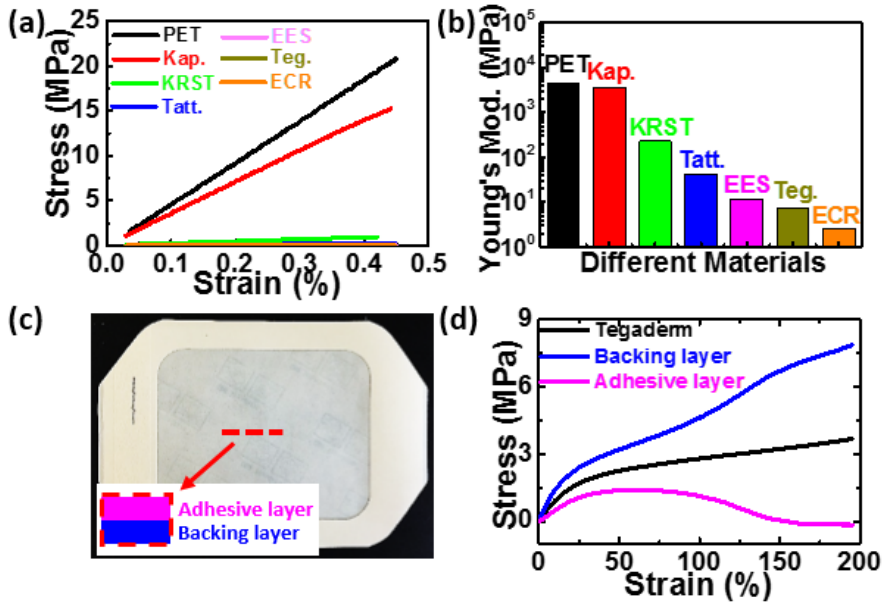

Figure 5.12 Stress-strain behavior of involved materials. (a) Uniaxial stress-strain curves of PET, Kapton, kind removal silicone tape (KRST), tattoo paper, ESS, Tegaderm, and ECR. (b) Bar plot of the Young's moduli in log scale. (c) Top view of Tegaderm, inset showing cross section of Tegaderm. (d) Uniaxial stress-strain curves of Tegaderm, Tegadmer backing layer and Tegaderm adhesive layer.

Material	Thickness (μm)	Young's Modulus (GPa)
PET (Goodfellow)	13	4.59
Kapton (Dupont)	12.7	3.59
KRST (3M)	200	0.228
Tattoo adhesive (Silhouette)	22	0.042
ESS on Tegaderm	60	0.011
Tegaderm (3M)	47	0.007
ECR (Wacker)	120	0.003

Table 5.1 List of measured Young's modulus of different materials used in ESS

5.9 CHAPTER SUMMARY

In this chapter, we have demonstrated a multimaterial, multiparametric ESS based on serpentine designs, which is compliant and stretchable such that it can be intimately but noninvasively applied on human skin to measure ECG, EMG, EEG, skin temperature, skin hydration and respiratory rate. The ESS has potential to communicate with external receivers wirelessly through the on-board double-stranded stretchable coil, which will be discussed in detail in next chapter.

Chapter 6 Serpentine-Based Stretchable Sensor Coil[1]

The biological signals captured by epidermal sensors should be wirelessly transmitted to data analytic devices. Conventional lead-wire based data transmission system is obstructive, and the movement of the lead wires can significantly contribute to moving artifacts. To transmit data with high fidelity and unobstructively, near field communication (NFC) represents a wireless and safe strategy. This chapter discusses the design, manufacture and experimental testing of a planar stretchable coil integrated on the ESS that can operate as an antenna near NFC frequencies. The stretchable coil can also be applied as a wireless, skin-mounted strain sensor which is applicable for detecting hand gestures. The coupled mechanoelectromagnetic performance of the stretchable coil is investigated experimentally, numerically and analytically.

[1] S. Yang, Y.-C. Chen, L. Nicolini, P. Pasupathy, J. Sacks, B. Su, R. Yang, D. Sanchez, Y.-F. Chang, P. Wang, D. Schnyer, D. Neikirk, N. Lu*, "*"Cut-and-Paste" Manufacture of Multiparametric Epidermal Sensor Systems*," Advanced Materials, vol. 27, no. 41, pp. 6423-6430, Nov 4, 2015.
Author contributions: S. Y., Y.-C. C., L. N., P. P., B. S., R. Y., N. L., D. N., and D. S. conducted device design, fabrication, calibration, and testing. S. Y. led the FEM analysis with J. S. and D. S.'s assistance. Y. C., P. W., S. Y., Y.-C. C., L. N. and R. Y. served as human subjects. L. N. and D. N. performed EP analysis. N. L., D. N., and D. S. supervised and coordinated the project. N. L., S. Y., Y.-C. C., L. N., P. P., D. N., and D. S. wrote the paper.

6.1 OBJECTIVE AND OVERVIEW

Human body biological signals such as ECG, EMG, EEG, skin temperature, skin hydration, and respiratory rate can be faithfully measured by ESS discussed in Chapter 5. However, it takes extra effort to transmit the measured data to external data processing system. Conventional lead-wire based data transmission systems are obstructive, and the movement of the lead wires can significantly contribute to moving artifacts. To establish a high performance, ambulatory monitoring ESS, a compliant, stretchable and wireless data transmission component has to be established. For example, a skin-like, stretchable NFC antenna is desirable. The development of wireless antennas includes antennas for soil-structure interfaces [164], structural health monitoring [165], and microfluidic radiofrequency antennas [166]. In addition, flexible wireless passive antennas have also been proposed for pressure measurements [167, 168] and biomedical applications [169], although, their stretchabilities are limited. One paradigm-shifting design for stretchable antenna was proposed in 2011 [63], in which the antenna was fabricated as serpentine coils in order to enhance its stretchability and compliance with preserved electrical functionality. The idea of serpentine coil is then developed in many studies [119, 120] in which thin and stretchable coils on epidermal electronics are exploited for NFC data transmission. In this chapter, we propose a double-stranded serpentine coil that exhibits high stretchability and a low resonant frequency, which can be fabricated by the "cut-and-paste" method introduced in Chapter 4, and can be used as a hand gesture detector and antenna for wireless communication.

6.2 COIL DESIGN

The resonant frequency (f) of sensor coils depend on their inductance (L_s) and capacitance (C_s) through the equation

$$f_s = \frac{1}{2\pi\sqrt{L_s C_s}} \tag{6.1}$$

As we hope to build a low frequency RLC coil that operates below 100 MHz for easier measurement and for future use as an NFC antenna, Equation (6.1) suggests that the coil should have high inductance and capacitance. Since we used a parallel plate capacitor in the design and the overall capacitance is fixed to be 3.76 pF, a coil with large inductance is preferred. Inductance depends on the layout of the coil. For a planar coil, its inductance depends on the number of turns, shape of the turns, and the area that is enclosed by the coil [170-173]. In general, the larger the area, the more turns, the higher the inductance, which conflicts with the need of building a wireless strain sensor that is small enough to be attached to many locations on the human body. Another design goal is to make it highly stretchable and compliant so that it doesn't mechanically load the skin. Last but not least, it is desirable to have highly strain-dependent inductance for high sensitivity measurement. With the aforementioned constraints and goals, we exploited a double-stranded serpentine design shown as the blue coils in Figure 5.1. This design helps maximize the use of limited real estate to fill in as many serpentine-shaped turns as possible. In the maintime it leaves a reasonable gap between serpentines so that stretchability of the coil is ensured.

6.3 EXPERIMENTAL MEASUREMENT

Figure 6.1 illustrates the wireless measurement on the sensor coil. A circular reader coil is connected to an Impedance Analyzer (HP 4194A) via a standard BNC-RCA adaptor. Figure 6.1 (a) shows the experimental setup and the reader is inductively coupled to the sensor coil in a transformer like configuration, so there is no cable connection between the reader and the sensor coil (Figure 6.1 (b)). In our wireless strain sensor, the planar inductor (L_s) and capacitor (C_s) together with the inductor's parasitic resistance (R_s) forms an RLC

resonant circuit. The reader coil inductor (L_r) has its own series parasitic resistance (R_r) and capacitance (C_r) which also forms an RLC circuit. Thus the reader and the sensor together form two coupled RLC resonant circuits with a coupling factor of *k*. The HP4194A is used to obtain the swept-frequency impedance response of the two coupled circuits. The parasitic capacitance induced by connectors and adaptors which connect the reader coil to the HP4194A add to C_r and hence lower f_r. The baseline response is that of the reader coil:

$$Z_{in} = C_r||(R_r + j\omega L_r) \tag{6.2}$$

where $||$ represents parallel circuit combination, ω is the angular frequency in radians/sec, and Z_{in} is the complex input impedance as a function of frequency. When the sensor is present, the input impedance is given by

$$Z_{in} = C_r||\left(R_r + j\omega L_r + \frac{\omega^2 M^2}{\left(R_s + j\omega L_s + \frac{1}{j\omega C_s}\right)}\right) \tag{6.3}$$

where *M* is the mutual inductance between the reader and sensor coils. The HP4194A measures both magnitude $|Z_{in}|$ in Ohms (Ω) and the Phase (θ) in degrees ($^\circ$). For this work, we use the phase response to determine the resonant frequency. By design we have ensured that $f_s \ll f_r$ which affords reliable estimation of the sensor's resonant frequency without perturbation from the reader's resonance. Thus the baseline response corresponds to the phase of the reader coil is around 90°. When the sensor is coupled to the reader, we observe a dip in the phase baseline with the minima point corresponding to the sensors resonant frequency (f_s). The size (i.e. deviation from the baseline) of this dip is dependent on the distance and orientation between the reader and the sensor coils as a result of changing coupling factor *k*. However the frequency corresponding to the dip, i.e. f_s, is independent of these changes. Thus one can reliably estimate f_s from this coupled but wireless measurement.

Uniaxial stretch tests has been performed on Tegaderm supported stretchable coils and strain-induced shift of resonant frequency of the coupled circuit has been recorded, as shown in Figure 6.1 (c), which shows a monotonic decay as the sensor coil is uniaxially elongated. The resonant frequency shifted from 38.6 MHz in the undeformed shape down to 34.3 MHz at the strain of 20%, which is more sensitive to deformation compared to a previously reported stretchable epidermal antenna [120].

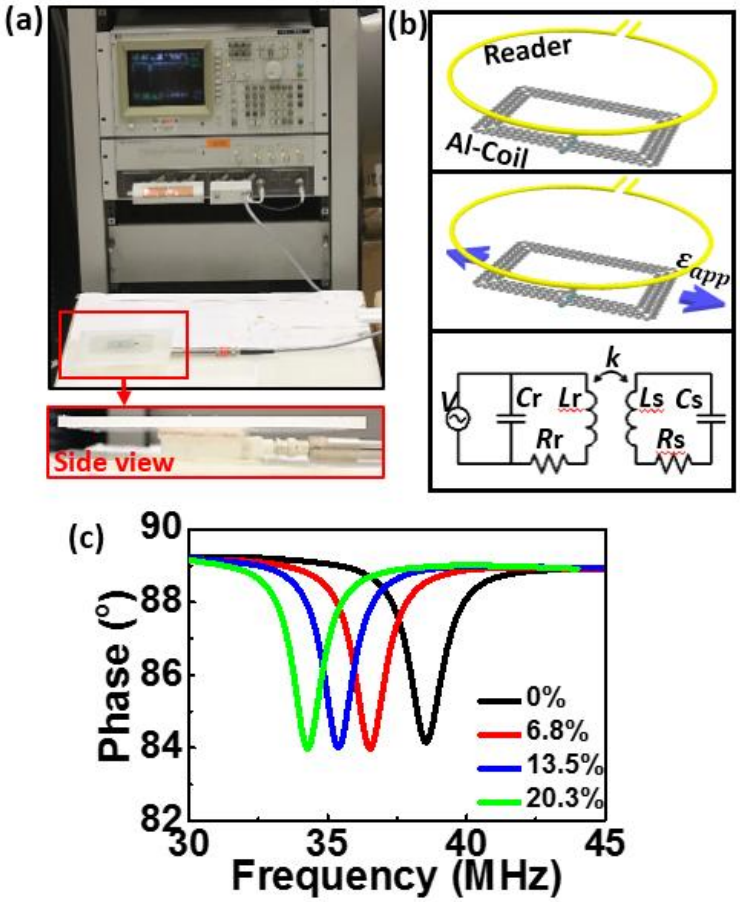

Figure 6.1 (a) Experimental setup for the measurement of the resonant frequency of the coupled system. The sensor coil is placed on top of the reader coil and separated by a 6 mm thick acrylic slab plus 4 mm air gap. The reader is connected to an Impedance Analyzer (HP 4194A). (b) Schematics of the wirelessly coupled reader and sensor coils. (c) Phase response of the coupled system as a function of sweeping frequency at different applied strains.

6.4 ANALYTICAL RESULT

Here we try to develop an analytical understanding of the inductance change with applied strain. The inductance of a planar, rectangular, single turn coil is approximately proportional to the square root of the area that is enclosed by the coil [171]. Thus

$$L \sim \sqrt{A} \sim \sqrt{l_1 l_2}, \tag{6.4}$$

where l_1 and l_2 are the initial length and width of the rectangle. Assuming the coil is bonded to a substrate with Poisson's ratio ν, when stretched by a strain of ε in direction 1, the deformed length and width becomes

$$l_{1(\varepsilon)} = (1+\varepsilon) l_1, \; l_{2(\varepsilon)} = (1-\nu\varepsilon) l_2. \tag{6.5}$$

Therefore the inductance of the deformed coil is

$$L_{(\varepsilon)} \sim \sqrt{A_{(\varepsilon)}} \sim \sqrt{A(1+\varepsilon)(1-\nu\varepsilon)} \sim L_0 \sqrt{(1+\varepsilon)(1-\nu\varepsilon)} \tag{6.6}$$

and hence the strain dependence of the resonant frequency is given by

$$f_{(\varepsilon)} = \frac{1}{2\pi\sqrt{L_{(\varepsilon)} C}} \sim f_0 \frac{1}{[(1+\varepsilon)(1-\nu\varepsilon)]^{0.25}} \sim f_0 \left(1 + \frac{1}{4}(\nu - 1)\varepsilon\right). \tag{6.7}$$

For a multi-turn planar rectangular coil, existing theory [170] has been extended to predict coil inductance under different applied strains. The inductance of a multi-turn rectangular coil is formulated as

$$L = \sum L_0 + \sum M, \tag{6.8}$$

where L is the total inductance, L_0 is the self-inductance of each straight segment and M is the mutual-inductance between any two segments. The self-inductance is given by

$$L_0 = 0.002 l \left[ln\left(\frac{2l}{GMD}\right) - 1.25 + \frac{AMD}{l} + \left(\frac{\mu}{4}\right) T \right], \tag{6.9}$$

in which *GMD* is the geometric mean distance and *AMD* is the arithmetic mean distance, both depending on the coil geometry and l is the segment length, T is the frequency correction parameter which is taken to be 1 m/H and μ is the magnetic permeability and is also set to be 1 H/m. The mutual-inductance is given by

$$M = 2lQ, \tag{6.10}$$

where Q is a parameter depending on the geometry of the segment

$$Q = ln\left\{\frac{1}{\beta} + \left(1 + \frac{1}{\beta^2}\right)^{0.5}\right\} - (1 + \beta^2)^{0.5}, \tag{6.11}$$

where $\beta = GMD/l$.

So given a rectangular coil with straight segments and uniform cross section, the total inductance of the coil solely depends on the layout of the coil, and the total inductance can be calculated in an iterative manner.

6.5 SIMULATION RESULTS

Finite element analysis was performed to model the inductance change of the sensor coil (one layer coil) with applied uniaxial tension. The mechanical deformation was modeled by ABAQUS and the inductance was modeled by ANSYS Maxwell. In ABAQUS, the sensor coil was modeled as Tegaderm-bonded serpentine-shaped wires with rectangular cross-sections and the entire structure was subjected to horizontal tensile displacement. The deformed shape of the coils was imported into ANSYS Maxwell and a 3D model was generated with rectangular cross-section 9 μm × 400 μm assigned to the coil. The coil was immersed in a rectangular box of atmosphere of size: 500 mm × 500 mm × 750 mm, to account for the dielectric effect of the surrounding air. Two extension wires were used to lead the two ports of the coil to the boundary of the atmospheric box (Figure 6.2 (a), atmosphere box not showing) and a current excitation of 1 A was applied across the ports. The solution type of "Magnetostatic" was selected and the magnetic flux density fields (B field) of the deformed coils are computed (Figure 6.2 (b)). Coil inductance is a direct output of the solution. Once numerical solutions of the sensor coil inductance are available, assuming capacitance to be unaffected by stretch, we are able to calculate the resonant frequency of the stretched sensor using Equation (6.1). This result is plotted in Figure 6.2

(c) as blue, square markers. It is evident that our FEM results can predict the decrease of resonant frequency as a result of increasing inductance when the coil is uniaxially stretched. But there is still a big discrepancy between experimental and FEM results, which requires future investigation.

To reveal the effect of serpentine, the straight counterpart of the serpentine coil has also been modeled, both are bonded on Tegaderm substrates and subjected to the same tensile strains. The resonant frequency results of straight coils are plotted in Figure 6.2 (c) as the blue, triangle markers, which is almost stationary under stretch (39.4MHz for 0% and 39.2MHz for 30%). Therefore, serpentine coils are ideal for wireless skin strain sensing as it is both more deformable and more sensitive to strain. However, when using those coils as NFC antenna, the fact that the resonant frequency of straight coils is less sensitive to mechanical strain compared with its serpentine counterpart poses a very interesting tradeoff between deformability and stability of frequency.

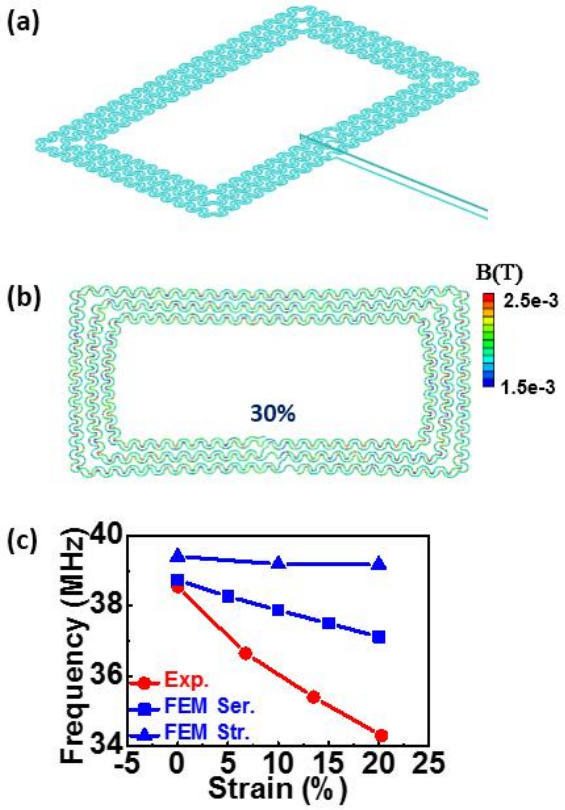

Figure 6.2 (a) 3D model of the coil with extension wire (atmosphere box is not showing). (b) Serpentine coil under 30 % applied strains with contour plot of the magnetic (B) filed magnitude. (c) Both experimental (red) and FEM (blue) results showing decreased resonant frequency with increased tensile strain.

6.6 APPLICATION

6.6.1 Hand Gesture Recognition

The measurement of skin deformation is performed by attaching the sensor coil on the dorsal wrist and bringing the reader coil within 45 mm of the sensor coil. Three layers of tattoo paper (Silhouette) are applied between the sensor coil and the skin to compensate for capacitive loading induced by the skin. Three repeated wrist gestures “flat”, “stretch”, and “compress” are measured (Figure 6.3 (a)) and phase measurement for the three gestures are plotted in Figure 6.3 (b), which reveals several interesting findings. First, the resonant frequency drops from 38.6 MHz to 13.92 MHz before and after the sensor coil is applied to the skin, which is due to the substantial capacitive loading induced by the skin [119].The second observation is that “stretch” reduces the resonant frequency (from 13.92 MHz to 12.99 MHz) whereas “compress” slightly increases resonant frequency (from 13.92 MHz to 14.41 MHz), as expected. Figure 6.3 (b) also suggests that the wireless strain gauge coil can offer very repeatable measurements of joint bending.

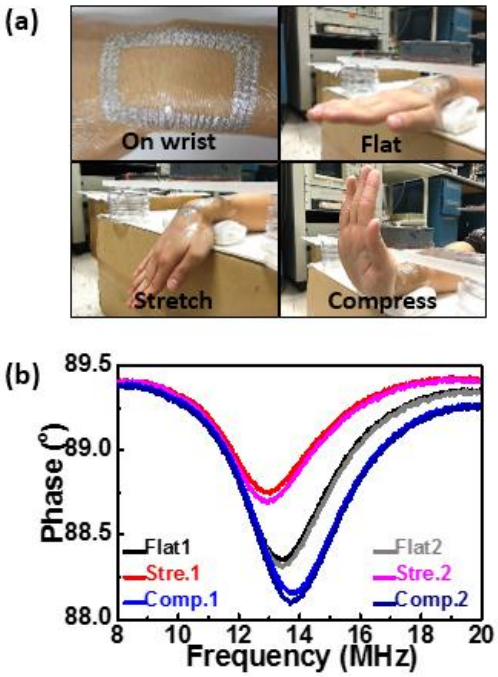

Figure 6.3 (a) Sensor coil attached on human wrist (top left) under different hand gestures: "flat" (top right), "stretch" (bottom left) and "compress" (bottom right). (b) Phase response as a function of sweeping frequency at repeated "flat", "stretch" and "compress" hand position. Good repeatability is observed.

6.6.2 NFC Antenna

The planar stretchable coil also has the potential to work as an NFC antenna for transferring the local signals measured by the ESS wirelessly to a remote receiver [120]. In order to transfer data properly, the resonant frequency should stay as steady as possible during the transfer process. We therefore test the coil response when it is placed on a human chest and the subject inhales and exhales deeply, as shown in Figure 6.4 (a). Figure 6.4 (b) indicates that the resonant frequency only changed from 13.06 MHz to 12.80 MHz, for either deep inhalation or exhalation. The insensitivity of resonant frequency to chest deformation associated inhalation and exhalation makes it possible to use the planar stretchable coil as a stable epidermal antenna for chest ESS.

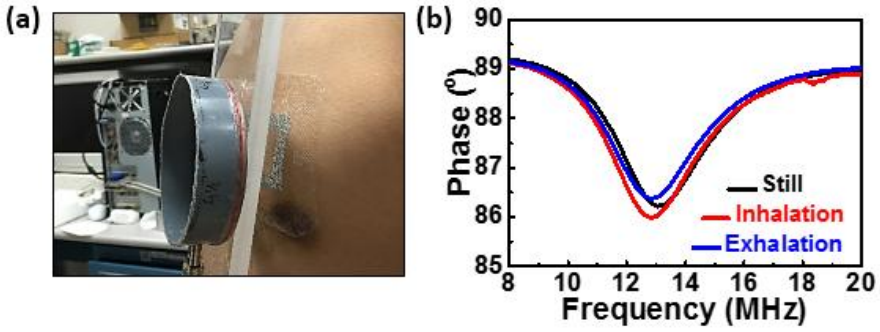

Figure 6.4 (a) Image for on-chest measurement. (b) Phase respond as a function of sweeping frequency at “still”, “inhalation”, and “exhalation” instant. It shows the resonant frequency and phase are stable in the three cases.

6.7 DISCUSSION

The effect of distance (coupling factor *k* as labeled in Figure 6.1 (b)) between the reader and the sensor coils has also been investigated, as shown in Figure 6.5. It is evident that the resonant frequency does not depend on the distance whereas the phase dip does. Specifically, the smaller the gap, the larger the phase dip, thus the higher coupling factor.

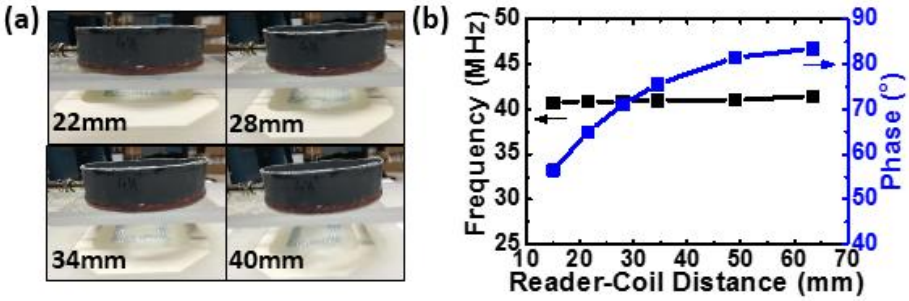

Figure 6.5 (a) Images of different separation distance between reader and the Al coil. (b) Plots of resonant frequency (black) and phase (blue) as function of reader-coil distance. It shows the resonant frequency is unaffected by the reader-coil distance whereas the phase depends on it.

6.8 CHAPTER SUMMARY

In this chapter, we have introduced the design of a stretchable double-stranded serpentine coil that can be used for hand gesture recognition and as an epidermal antenna for wireless data communication. Detailed experiments as well as analytical and numerical solutions have been discussed. Our study suggests that the resonant frequency of the stretchable coil decreases as the coil is stretched. The numerical result also shows that the resonant frequency of coils with straight segments are much less sensitive to the applied strain compared to the serpentine coils. This indicates that there is a tradeoff between the stretchability and frequency stability of planar coils. When the coil is laminated on human skin, we find that its resonant frequency is sensitive to skin loading. Further work is required for the optimization of compliant stretchable antennas.

Chapter 7 Conclusions and outlook

The last chapter summarizes this thesis work and proposes suggestions for future endeavors along this route.

7.1 SUMMARY AND CONCLUDING REMARKS

Echoing back to the introduction in Chapter 1, the goal of this dissertation is to understand the fundamental mechanics of serpentine-shaped stretchable structures and propose an affordable method for manufacturing disposable yet high performance epidermal sensors for reliable vital sign monitoring.

Two most commonly used serpentine configurations for stretchable structures, i.e. freestanding serpentine structures and substrate-supported serpentine structures have been systematically studied. For freestanding serpentine structures, it was found that the serpentine structure is actually not always more stretchable, yet always "more compliant", than its straight counterpart. Analytical solutions using simple curved beam theory and more rigorous elasticity theory have both been derived to calculate the stretchability and effective stiffness of freestanding serpentine structures, which have been validated both numerically and experimentally. An example for optimizing serpentine shapes under practical constraints has also been offered. For substrate-supported metallic and ITO serpentine ribbons, in situ electrical resistance measurement during uniaxial stretching with top down microstructure observation has been carried out. The study reveals that, while high substrate stiffness completely prevents serpentine ribbons from in-plane rotation or out-of-plane twist, serpentines on compliant substrates are not necessarily as stretchable as freestanding ones because transverse buckling can crack brittle serpentine ribbons that are well bonded on the compliant substrates.

As the conventional microfabrication process for serpentine based inorganic stretchable electronics is time and labor intensive, a dry, benchtop, and freeform manufacturing method named the "cut-and-paste" method for the fabrication of stretchable and disposable epidermal sensors has been proposed in this thesis. Various fabrication parameters have been investigated and optimized manufacturing guidelines have been

proposed. As a demonstration of the cost and time effective "cut-and-paste" method, we have manufactured a multimaterial, multiparametric epidermal sensor systems (ESS), which can be intimately but noninvasively laminated on human skin to monitor electrophysiological signals, skin temperature, skin hydration and respiratory rate. The ESS may potentially harvest energy from and communicate with wireless interrogators through the on-patch double-stranded stretchable coil. Design, measurement, and coupled mechanical-electromagnetic modeling of the stretchable coil structure have been discussed in details.

Overall, the research goals of this dissertation have been fulfilled. The mechanics of serpentine structures was systematically investigated with emphasis on the effects of serpentine geometry and substrate stiffness, which involves theoretical analysis, numerical simulation, and experimental validation. To manufacture high quality serpentine ribbons with high throughput and low cost, we have invented a "cut-and-paste" method to fabricate both metallic and ceramic serpentines. As a demonstration of our method, a noninvasive, tattoo-like multifunctional epidermal sensor system has been built for the measurement of various vital signs. Engineering of epidermal stretchable antenna for wireless communication is also detailed and rationalized.

7.2 SUGGESTIONS FOR FUTURE WORK

Here are some thoughts and suggestions for future endeavors:

1. It will be very helpful to develop closed-form analytical solutions for the buckling and post buckling analysis for freestanding serpentine networks, not only because it is a very interesting mechanics problem, but also it will be important for the combined mechanical and electrical circuit design of stretchable devices based on such structures.

2. The current "cut-and-paste" fabrication is far from perfect and improvements can be made. Some good starting points include but not limited to the improvement of the

cutting resolution and uniformity, specimen thinness, and process automation.

3. More medical sensors and actuators such as blood pressure sensor, blood-oxygen monitor, transdermal heaters, and drug delivery systems can be integrated in the "cut-and-paste" fabricated ESS, to form a closed-loop monitoring and treatment medical system.

4. In the simulation of stretchable coils, instead of performing the mechanical stretch and electromagnetic frequency analyses in two different modules, carrying out the two simulations in one software package such as ANSYS allow for coupling and may yield simulation results that can better reproduce the experimental results.

References

[1] C. Brunetti, and R. W. Curtis, "Printed-Circuit Techniques," *Proceedings of the Institute of Radio Engineers,* vol. 36, no. 1, pp. 121-161, 1948.

[2] J. Y. Ouyang, C. W. Chu, C. R. Szmanda *et al.*, "Programmable polymer thin film and non-volatile memory device," *Nature Materials,* vol. 3, no. 12, pp. 918-922, Dec, 2004.

[3] P. F. Baude, D. A. Ender, M. A. Haase *et al.*, "Pentacene-based radio-frequency identification circuitry," *Applied Physics Letters,* vol. 82, no. 22, pp. 3964-3966, Jun 2, 2003.

[4] E. Cantatore, T. C. T. Geuns, G. H. Gelinck *et al.*, "A 13.56-MHz RFID system based on organic transponders," *Ieee Journal of Solid-State Circuits,* vol. 42, no. 1, pp. 84-92, Jan, 2007.

[5] D. H. Kim, N. S. Lu, R. Ghaffari *et al.*, "Materials for multifunctional balloon catheters with capabilities in cardiac electrophysiological mapping and ablation therapy," *Nature Materials,* vol. 10, no. 4, pp. 316-323, Apr, 2011.

[6] D. H. Kim, S. D. Wang, H. Keum *et al.*, "Thin, Flexible Sensors and Actuators as 'Instrumented' Surgical Sutures for Targeted Wound Monitoring and Therapy," *Small,* vol. 8, no. 21, pp. 3263-3268, Nov 5, 2012.

[7] F. Garnier, R. Hajlaoui, A. Yassar *et al.*, "All-Polymer Field-Effect Transistor Realized by Printing Techniques," *Science,* vol. 265, no. 5179, pp. 1684-1686, Sep 16, 1994.

[8] Z. N. Bao, Y. Feng, A. Dodabalapur *et al.*, "High-performance plastic transistors fabricated by printing techniques," *Chemistry of Materials,* vol. 9, no. 6, pp. 1299-1301, Jun, 1997.

[9] J. A. Rogers, Z. Bao, K. Baldwin *et al.*, "Paper-like electronic displays: Large-area rubber-stamped plastic sheets of electronics and microencapsulated electrophoretic inks," *Proceedings of the National Academy of Sciences of the United States of America,* vol. 98, no. 9, pp. 4835-4840, Apr 24, 2001.

[10] K. I. Jang, S. Y. Han, S. Xu *et al.*, "Rugged and breathable forms of stretchable electronics with adherent composite substrates for transcutaneous monitoring," *Nature Communications,* vol. 5, Sep, 2014.

[11] D. J. Lipomi, B. C. K. Tee, M. Vosgueritchian *et al.*, "Stretchable Organic Solar Cells," *Advanced Materials,* vol. 23, no. 15, pp. 1771-1775, Apr 19, 2011.

[12] D. J. Lipomi, H. Chong, M. Vosgueritchian *et al.*, "Toward mechanically robust and intrinsically stretchable organic solar cells: Evolution of photovoltaic properties with tensile strain," *Solar Energy Materials and Solar Cells,* vol. 107,

pp. 355-365, Dec, 2012.
[13] C. Lungenschmied, G. Dennler, H. Neugebauer *et al.*, "Flexible, long-lived, large-area, organic solar cells," *Solar Energy Materials and Solar Cells,* vol. 91, no. 5, pp. 379-384, Mar 6, 2007.
[14] M. He, J. H. Jung, F. Qiu *et al.*, "Graphene-based transparent flexible electrodes for polymer solar cells," *Journal of Materials Chemistry,* vol. 22, no. 46, pp. 24254-24264, Dec 14, 2012.
[15] M. Kaltenbrunner, M. S. White, E. D. Glowacki *et al.*, "Ultrathin and lightweight organic solar cells with high flexibility," *Nature Communications,* vol. 3, pp. 770, Apr, 2012.
[16] K. S. Lee, Y. Lee, J. Y. Lee *et al.*, "Flexible and Platinum-Free Dye-Sensitized Solar Cells with Conducting-Polymer-Coated Graphene Counter Electrodes," *Chemsuschem,* vol. 5, no. 2, pp. 379-382, Feb 13, 2012.
[17] T. Someya, T. Sekitani, S. Iba *et al.*, "A large-area, flexible pressure sensor matrix with organic field-effect transistors for artificial skin applications," *Proceedings of the National Academy of Sciences of the United States of America,* vol. 101, no. 27, pp. 9966-9970, Jul 6, 2004.
[18] M. L. Hammock, A. Chortos, B. C. K. Tee *et al.*, "25th Anniversary Article: The Evolution of Electronic Skin (E-Skin): A Brief History, Design Considerations, and Recent Progress," *Advanced Materials,* vol. 25, no. 42, pp. 5997-6037, Nov, 2013.
[19] L. Li, H. T. Lin, S. T. Qiao *et al.*, "Integrated flexible chalcogenide glass photonic devices," *Nature Photonics,* vol. 8, no. 8, pp. 643-649, Aug, 2014.
[20] N. S. Lu, and D. H. Kim, "Flexible and Stretchable Electronics Paving the Way for Soft Robotics," *Soft Robotics,* vol. 1, no. 1, pp. 53-62, Mar, 2014.
[21] C. D. Dimitrakopoulos, and P. R. L. Malenfant, "Organic thin film transistors for large area electronics," *Advanced Materials,* vol. 14, no. 2, pp. 99-117, Jan 16, 2002.
[22] S. R. Forrest, "The path to ubiquitous and low-cost organic electronic appliances on plastic," *Nature,* vol. 428, no. 6986, pp. 911-918, Apr 29, 2004.
[23] P. F. Moonen, I. Yakimets, and J. Huskens, "Fabrication of Transistors on Flexible Substrates: from Mass-Printing to High-Resolution Alternative Lithography Strategies," *Advanced Materials,* vol. 24, no. 41, pp. 5526-5541, Nov 2, 2012.
[24] D. H. Kim, R. Ghaffari, N. Lu *et al.*, "Flexible and stretchable electronics for biointegrated devices," *Annu Rev Biomed Eng,* vol. 14, pp. 113-28, 2012.
[25] R. F. Service, "Materials science - Inorganic electronics begin to flex their muscle," *Science,* vol. 312, no. 5780, pp. 1593-1594, Jun 16, 2006.
[26] Y. G. Sun, and J. A. Rogers, "Inorganic semiconductors for flexible electronics," *Advanced Materials,* vol. 19, no. 15, pp. 1897-1916, Aug 3, 2007.
[27] G. S. Huang, and Y. F. Mei, "Thinning and Shaping Solid Films into Functional and Integrative Nanomembranes," *Advanced Materials,* vol. 24, no. 19, pp. 2517-

2546, May 15, 2012.
[28] W. N. Zhu, M. N. Yogeesh, S. X. Yang *et al.*, "Flexible Black Phosphorus Ambipolar Transistors, Circuits and AM Demodulator," *Nano Letters,* vol. 15, no. 3, pp. 1883-1890, Mar, 2015.
[29] H. Y. Chang, S. X. Yang, J. H. Lee *et al.*, "High-Performance, Highly Bendable MoS2 Transistors with High-K Dielectrics for Flexible Low-Power Systems," *Acs Nano,* vol. 7, no. 6, pp. 5446-5452, Jun, 2013.
[30] J.-H. A. Sang-Il Park, Xue Feng, Shuodao Wang, Yonggang Huang, and John A. Rogers, "Theoretical and Experimental Studies of Bending of Inorganic Electronic Materials on Plastic Substrates," *Advanced Functional Materials,* vol. 18, pp. 2673–2684, 2008.
[31] D. H. Kim, J. H. Ahn, W. M. Choi *et al.*, "Stretchable and foldable silicon integrated circuits," *Science,* vol. 320, no. 5875, pp. 507-511, Apr 25, 2008.
[32] S. P. Lacour, J. Jones, S. Wagner *et al.*, "Stretchable interconnects for elastic electronic surfaces," *Proceedings of the Ieee,* vol. 93, no. 8, pp. 1459-1467, Aug, 2005.
[33] E. Y. M. Z. Suo, H. Gleskova, and S. Wagner, "Mechanics of rollable and foldable film-on-foil electronics," *Applied Physics Letters,* vol. 74, 1999.
[34] A. Kumar, H. A. Biebuyck, N. L. Abbott *et al.*, "The Use of Self-Assembled Monolayers and a Selective Etch to Generate Patterned Gold Features," *Journal of the American Chemical Society,* vol. 114, no. 23, pp. 9188-9189, Nov 4, 1992.
[35] M. S. Miller, H. L. Filiatrault, G. J. E. Davidson *et al.*, "Selectively Metallized Polymeric Substrates by Microcontact Printing an Aluminum(III) Porphyrin Complex," *Journal of the American Chemical Society,* vol. 132, no. 2, pp. 765-772, Jan 20, 2010.
[36] P. C. Hidber, W. Helbig, E. Kim *et al.*, "Microcontact printing of palladium colloids: Micron-scale patterning by electroless deposition of copper," *Langmuir,* vol. 12, no. 5, pp. 1375-1380, Mar 6, 1996.
[37] T. Widlund, S. X. Yang, Y. Y. Hsu *et al.*, "Stretchability and compliance of freestanding serpentine-shaped ribbons," *International Journal of Solids and Structures,* vol. 51, no. 23-24, pp. 4026-4037, Nov, 2014.
[38] J. Song, "Mechanics of stretchable electronics," *Current Opinion in Solid State & Materials Science,* vol. 19, no. 3, pp. 160-170, Jun, 2015.
[39] H. Jang, Y. J. Park, X. Chen *et al.*, "Graphene-Based Flexible and Stretchable Electronics," *Adv Mater,* vol. Online, Jan 5, 2016.
[40] P. K. Yang, L. Lin, F. Yi *et al.*, "A Flexible, Stretchable and Shape-Adaptive Approach for Versatile Energy Conversion and Self-Powered Biomedical Monitoring," *Advanced Materials,* vol. 27, no. 25, pp. 3817-3824, Jul 1, 2015.
[41] S. Hong, H. Lee, J. Lee *et al.*, "Highly Stretchable and Transparent Metal Nanowire

Heater for Wearable Electronics Applications," *Advanced Materials,* vol. 27, no. 32, pp. 4744-4751, Aug 26, 2015.

[42] S. K. Lee, B. J. Kim, H. Jang *et al.*, "Stretchable Graphene Transistors with Printed Dielectrics and Gate Electrodes," *Nano Letters,* vol. 11, no. 11, pp. 4642-4646, Nov, 2011.

[43] H. C. Ko, M. P. Stoykovich, J. Z. Song *et al.*, "A hemispherical electronic eye camera based on compressible silicon optoelectronics (Supplementary Information)," 2008.

[44] D. H. Kim, R. Ghaffari, N. S. Lu *et al.*, "Electronic sensor and actuator webs for large-area complex geometry cardiac mapping and therapy," *Proceedings of the National Academy of Sciences of the United States of America,* vol. 109, no. 49, pp. 19910-19915, Dec 4, 2012.

[45] D. H. Kim, J. A. Rogers, J. Viventi *et al.*, "Flexible Biomedical Devices for Mapping Cardiac and Neural Electrophysiology," *2011 Ieee International Reliability Physics Symposium (Irps)*, 2011.

[46] J. Viventi, D. H. Kim, J. D. Moss *et al.*, "A Conformal, Bio-Interfaced Class of Silicon Electronics for Mapping Cardiac Electrophysiology," *Science Translational Medicine,* vol. 2, no. 24, Mar 24, 2010.

[47] D. Son, J. Lee, D. J. Lee *et al.*, "Bioresorbable Electronic Stent Integrated with Therapeutic Nanoparticles for Endovascular Diseases," *Acs Nano,* vol. 9, no. 6, pp. 5937-5946, Jun, 2015.

[48] N. S. Giulia Lanzara, Zhiqiang Guo, Fu-Kuo Chang, "A Spider-Web-Like Highly Expandable Sensor Network for Multifunctional Materials," *advanced materials,* vol. 22, no. 41, pp. 4643-4648, 2010.

[49] J. Y. Sun, N. S. Lu, J. Yoon *et al.*, "Debonding and fracture of ceramic islands on polymer substrates," *Journal of Applied Physics,* vol. 111, no. 1, Jan 1, 2012.

[50] Y. W. Su, Z. J. Liu, S. D. Wang *et al.*, "Mechanics of stretchable electronics on balloon catheter under extreme deformation," *International Journal of Solids and Structures,* vol. 51, no. 7-8, pp. 1555-1561, Apr, 2014.

[51] A. Roguin, E. Grenadier, B. Peled *et al.*, "Acute and 30-day results of the serpentine balloon expandable stent implantation in simple and complex coronary arterial narrowings," *American Journal of Cardiology,* vol. 80, no. 9, pp. 1155-1162, Nov 1, 1997.

[52] R. Beyar, A. Roguin, J. Hamburger *et al.*, "Multicenter pilot study of a serpentine balloon-expandable stent (beStent(TM)): Acute angiographic and clinical results," *Journal of Interventional Cardiology,* vol. 10, no. 4, pp. 277-286, Aug, 1997.

[53] D. Khang, H. Jiang, Y. Huang *et al.*, "A stretchable form of single-crystal silicon for high-performance electronics on rubber substrates," *Science,* vol. 311, no. 5758, pp. 208-212, JAN 13 2006, 2006.

[54] Y. Sun, W. Choi, H. Jiang *et al.*, "Controlled buckling of semiconductor nanoribbons for stretchable electronics," *Nature Nanotechnology,* vol. 1, no. 3, pp. 201-207, DEC 2006, 2006.

[55] Y. Sun, V. Kumar, I. Adesida *et al.*, "Buckled and wavy ribbons of GaAs for high-performance electronics on elastomeric substrates," *Advanced Materials,* vol. 18, no. 21, pp. 2857-2862, NOV 3 2006, 2006.

[56] W. Choi, J. Song, D. Khang *et al.*, "Biaxially stretchable "Wavy" silicon nanomembranes," *Nano Letters,* vol. 7, no. 6, pp. 1655-1663, JUN 2007, 2007.

[57] S. P. Lacour, S. Wagner, Z. Y. Huang *et al.*, "Stretchable gold conductors on elastomeric substrates," *Applied Physics Letters,* vol. 82, no. 15, pp. 2404-2406, Apr 14, 2003.

[58] N. Bowden, S. Brittain, A. G. Evans *et al.*, "Spontaneous formation of ordered structures in thin films of metals supported on an elastomeric polymer," *Nature,* vol. 393, no. 6681, pp. 146-149, May, 1998.

[59] B. D. Y. Xue Feng, Yuanming Liu, Yong Wang, Canan Dagdeviren, Zhuangjian Liu, Andrew Carlson, Jiangyu Li, Yonggang Huang, John A. Rogers, "Stretchable Ferroelectric Nanoribbons with Wavy Configurations on Elastomeric Substrates," *Acs Nano,* vol. 5, no. 4, pp. 3326–3332, 2011.

[60] N. Bowden, W. T. S. Huck, K. E. Paul *et al.*, "The controlled formation of ordered, sinusoidal structures by plasma oxidation of an elastomeric polymer," *Applied Physics Letters,* vol. 75, no. 17, pp. 2557-2559, Oct, 1999.

[61] W. T. S. Huck, N. Bowden, P. Onck *et al.*, "Ordering of spontaneously formed buckles on planar surfaces," *Langmuir,* vol. 16, no. 7, pp. 3497-3501, Apr, 2000.

[62] J. J. Stéphanie P. Lacour, Z. Suo, Sigurd Wagner, "Design and Performance of Thin Metal Film Interconnects for Skin-Like Electronic Circuits," *Ieee Electron Device Letters,* vol. 25, no. 4, pp. 179-181, 2004.

[63] D. H. Kim, N. S. Lu, R. Ma *et al.*, "Epidermal Electronics," *Science,* vol. 333, no. 6044, pp. 838-843, Aug 12, 2011.

[64] Y. W. Su, S. D. Wang, Y. A. Huang *et al.*, "Elasticity of Fractal Inspired Interconnects," *Small,* vol. 11, no. 3, pp. 367-373, Jan 21, 2015.

[65] H. R. Fu, S. Xu, R. X. Xu *et al.*, "Lateral buckling and mechanical stretchability of fractal interconnects partially bonded onto an elastomeric substrate," *Applied Physics Letters,* vol. 106, no. 9, Mar 2, 2015.

[66] Y. H. Zhang, H. R. Fu, S. Xu *et al.*, "A hierarchical computational model for stretchable interconnects with fractal-inspired designs," *Journal of the Mechanics and Physics of Solids,* vol. 72, pp. 115-130, Dec, 2014.

[67] M. A. Meitl, Z. T. Zhu, V. Kumar *et al.*, "Transfer printing by kinetic control of adhesion to an elastomeric stamp," *Nature Materials,* vol. 5, no. 1, pp. 33-38, Jan, 2006.

[68] M. A. M. Xue Feng, Audrey M. Bowen ,Yonggang Huang ,Ralph G. Nuzzo ,John A. Rogers, "Competing Fracture in Kinetically Controlled Transfer Printing," *Langmuir,* vol. 23, no. 25, pp. 12555–12560, 2007.

[69] J. Song, H. Jiang, Y. Huang *et al.*, "Mechanics of stretchable inorganic electronic materials," *Journal of Vacuum Science & Technology A,* vol. 27, no. 5, pp. 1107-1125, Sep, 2009.

[70] D. H. Kim, J. Z. Song, W. M. Choi *et al.*, "Materials and noncoplanar mesh designs for integrated circuits with linear elastic responses to extreme mechanical deformations," *Proceedings of the National Academy of Sciences of the United States of America,* vol. 105, no. 48, pp. 18675-18680, Dec 2, 2008.

[71] S. Xu, Y. H. Zhang, J. Cho *et al.*, "Stretchable batteries with self-similar serpentine interconnects and integrated wireless recharging systems," *Nature Communications,* vol. 4, pp. 1543, Feb, 2013.

[72] E. Vogel, "Technology and metrology of new electronic materials and devices," *Nature Nanotechnology,* vol. 2, pp. 25-32, 2007.

[73] J. R. Ives, S. M. Mirsattari, and D. Jones, "Miniaturized, on-head, invasive electrode connector integrated EEG data acquisition system," *Clinical Neurophysiology,* vol. 118, no. 7, pp. 1633-1638, Jul, 2007.

[74] P. Griss, H. K. Tolvanen-Laakso, P. Merilainen *et al.*, "Characterization of micromachined spiked biopotential electrodes," *Ieee Transactions on Biomedical Engineering,* vol. 49, no. 6, pp. 597-604, Jun, 2002.

[75] A. Searle, and L. Kirkup, "A direct comparison of wet, dry and insulating bioelectric recording electrodes," *Physiological Measurement,* vol. 21, no. 2, pp. 271-283, May, 2000.

[76] S. Kim, C. Laschi, and B. Trimmer, "Soft robotics: a bioinspired evolution in robotics," *Trends in Biotechnology,* vol. 31, no. 5, pp. 23-30, May, 2013.

[77] R. Pfeifer, M. Lungarella, and F. Iida, "The Challenges Ahead for Bio-Inspired 'Soft' Robotics," *Communications of the Acm,* vol. 55, no. 11, pp. 76-87, Nov, 2012.

[78] A. E. H. Love, *A Treatise on the Mathematical Theory of Elasticity*, New York, USA: Dover Publications, 2011.

[79] Y. J. Kang, and C. H. Yoo, "Thin-walled curved beams .1. Formulation of nonlinear equations - Closure," *Journal of Engineering Mechanics-Asce,* vol. 122, no. 5, pp. 483-484, May, 1996.

[80] V. K. Verma, "Thin-walled curved beams .1. Formulation of nonlinear equations - Discussion," *Journal of Engineering Mechanics-Asce,* vol. 122, no. 5, pp. 483-483, May, 1996.

[81] Y. B. Yang, and S. R. Kuo, "Thin-walled curved beams .1. Formulation of nonlinear equations," *Journal of Engineering Mechanics-Asce,* vol. 122, no. 5, pp. 482-483, May, 1996.

[82] N. L. Liping Liu, "Variational Formulations, Instabilities and Critical Loadings of Space Curved Beams," *International Journal of Solids and Structures,* vol. 87, no. 1, pp. 48-60, 2016.

[83] T. Li, Z. G. Suo, S. P. Lacour *et al.*, "Compliant thin film patterns of stiff materials as platforms for stretchable electronics," *Journal of Materials Research,* vol. 20, no. 12, pp. 3274-3277, Dec, 2005.

[84] D. S. Gray, J. Tien, and C. S. Chen, "High-conductivity elastomeric electronics," *Advanced Materials,* vol. 16, no. 5, pp. 393-397, Mar 5, 2004.

[85] D. Brosteaux, F. Axisa, M. Gonzalez *et al.*, "Design and fabrication of elastic interconnections for stretchable electronic circuits," *Ieee Electron Device Letters,* vol. 28, no. 7, pp. 552-554, Jul, 2007.

[86] Y. Y. Hsu, M. Gonzalez, F. Bossuyt *et al.*, "In situ observations on deformation behavior and stretching-induced failure of fine pitch stretchable interconnect," *Journal of Materials Research,* vol. 24, no. 12, pp. 3573-3582, Dec, 2009.

[87] S. X. Yihui Zhang, Haoran Fu,Juhwan Lee,Jessica Su,Keh-Chih Hwang,John A. Rogers and Yonggang Huang, "Buckling in serpentine microstructures and applications in elastomer-supported ultra-stretchable electronics with high areal coverage," *Soft Matter,* vol. 9, pp. 8062-8070, 2013.

[88] H. F. Yihui Zhang, Yewang Su, Sheng Xu ,, J. A. F. Huanyu Cheng , Keh-Chih Hwang, John A. Rogers⇑,, and b. Yonggang Huang a, c,d,⇑, "Mechanics of ultra-stretchable self-similar serpentine interconnects," *Acta Materialia,* vol. 61, no. 20, pp. 7916-7827, 2013.

[89] K. G. W. Pijnenburg, T. Seelig, and E. van der Giessen, "Successively refined models for crack tip plasticity in polymer blends," *European Journal of Mechanics a-Solids,* vol. 24, no. 5, pp. 740-756, Sep-Oct, 2005.

[90] S. W. Hwang, C. H. Lee, H. Y. Cheng *et al.*, "Biodegradable Elastomers and Silicon Nanomembranes/Nanoribbons for Stretchable, Transient Electronics, and Biosensors," *Nano Letters,* vol. 15, no. 5, pp. 2801-2808, May, 2015.

[91] S. X. Yang, Y. C. Chen, L. Nicolini *et al.*, ""Cut-and-Paste" Manufacture of Multiparametric Epidermal Sensor Systems," *Advanced Materials,* vol. 27, no. 41, pp. 6423-6430, Nov 4, 2015.

[92] Y. Y. Hsu, M. Gonzalez, F. Bossuyt *et al.*, "Design and analysis of a novel fine pitch and highly stretchable interconnect," *Microelectronics International,* vol. 27, no. 1, pp. 33-38, 2010.

[93] M. G. Yung-Yu Hsu, Frederick Bossuyt, Fabrice Axisa, Jan Vanfleteren and Ingrid DeWolf, "The effect of pitch on deformation behavior and the stretching-induced failure of a polymer-encapsulated stretchable circuit," *Journal of Micromechanics and Microengineering,* vol. 20, no. 7, 2010.

[94] Y. Y. Hsu, M. Gonzalez, F. Bossuyt *et al.*, "The effects of encapsulation on

deformation behavior and failure mechanisms of stretchable interconnects," *Thin Solid Films,* vol. 519, no. 7, pp. 2225-2234, Jan 31, 2011.

[95] Y. Y. Hsu, M. Gonzalez, F. Bossuyt *et al.*, "Polyimide-Enhanced Stretchable Interconnects: Design, Fabrication, and Characterization," *Ieee Transactions on Electron Devices,* vol. 58, no. 8, pp. 2680-2688, Aug, 2011.

[96] M. G. Yung-Yu Hsu, Frederick Bossuyt, Fabrice Axisa, Jan Vanfleteren, Ingrid De Wolf, "The effects of encapsulation on deformation behavior and failure mechanisms of stretchable interconnects," *Thin Solid Films,* vol. 519, no. 7, pp. 2225–2234, 2011.

[97] X. Huang, W. H. Yeo, Y. H. Liu *et al.*, "Epidermal Differential Impedance Sensor for Conformal Skin Hydration Monitoring," *Biointerphases,* vol. 7, no. 51, pp. 1, Dec, 2012.

[98] D. H. Kim, N. S. Lu, R. Ghaffari *et al.*, "Inorganic semiconductor nanomaterials for flexible and stretchable bio-integrated electronics," *NPG Asia Materials,* vol. 4, pp. e15, Apr, 2012.

[99] S. H. Wang, L. Lin, and Z. L. Wang, "Nanoscale Triboelectric-Effect-Enabled Energy Conversion for Sustainably Powering Portable Electronics," *Nano Letters,* vol. 12, no. 12, pp. 6339-6346, Dec, 2012.

[100] M. Ying, A. P. Bonifas, N. S. Lu *et al.*, "Silicon nanomembranes for fingertip electronics," *Nanotechnology,* vol. 23, no. 34, pp. 344004, Aug 31, 2012.

[101] P. Bai, G. Zhu, Z.-H. Lin *et al.*, "Integrated Multilayered Triboelectric Nanogenerator for Harvesting Biomechanical Energy from Human Motions," *ACS Nano,* vol. 7, no. 4, pp. 3713-3719, April, 2013, 2013.

[102] W. Wu, X. Wen, and Z. L. Wang, "Taxel-Addressable Matrix of Vertical-Nanowire Piezotronic Transistors for Active and Adaptive Tactile Imaging," *Science,* vol. 340, no. 6135, pp. 952-957, 2013.

[103] W.-H. Yeo, Y.-S. Kim, J. Lee *et al.*, "Multi-Functional Electronics: Multifunctional Epidermal Electronics Printed Directly Onto the Skin (Adv. Mater. 20/2013)," *Advanced Materials,* vol. 25, no. 20, pp. 2772-2772, 2013.

[104] G. H. Gelinck, H. E. A. Huitema, E. Van Veenendaal *et al.*, "Flexible active-matrix displays and shift registers based on solution-processed organic transistors," *Nature Materials,* vol. 3, no. 2, pp. 106-110, Feb, 2004.

[105] A. Bollero, L. Kaupmees, T. Raadik *et al.*, "Thermal stability of sputtered Mo/polyimide films and formation of MoSe2 and MoS2 layers for application in flexible Cu(In,Ga)(Se,S)(2) based solar cells," *Thin Solid Films,* vol. 520, no. 12, pp. 4163-4168, Apr 2, 2012.

[106] X. X. Wang, J. Y. Zhou, L. Lei *et al.*, "High Resolution ITO Lithography Using Excimer Laser for Flat-Panel Display Fabrication," *Advanced Manufacturing Technology, Pts 1-3,* vol. 314-316, pp. 1910-1913, 2011.

[107] C. H. Moon, "The Effect of the ITO Electrode Structure on the Luminous Characteristics of a Plasma Display Panel," *Ieee Transactions on Plasma Science,* vol. 38, no. 9, pp. 2445-2450, Sep, 2010.

[108] J. H. Lee, S. H. Sohn, J. H. Moon *et al.*, "Characteristics of ITO Thin Films for the Plasma Display Panel Prepared by a MF Dual Magnetron Sputtering in the Oxygen Atmosphere," *Molecular Crystals and Liquid Crystals,* vol. 499, pp. 500-506, 2009.

[109] X. J. Zhou, J. W. Xu, L. Yang *et al.*, "Effects of tin content on structure, properties, electrical repeatability, uniformity and stability of high sheet resistance ITO thin films for touch panels," *Journal of Materials Science-Materials in Electronics,* vol. 26, no. 9, pp. 6954-6960, Sep, 2015.

[110] S. Y. Liu, W. H. Li, Y. J. Wang *et al.*, "One Glass Single ITO Layer Solution for Large Size Projected-Capacitive Touch Panels," *Journal of Display Technology,* vol. 11, no. 9, pp. 725-729, Sep, 2015.

[111] C. H. Kim, W. J. Choi, S. K. Cho *et al.*, "Fabrication of Structurally Simple Index-Matched ITO Films Using Roll-to-Roll Sputtering for Touch Screen Panel Devices," *Plasma Processes and Polymers,* vol. 12, no. 11, pp. 1322-1327, Nov, 2015.

[112] S. H. Park, S. J. Lee, J. H. Lee *et al.*, "Large area roll-to-roll sputtering of transparent ITO/Ag/ITO cathodes for flexible inverted organic solar cell modules," *Organic Electronics,* vol. 30, pp. 112-121, Mar, 2016.

[113] X. Li, C. Y. Li, S. W. Hou *et al.*, "Thickness of ITO thin film influences on fabricating ZnO nanorods applying for dye-sensitized solar cell," *Composites Part B-Engineering,* vol. 74, pp. 147-152, Jun 1, 2015.

[114] A. Arunachalam, S. Dhanapandian, C. Manoharan *et al.*, "Characterization of sprayed TiO2 on ITO substrates for solar cell applications," *Spectrochimica Acta Part a-Molecular and Biomolecular Spectroscopy,* vol. 149, pp. 904-912, Oct 5, 2015.

[115] C. J. Yu, Z. Duan, P. X. Yuan *et al.*, "Electronically Programmable, Reversible Shape Change in Two- and Three-Dimensional Hydrogel Structures," *Advanced Materials,* vol. 25, no. 11, pp. 1541-1546, Mar 20, 2013.

[116] H. C. Ko, M. P. Stoykovich, J. Z. Song *et al.*, "A hemispherical electronic eye camera based on compressible silicon optoelectronics," *Nature,* vol. 454, no. 7205, pp. 748-753, Aug 7, 2008.

[117] L. Z. Xu, S. R. Gutbrod, Y. J. Ma *et al.*, "Materials and Fractal Designs for 3D Multifunctional Integumentary Membranes with Capabilities in Cardiac Electrotherapy," *Advanced Materials,* vol. 27, no. 10, pp. 1731-+, Mar 11, 2015.

[118] L. Z. Xu, S. R. Gutbrod, A. P. Bonifas *et al.*, "3D multifunctional integumentary membranes for spatiotemporal cardiac measurements and stimulation across the entire epicardium," *Nature Communications,* vol. 5, Feb, 2014.

[119] J. Kim, A. Banks, Z. Q. Xie *et al.*, "Miniaturized Flexible Electronic Systems with

Wireless Power and Near-Field Communication Capabilities," *Advanced Functional Materials,* vol. 25, no. 30, pp. 4761-4767, Aug 12, 2015.

[120] J. Kim, A. Banks, H. Y. Cheng *et al.*, "Epidermal Electronics with Advanced Capabilities in Near-Field Communication," *Small,* vol. 11, no. 8, pp. 906-912, Feb 25, 2015.

[121] M. Gonzalez, F. Axisa, F. Bossuyt *et al.*, "Design and performance of metal conductors for stretchable electronic circuits," *Circuit World,* vol. 35, no. 1, pp. 22-29, 2009.

[122] Y. Qi, J. Kim, T. D. Nguyen *et al.*, "Enhanced Piezoelectricity and Stretchability in Energy Harvesting Devices Fabricated from Buckled PZT Ribbons," *Nano Letters,* vol. 11, no. 3, pp. 1331-1336, Mar, 2011.

[123] T. Ma, Y. Wang, R. Tang *et al.*, "Pre-patterned ZnO nanoribbons on soft substrates for stretchable energy harvesting applications," *Journal of Applied Physics,* vol. 113, no. 20, pp. 204503, 2013.

[124] Y. Qi, T. D. Nguyen, P. K. Purohit *et al.*, "Stretchable Piezoelectric Nanoribbons for Biocompatible Energy Harvesting," *Stretchable Electronics*, pp. 111-139: Wiley-VCH Verlag GmbH & Co. KGaA, 2012.

[125] C. Peng, Z. Jia, D. Bianculli *et al.*, "In situ electro-mechanical experiments and mechanics modeling of tensile cracking in indium tin oxide thin films on polyimide substrates," *Journal of Applied Physics,* vol. 109, no. 10, May 15, 2011.

[126] C. Peng, Z. Jia, H. Neilson *et al.*, "In Situ Electro-Mechanical Experiments and Mechanics Modeling of Fracture in Indium Tin Oxide-Based Multilayer Electrodes," *Advanced Engineering Materials,* vol. 15, no. 4, pp. 250-256, Apr, 2013.

[127] S. X. Yang, B. Su, G. Bitar *et al.*, "Stretchability of indium tin oxide (ITO) serpentine thin films supported by Kapton substrates," *International Journal of Fracture,* vol. 190, no. 1-2, pp. 99-110, Nov, 2014.

[128] T. W. Shield, K. S. Kim, and R. T. Shield, "The Buckling of an Elastic Layer Bonded to an Elastic Substrate in Plane-Strain (Vol 61, Pg 231, 1994)," *Journal of Applied Mechanics-Transactions of the Asme,* vol. 61, no. 4, pp. 796-796, Dec, 1994.

[129] G. Gioia, and M. Ortiz, "Delamination of compressed thin films," *Advances in Applied Mechanics, Vol 33,* vol. 33, pp. 119-192, 1997.

[130] J. Liang, R. Huang, H. Yin *et al.*, "Relaxation of compressed elastic islands on a viscous layer," *Acta Materialia,* vol. 50, no. 11, pp. 2933-2944, Jun 28, 2002.

[131] S. Goyal, K. Srinivasan, G. Subbarayan *et al.*, "On instability-induced debond initiation in thin film systems," *Engineering Fracture Mechanics,* vol. 77, no. 8, pp. 1298-1313, May, 2010.

[132] J. Song, H. Jiang, Z. Liu *et al.*, "Buckling of a stiff thin film on a compliant substrate

in large deformation," *International Journal of Solids and Structures,* vol. 45, no. 10, pp. 3107-3121, May 15 2008, 2008.

[133] M. A. Brenckle, H. Y. Cheng, S. Hwang *et al.*, "Modulated Degradation of Transient Electronic Devices through Multilayer Silk Fibroin Pockets," *Acs Applied Materials & Interfaces,* vol. 7, no. 36, pp. 19870-19875, Sep 16, 2015.

[134] S. Il Park, D. S. Brenner, G. Shin *et al.*, "Soft, stretchable, fully implantable miniaturized optoelectronic systems for wireless optogenetics," *Nature Biotechnology,* vol. 33, no. 12, pp. 1280-1286, Dec, 2015.

[135] C. H. Lee, H. Kim, D. V. Harburg *et al.*, "Biological lipid membranes for on-demand, wireless drug delivery from thin, bioresorbable electronic implants," *Npg Asia Materials,* vol. 7, Nov, 2015.

[136] S. K. Kang, R. K. J. Murphy, S. W. Hwang *et al.*, "Bioresorbable silicon electronic sensors for the brain," *Nature,* vol. 530, no. 7588, pp. 71-76, Feb 4, 2016.

[137] A. Koh, S. R. Gutbrod, J. D. Meyers *et al.*, "Ultrathin Injectable Sensors of Temperature, Thermal Conductivity, and Heat Capacity for Cardiac Ablation Monitoring," *Advanced Healthcare Materials,* vol. 5, no. 3, pp. 373-381, Feb 4, 2016.

[138] J. Rogers, Y. G. Huang, O. G. Schmidt *et al.*, "Origami MEMS and NEMS," *Mrs Bulletin,* vol. 41, no. 2, pp. 123-129, Feb, 2016.

[139] Y. H. Zhang, R. C. Webb, H. Y. Luo *et al.*, "Theoretical and Experimental Studies of Epidermal Heat Flux Sensors for Measurements of Core Body Temperature," *Advanced Healthcare Materials,* vol. 5, no. 1, pp. 119-127, Jan, 2016.

[140] S. D. Wang, M. Li, J. Wu *et al.*, "Mechanics of Epidermal Electronics," *Journal of Applied Mechanics-Transactions of the Asme,* vol. 79, no. 3, May, 2012.

[141] J. W. Jeong, W. H. Yeo, A. Akhtar *et al.*, "Materials and Optimized Designs for Human-Machine Interfaces Via Epidermal Electronics," *Advanced Materials,* vol. 25, no. 47, pp. 6839-6846, Dec, 2013.

[142] S. T. Qiao, J. B. Gratadour, L. Wang *et al.*, "Conformability of a Thin Elastic Membrane Laminated on a Rigid Substrate With Corrugated Surface," *Ieee Transactions on Components Packaging and Manufacturing Technology,* vol. 5, no. 9, pp. 1237-1243, Sep, 2015.

[143] N. L. Liu Wang, "Conformability of a Thin Elastic Membrane Laminated on a Soft Substrate With Slightly Wavy Surface," *Journal of Applied Mechanics,* vol. 83, no. 4, pp. 1662-1671, 2016.

[144] H. J. Kock, K. M. Sturmer, R. Letsch *et al.*, "Interface and Biocompatibility of Polyethylene Terephthalate Knee Ligament Prostheses - a Histological and Ultrastructural Device Retrieval Analysis in Failed Synthetic Implants Used for Surgical Repair of Anterior Cruciate Ligaments," *Archives of Orthopaedic and Trauma Surgery,* vol. 114, no. 1, pp. 1-7, Dec, 1994.

[145] I. K. Descheerder, K. V. Wilczek, E. V. Verbeken *et al.*, "Intraarterial Biocompatibility of Polyethylene Terephthalate Self-Expandable Stents Implanted in Porcine Peripheral Arteries," *Academic Radiology,* vol. 2, no. 2, pp. 154-158, Feb, 1995.

[146] H. Seitz, S. Marlovits, I. Schwendenwein *et al.*, "The biocompatibility of polyethylene terephthalate PET (Trevira(R) hochfest). An in vivo study on sheep stifle joints," *Biomedizinische Technik,* vol. 41, no. 6, pp. 178-182, Jun, 1996.

[147] H. Seitz, S. Marlovits, I. Schwendenwein *et al.*, "Biocompatibility of polyethylene terephthalate (Trevira (R) hochfest) augmentation device in repair of the anterior cruciate ligament," *Biomaterials,* vol. 19, no. 1-3, pp. 189-196, Jan-Feb, 1998.

[148] N. V. Thakor, and Y. S. Zhu, "Applications of Adaptive Filtering to Ecg Analysis - Noise Cancellation and Arrhythmia Detection," *Ieee Transactions on Biomedical Engineering,* vol. 38, no. 8, pp. 785-794, Aug, 1991.

[149] W. Klimesch, "EEG alpha and theta oscillations reflect cognitive and memory performance: a review and analysis," *Brain Research Reviews,* vol. 29, no. 2-3, pp. 169-195, Apr, 1999.

[150] F. Rosenow, K. M. Klein, and H. M. Hamer, "Non-invasive EEG evaluation in epilepsy diagnosis," *Expert Review of Neurotherapeutics,* vol. 15, no. 4, pp. 425-444, Apr, 2015.

[151] K. G. Jordan, "Emergency EEG and continuous EEG monitoring in acute ischemic stroke," *Journal of Clinical Neurophysiology,* vol. 21, no. 5, pp. 341-352, Sep-Oct, 2004.

[152] A. M. F. L. M. de Sa, J. M. de Seixas, J. D. Costa *et al.*, "A principal component-based algorithm for denoising in single channel data (PCA for denoising in single channel data)," *Measurement,* vol. 60, pp. 121-128, Jan, 2015.

[153] C. Blichmann, and J. Serup, "Hydration Studies on Scaly Hand Eczema," *Contact Dermatitis,* vol. 16, no. 3, pp. 155-159, Mar, 1987.

[154] B. M. Morrison, and D. D. Scala, "Comparison of instrumental measurements of skin hydration," *Journal of Toxicology-Cutaneous and Ocular Toxicology,* vol. 15, no. 4, pp. 305-314, 1996.

[155] P. G. Sator, J. B. Schmidt, and H. Honigsmann, "Comparison of epidermal hydration and skin surface lipids in healthy individuals and in patients with atopic dermatitis," *Journal of the American Academy of Dermatology,* vol. 48, no. 3, pp. 352-358, Mar, 2003.

[156] K. L. E. Hon, K. Y. Wong, T. F. Leung *et al.*, "Comparison of skin hydration evaluation sites and correlations among skin hydration, transepidermal water loss, SCORAD index, Nottingham eczema severity score, and quality of life in patients with atopic dermatitis," *American Journal of Clinical Dermatology,* vol. 9, no. 1, pp. 45-50, 2008.

[157] J. Fantasia, J. C. Liu, and T. Chen, "Comparison of skin hydration levels among three ethnic populations in the United States," *Journal of the American Academy of Dermatology,* vol. 62, no. 3, pp. Ab60-Ab60, Mar, 2010.

[158] P. G. Sator, J. B. Schmidt, T. Rabe *et al.*, "Skin aging and sex hormones in women - clinical perspectives for intervention by hormone replacement therapy," *Experimental Dermatology,* vol. 13, pp. 36-40, Dec, 2004.

[159] B. W. Tran, A. D. P. Papoiu, C. V. Russoniello *et al.*, "Effect of Itch, Scratching and Mental Stress on Autonomic Nervous System Function in Atopic Dermatitis," *Acta Dermato-Venereologica,* vol. 90, no. 4, pp. 354-361, 2010.

[160] S. M. Kleiner, "Water: An essential but overlooked nutrient," *Journal of the American Dietetic Association,* vol. 99, no. 2, pp. 200-206, Feb, 1999.

[161] M. Boguniewicz, N. Nicol, K. Kelsay *et al.*, "A multidisciplinary approach to evaluation and treatment of atopic dermatitis," *Seminars in Cutaneous Medicine and Surgery,* vol. 27, no. 2, pp. 115-127, Jun, 2008.

[162] N. Lu, C. Lu, S. Yang *et al.*, "Highly Sensitive Skin-Mountable Strain Gauges Based Entirely on Elastomers," *Advanced Functional Materials,* vol. 22, no. 19, pp. 4044-4050, 2012.

[163] V. Arumugam, M. D. Naresh, and R. Sanjeevi, "Effect of Strain-Rate on the Fracture-Behavior of Skin," *Journal of Biosciences,* vol. 19, no. 3, pp. 307-313, Sep, 1994.

[164] B. Liea, and K. J. Loh, "Passive Wireless Sensors for Monitoring Particle Movement at Soil-Structure Interfaces," *Sensors and Smart Structures Technologies for Civil, Mechanical, and Aerospace Systems 2010,* vol. 7647, 2010.

[165] Y. Ikemoto, S. Suzuki, H. Okamoto *et al.*, "Force sensor system for structural health monitoring using passive RFID tags," *Sensor Review,* vol. 29, no. 2, pp. 127-136, 2009.

[166] M. Kubo, X. F. Li, C. Kim *et al.*, "Stretchable Microfluidic Radiofrequency Antennas," *Advanced Materials,* vol. 22, no. 25, pp. 2749-2752, Jul 6, 2010.

[167] R. Matsuzaki, and A. Todoroki, "Wireless flexible capacitive sensor based on ultra-flexible epoxy resin for strain measurement of automobile tires," *Sensors and Actuators a-Physical,* vol. 140, no. 1, pp. 32-42, Oct 1, 2007.

[168] K. H. Shin, C. R. Moon, T. H. Lee *et al.*, "Flexible wireless pressure sensor module," *Sensors and Actuators a-Physical,* vol. 123-24, pp. 30-35, Sep 23, 2005.

[169] M. G. A. Michael A. Fonseca (1), Jason Kroh (2) and Jason White, "Flexible Wireless Passive Pressure Sensors For Biomedical Applications," 2006.

[170] Greenhou.Hm, "Design of Planar Rectangular Microelectronic Inductors," *Ieee Transactions on Parts Hybrids and Packaging,* vol. Ph10, no. 2, pp. 101-109, 1974.

[171] S. S. Mohan, M. D. Hershenson, S. P. Boyd *et al.*, "Simple accurate expressions for planar spiral inductances," *Ieee Journal of Solid-State Circuits,* vol. 34, no. 10, pp.

1419-1424, Oct, 1999.

[172] K. Um, and B. An, "Design of rectangular printed planar antenna via input impedance for supporting mobile wireless communications," *Ieee 55th Vehicular Technology Conference, Vtc Spring 2002, Vols 1-4, Proceedings*, pp. 948-951, 2002.

[173] K. Phaebua, D. Torrungrueng, and C. Phongcharoenphanich, "Design of Planar Rectangular Spiral Antennas for the Wireless Vehicle Battery Charging System," *2013 Asia-Pacific Microwave Conference Proceedings (Apmc 2013)*, pp. 1172-1174, 2013.